UNIVERSITÀ DEGLI STUDI DI TRIESTE
Sede Amministrativa del Dottorato di Ricerca

XX CICLO DEL DOTTORATO DI RICERCA IN INGEGNERIA E SCIENZA DEI MATERIALI

APPLICATIONS OF X-RAY COMPUTED MICROTOMOGRAPHY TO MATERIAL SCIENCE: DEVICES AND PERSPECTIVES

Settore scientifico-disciplinare ING-IND/22

DOTTORANDO:
Stefano FAVRETTO

COORDINATORE DEL COLLEGIO DEI DOCENTI:
Chiar.mo Prof. Sergio MERIANI
Università degli Studi di Trieste

TUTORE:
Dr. Lucia MANCINI
Sincrotrone Trieste S.C.p.A.

RELATORE:
Chiar.mo Prof. Elio LUCCHINI
Università degli Studi di Trieste

Abstract

The three-dimensional visualization of the inner microstructural features of objects and materials is an aspect of relevant interest for a wide range of scientific and industrial applications. X-ray computed microtomography (μ-CT) is a powerful non-destructive technique capable to satisfy these needs.

Once the complete reconstruction of the sample is available, a quantitative characterisation of the microstructure is essential. Through digital image processing tools, image analysis software or custom developed algorithms, it is possible to obtain an exhaustive geometrical, morphological and topological description of the features inside the volume, or to extract other particular parameters of interest (e.g. porosity, voids distribution, cell size distribution, average struts length, connectivity between the cells, tortuosity).

This thesis was carried out at the third-generation Elettra Synchrotron Radiation Facility (Trieste, Italy), where a hard X-ray imaging beamline is available. The experience developed at this beamline has leaded scientists to design a complementary state-of-the-art μ-CT facility based on a micro-focus X-ray source, working both in absorption and phase contrast mode.

In this dissertation a detailed description of this facility is given together with a rigorous characterization of the imaging system capabilities, in terms of the actual achievable spatial resolution, in order to optimize the working parameters for the different experiments. The main artefacts that concur to the degradation of the quality of the reconstructed images have been considered (e.g. beam hardening effects, ring

artefacts, uncertainness associated with the cone-beam geometry): procedures are presented in order to eliminate, or at least to reduce, the causes of these artefacts.

The aspects related to the digital image processing of the reconstructed data are intensively developed in this study: appropriated methodologies have been elaborated capable to deal with the different three-dimensional data of complex porous media, providing a correlation between the microstructure and the macroscopic behaviour of the observed materials.

Three representative examples obtained with the described methods are used to demonstrate the application of μ-CT, combined with the developed image processing tools, to material science: the geometrical and morphological characterisation of polyurethane foams employed in the automotive industry due their vibro-acoustic properties; a new approach to characterize the resonance spruce wood microstructure in order to study its acoustical behaviour; finally, the possibility of revealing defects in hybrid-friction stir welded aluminium joints, guiding the optimization of the process parameters.

Contents

Chapter 2

Chapter 3

Chapter 4

List of Figures

List of Tables

List of abbreviations

CCD	Charge Coupled Device
CMB	Centres of Maximal Balls
CT	Computed Tomography
DIA	Digital Image Analysis
DIP	Digital Image Processing
DT	Distance Transform
EDM	Euclidean Distance Map
ESF	Edge Spread Function
FBP	Filtered Back Projection
FDM	Finite Difference Method
FEM	Finite Element Method
FFT	Fourier Fast Transform
FOV	Field Of View
FS	Focal Spot
FSW	Friction Stir Welding
FWHM	Full Width Half Maximum
GMAW	Gas Metal Arc Welding
GTAW	Gas Tungsten Arc Welding
HFSW	Hybrid Friction Stir Welding
LBM	Lattice Boltzmann Method
LSF	Line Spread Function
MA	Medial Axis
MTF	Modulation Transfer Function

NDT	Non-Destructive Testing
PHC	Phase Contrast
PSF	Point Spread Function
REV	Representative Elementary Volume
ROI	Region Of Interest
SEM	Scanning Electron Microscopy
TIG	Tungsten Inert Gas
VOI	Volume Of Interest
VPPAW	Variable Polarity Plasma Arc Welding
XRCT	X-Ray Computed Tomography
μ-CT	Micro-Computed Tomography

Sintesi

La microtomografia a raggi X

Lo sviluppo di metodologie non distruttive, volte all'analisi della microstruttura dei più svariati tipi di materiale, è oggi un'esigenza fortemente sentita in molteplici settori del settore produttivo e della ricerca. Si manifesta così la necessità di avere a disposizione una adeguata strumentazione da laboratorio, la quale consenta di effettuare tutte le analisi in maniera semplice e veloce, contenendo i costi dell'operazione.

La tomografia computerizzata (CT), nell'ambito delle prove non distruttive, è una delle tecniche diagnostiche più avanzate ed attualmente di maggior interesse. Tomografia è parola composta dal greco τόμος (sezione) e γράφω (disegnare): dunque, operando una tomografia, si disegna una sezione. In effetti, questa definizione non è lontana dal vero: ciò che si ottiene tramite la tomografia è una riproduzione del volume interno di un oggetto, a partire proprio dalla ricostruzione delle sue sezioni trasversali.

Nata in ambiente medico quando nel 1972 Hounsfield realizzò il primo scanner dedicato allo studio della struttura ossea del corpo umano, la CT ha poi assunto, nel corso degli anni '80 e '90, una sempre crescente importanza anche in campo scientifico ed industriale.

Oggigiorno, grazie all'avanzamento tecnologico raggiunto nonché all'elevata potenza di calcolo dei moderni elaboratori, la CT ad alta risoluzione (μ-CT) è largamente impiegata in un vasto campo di applicazioni.

Dal punto di vista strumentale, gli elementi principali che compongono una postazione per μ-CT sono la sorgente di radiazione X, l'apparato per il posizionamento e la movimentazione d'alta precisione del campione da sottoporre ad analisi e il sistema di raccolta della radiazione trasmessa uscente dall'oggetto (detector).

Il principio di funzionamento deriva direttamente dalla tecnica radiografica, poiché sfrutta il potere penetrante dei raggi X e il loro assorbimento da parte della materia. Una radiazione di intensità nota, emessa dalla sorgente, attraversa il campione che è posto su un piatto rotante, e l'intensità della radiazione non assorbita durante l'attraversamento viene registrata sul piano del detector collocato oltre al campione. Mano a mano che l'oggetto ruota sul piatto attorno al proprio asse, secondo la schema descritto, si ottengono diverse proiezioni bidimensionali dello stesso. Da un sufficiente numero di proiezioni è possibile ricostruire la struttura interna dell'oggetto, attraverso procedimenti matematici che furono elaborati per la prima volta da Radon già nel 1917. Tali algoritmi di ricostruzione si basano sulla tecnica della retroproiezione filtrata (FBP) (Kak & Slaney, 1987). Il prodotto ultimo del processo è costituito da una serie di immagini in scala di grigio che rappresentano ciascuna una fetta orizzontale (*slice*) dell'oggetto esaminato. Le tonalità di grigio evidenziate nella slice forniscono una mappa della distribuzione dei coefficienti di assorbimento ai raggi X in seno al campione analizzato. Tali coefficienti, a loro volta, dipendono dalla densità del materiale incontrato, dal numero atomico degli elementi costituenti il campione oltre che dall'energia incidente utilizzata.

La fase di sviluppo iniziale della μ-CT è legata alla costruzione dei grossi acceleratori di particelle, quali i sincrotroni di terza generazione. La μ-CT con luce di sincrotrone trae vantaggio da alcune caratteristiche peculiari del fascio incidente come l'elevato grado di monocromaticità e la notevole coerenza spaziale solitamente disponibile. Quest'ultimo aspetto permette l'acquisizione di immagini in contrasto di fase (PHase Contrast imaging), accanto naturalmente alla tradizionale modalità in assorbimento (Cloetens et al., 2001). Con la tecnica del PHC si recuperano le informazioni sulla variazione di fase ed ampiezza del fronte d'onda dovute all'attraversamento dal campione da parte dei raggi, potendo di conseguenza riconoscere materiali leggeri altrimenti "trasparenti" ai raggi X, quali campioni biologici oppure un filo di nylon, e contemporaneamente di discriminare fra loro materiali aventi coefficiente di attenuazione molto simile, altrimenti indistinguibili (Stevenson et al., 2003). L'altra peculiare caratteristica della tomografia con luce di sincrotrone consiste nella geometria del fascio incidente, che è costituito da raggi approssimativamente paralleli tra loro (solitamente infatti la grande distanza presente fra la sorgente di radiazione ed il campione, dell'ordine di alcune decine di metri, rende la divergenza laterale dei raggi molto piccola da consentire tale assunzione).

Recentemente tuttavia il progresso tecnologico che ha condotto alla realizzazione di sorgenti a raggi X da laboratorio aventi una macchia focale di dimensione micrometrica, o anche sub-micrometrica, ha favorito una rapida diffusione di stazioni per μ-CT indipendenti e di sistemi, per così dire, portatili. In questi casi, in cui la geometria del fascio risulta conica, la riduzione delle dimensioni finite della sorgente è fra i fattori determinanti per il raggiungimento di elevate risoluzioni spaziali (Lopes et al., 1997). Le scelte progettuali nel loro complesso, che devono stabilire il miglior accoppiamento delle componenti da assemblare, appaiono di fondamentale importanza per l'ottimizzazione delle prestazione dell'intera apparecchiatura (Pogany et al., 1997). In particolare, la ridotta macchia focale, unitamente alla possibilità di ingrandimento per via geometrica del campione sul piano di acquisizione, ovvero il tipo di rivelatore impiegato e la dimensione dei suoi pixel, sono tutti aspetti da ponderare con cura.

Strumentazioni allo stato dell'arte offrono la possibilità di raggiungere, in linea di principio, risoluzioni spaziali dello stesso ordine di grandezza delle dimensioni della macchia focale. Nella pratica, dettagli di pochi micrometri possono venire evidenziati su campioni di dimensioni millimetriche, rendendo, da questo punto di vista, i risultati ottenuti mediante apparecchiature da laboratorio spesso paragonabili a quelli conseguiti con sorgenti che sfruttano la luce di sincrotrone (Bernhardt et al., 2004).

In questo contesto si inserisce il progetto per la realizzazione di una stazione per microtomografia computerizzata, denominata TOMOLAB, presso il Laboratorio Nazionale di Ricerca di Elettra, sorto da una collaborazione tra la stessa Elettra e l'Università degli Studi di Trieste. La stazione, appena realizzata, affianca ora in maniera complementare e sinergica la già esistente linea di luce SYRMEP (SYnchrotron Radiation for MEdical Physics) dedicata allo studio e allo sviluppo di nuove tecniche di acquisizione d'immagine, in campo medicale e nel campo della scienza dei materiali. TOMOLAB inoltre, per alcune attività sperimentali sia scientifiche sia industriali, ha già dimostrato di rappresentare una valida alternativa alla linea di luce, potendo talora sostituirsi ad essa.

La sorgente di raggi X in uso al TOMOLAB, dotata di un anodo in tungsteno, garantisce una macchia focale ridotta a 5 μm (a 4 W), ed emette uno spettro policromatico in un intervallo energetico tra i 40 e 130 kV, ben superiore all'energia selezionabile al monocromatore della linea SYRMEP (tra 8.3 e 35 keV). Il rivelatore è costituito da una camera CCD e unisce i vantaggi di possedere un ampio campo di vista

(la matrice è formata da 4008×2670 elementi) e una ridotta dimensione del singolo pixel (12.5×12.5 μm).

Se, come già accennato, la risoluzione spaziale oggi disponibile è tipicamente dell'ordine di pochi micrometri, è tuttavia vero che la qualità complessiva di una slice ricostruita non dipende soltanto dal potere risolutivo delle singole componenti di un apparato per μ-CT, ma è condizionata anche da diversi tipi di altri fattori e dai numerosi artefatti presenti nelle slice, causati dalle intrinseche limitazioni dovute al processo di acquisizione e dall'incertezza geometrica associata al sistema, che si ripercuote poi nel successivo processo di ricostruzione (Barrett & Keat, 2004). A tal proposito, è utile evidenziare come la geometria conica del fascio introduca di per sé un certo grado di incertezza associato ai numerosi parametri liberi (non basta soltanto che l'asse di rotazione del campione sia allineato con una colonna di pixel del detector, ma servirà conoscere, ad esempio, la posizione e l'inclinazione del piano centrale del fascio, e dell'asse del cono in particolare, verificare la sua ortogonalità col piano del detector etc.) e richiede l'impiego di algoritmi di ricostruzione più complessi (Feldkamp et al., 1984).

Gli artefatti cui si faceva riferimento poco sopra possono essere visti in generale come ogni distorsione introdotta nell'immagine originale, in maniera sistematica oppure casuale, che porti in generale al deterioramento della qualità dell'immagine ricostruita ovvero alla perdita delle informazioni in essa contenute. Non tutti gli artefatti possono essere eliminati; tuttavia, è possibile ridurne gli effetti in via preventiva o in fase di post-elaborazione.

Il presente lavoro di tesi illustra e riassume attività svolte sia presso la linea SYRMEP, in stretta collaborazione con i ricercatori che vi operano e molti degli utenti che ne hanno usufruito, sia presso il laboratorio TOMOLAB, la cui messa a punto e caratterizzazione fanno parte integrante del lavoro medesimo.

L'analisi del dato digitale

Il più delle volte, l'interesse primario non risiede tanto nella visualizzazione del dato tomografico raccolto, quanto nella sua successiva elaborazione al fine di estrarne delle informazioni quantitative, che siano significative per la specifica applicazione.

Pertanto, in contemporanea alla messa in funzione del laboratorio TOMOLAB, è stata affrontata e approfondita la preparazione di specifiche metodologie di analisi di immagine volte alla caratterizzazione quantitativa dei campioni oggetto di indagine.

Molteplici, come detto, sono i settori di applicazione della μ-CT alla scienza dei materiali dal momento che molto spesso è richiesta una correlazione tra proprietà macroscopiche e microstruttura (Baruchel et al., 2000; Salvo et al., 2003; Knackstedt et al., 2005). Non solo sono possibili analisi quantitative di sistemi multifase, ma anche la caratterizzazione della tessitura e la determinazione della continuità di una fase all'interno di un composto. Inoltre, a volte sorge la necessità di valutare, tramite metodi non invasivi, la variazione di densità in seno al materiale durante il processo di carico e scarico, di osservare insomma come la microstruttura di un corpo evolve percorrendo la tipica curva sforzo-deformazione.

Tutto ciò può essere particolarmente significativo per effettuare test di qualità su materiali nuovi o già esistenti, per riconoscere la formazione di difetti e prevenire eventuali rotture, per esaminare lo stato di affaticamento del materiale dopo un certo numero di cicli lavorativi.

La caratterizzazione geometrica e morfologica della microstruttura interna dei materiali, in particolare quando si tratta di mezzi porosi costituiti da una fase vuota variamente distribuita e interconnessa, è fondamentale per l'ottimizzazione dei parametri del processo produttivo, e contribuisce enormemente alla definizione di adeguati modelli concettuali ove simulare il comportamento meccanico, acustico, termico o fluido-dinamico per i materiali osservati (Spanne et al., 1994; Torquato, 2001).

Molto spesso la μ-CT è utilizzata indirettamente per ricavare, attraverso metodi di analisi di immagine, una serie di parametri necessari alla corretta modellazione del mezzo, ad esempio tramite modelli agli elementi finiti (FEM) (Maire et al., 2003); tuttavia, sempre più spesso si ricorre all'uso di simulazioni direttamente condotte sul dato digitale raccolto, compatibilmente con la risoluzione spaziale raggiunta, come avviene per esempio con i metodi Lattice Boltzmann (LB), oggi largamente diffusi anche per lo studio di sistemi multifase, dove gli stessi voxel definiscono gli elementi di calcolo (Garboczi, 1999; Succi, 2001).

Un mezzo poroso può essere semplicemente visto come un materiale solido che contiene dei "buchi" al suo interno: una definizione così intuitiva, tuttavia, contiene implicitamente il concetto di omogeneità e quello di scala (Garboczi et al., 1999) che impongono di comparare la dimensione dei vuoti con la grandezza tipica dell'oggetto considerato nonché di valutare come i vuoti siano distribuiti all'interno del campione.

L'osservazione di mezzi porosi naturali quali le rocce e i suoli occupa una posizione di riguardo nel campo delle geoscienze (Ketcham & Carlson, 2001; Wildenshild et al., 2002), sia per quanto concerne tematiche di attualità ambientale quali il ripristino di acquiferi contaminati, la produzione di energia geotermica o l'immagazzinamento nel sottosuolo di anidride carbonica (Iglauer et al., 2008), che le problematiche legate all'ingegneria petrolifera (Knackstedt, 2004; Al-Kharusi and Blunt, 2007). In tutti i casi citati, la descrizione da un punto di vista geometrico, morfologico e topologico dello spazio poroso complesso risulta fondamentale per la comprensione dei fenomeni di trasporto fluido o termico attraverso il mezzo (Coles et al., 1996).

D'altra parte, numerosi sistemi porosi artificiali risultano di grande interesse in particolar modo per il loro carattere innovativo: schiume metalliche vengono largamente utilizzate nel settore dei trasporti e in quello edile data la loro leggerezza e robustezza (Olurin et al., 2002), schiume plastiche vengono impiegate nell'industria dei trasporti e degli imballaggi in considerazione delle loro ottime proprietà termo- e vibro-isolanti (Saadatfar et al., 2004), altri materiali con struttura cellulare presentano altrettanto utili proprietà meccaniche, termiche e acustiche (Monminy et al., 2001), materiali compositi o a matrice cementizia vengono invece continuamente migliorati per soddisfare alle nuove richieste tecnologiche (Gallucci et al., 2007). Di nuovo, la microstruttura interna di tutti questi materiali richiede di essere accuratamente descritta in modo da determinare le loro prestazioni attraverso modelli numerici, poter correttamente riprodurli ed impiegarli poi nel modo più efficace.

La soluzione dei problemi pratici che coinvolgono i mezzi porosi o i sistemi multifase necessita della conoscenza delle proprietà macroscopiche della matrice porosa, come la porosità, la permeabilità, la tortuosità, la conducibilità termica o elettrica e molte altre. Spesso, nel passato, tecniche specifiche di analisi sono state applicate ad immagini bidimensionali ottenute attraverso metodi ottici o di superficie. Ora, l'estensione di questi concetti ai casi tridimensionali rappresenta spesso una sfida non banale, richiedendo sia uno sforzo consistente di calcolo sia l'implementazione di nuovi approcci metodologici.

Uno dei punti cruciali è la gestione, a livello di risorse di calcolo investite, di enormi quantità di dati, dapprima dal punto di vista della ricostruzione tomografica, poi soprattutto dal punto di vista dell'elaborazione del dato raccolto (basti pensare che è del tutto normale trattare svariati Gb di dati nel corso di una singola acquisizione tomografica).

Anche per queste ragioni, il costante progresso tecnologico che coinvolge la μ-CT avviene secondo due direttrici principali: da un lato, il miglioramento e lo sviluppo di nuovi sistemi in grado di migliorare la qualità dell'immagine e ridurre i tempi di raccolta delle misure; dall'altro, lo sviluppo di sistemi di calcolo più efficienti, capaci di diminuire il tempo di elaborazione dell'immagine, e di nuovi software applicativi in grado di incrementare notevolmente le capacità di post-processing.

Organizzazione della tesi

Si riporta di seguito un breve riepilogo delle principali tematiche affrontate, nel corso dei prossimi capitoli, dal presente lavoro di tesi.

Il primo capitolo fornisce innanzitutto una panoramica di riferimento circa la tecnica tomografica, presentandone gli aspetti più generali a partire dai principi fisici della produzione dei raggi X e dalla loro interazione con la materia, evidenziando poi le componenti hardware e software coinvolte nel processo di acquisizione e ricostruzione delle immagini e distinguendo fra le diverse modalità di acquisizione in assorbimento oppure in contrasto di fase. Infine, viene descritta la linea di luce SYRMEP di Elettra.

Il capitolo secondo è invece interamente dedicato al laboratorio TOMOLAB. Vengono definite le scelte progettuali adottate, con particolare riferimento all'accoppiamento fra le diverse componenti. Inoltre, poiché le fasi di assemblaggio, messa a punto e verifica della stazione rappresentano una parte rilevante dell'attività svolta nell'ambito del dottorato, esse sono ripercorse per sommi capi fino alla completa entrata in funzione del laboratorio per μ-CT. È illustrata perciò anche l'organizzazione delle modalità di controllo e di gestione della strumentazione in fase operativa, basate in parte su programmi commerciali, come ad esempio nel caso della ricostruzione delle slice, in parte su software appositamente implementato. Infine, in questo capitolo sono presentati i risultati di alcuni test preliminari qualitativi svolti sul sistema, con l'obiettivo di porre a confronto immagini planari di determinati campioni acquisite anche con luce di sincrotrone alla linea SYRMEP, dimostrando, fra l'altro, la possibilità di sfruttare pure al TOMOLAB la modalità di lavoro in contrasto di fase.

Il capitolo terzo introduce importanti concetti legati alla qualità dell'immagine, in termini di risoluzione spaziale e di contrasto. Viene fornita così una caratterizzazione delle prestazioni del sistema completo sulla base di parametri matematici quali la Point Spread Function (PSF) e la Modulation Transfer Function (MTF). Queste funzioni particolari sono valutate non soltanto, come è prassi, sulle radiografie acquisite ma

anche, secondo un criterio certamente più significativo per le reali applicazioni di μ-CT, sulle slice ricostruite. Il capitolo tratta inoltre nel dettaglio dei più comuni artefatti che si incontrano nella μ-CT a fascio conico e con sorgente policromatica, portando per ognuno di essi degli esempi pratici riscontrati operando al laboratorio TOMOLAB. Vengono proposti di volta in volta dei metodi che possono portare alla loro eliminazione o, perlomeno, alla riduzione degli effetti più deleteri per la qualità del dato elaborato.

Col capitolo quarto si affronta la seconda parte della trattazione, ovvero quella dedicata all'analisi di immagine digitale (DIP) a seguito dell'ottenimento del dato tomografico. Il capitolo propone una visione d'insieme delle tecniche di elaborazione di immagine disponibili, descrivendo poi le metodologie specifiche che sono state messe a punto nel corso di questo lavoro di tesi per l'analisi dei dati tomografici acquisiti, e che sono state raccolte in un programma sviluppato in ambiente Matlab (PORE3D). Questo raggruppa in un unico software, versatile e di semplice utilizzo, gli algoritmi dedicati al miglioramento dell'immagine (filtraggio, segmentazione), accanto a strumenti investigativi più complessi volti alla caratterizzazione tridimensionale della microstruttura dei campioni oggetto di indagine. Nel capitolo viene illustrato l'approccio che prevede l'estrazione del cosiddetto scheletro, come rappresentazione semplificata monodimensionale di un oggetto 3D. Poiché l'estrazione dello scheletro, richiedendo un controllo continuo sui singoli voxel, risulta spesso complicata e onerosa dal punto di vista del calcolo, è stato implementato un approccio alternativo in grado di estrarre un gran numero di percorsi possibili all'interno della microstruttura analizzata, da utilizzare poi come strumenti esplorativi e di navigazione per ricavare misure quantitative relativamente alla geometria, alla morfologia e alla topologia dello spazio poroso stesso.

Nel capitolo quinto infine, vengono presentati alcuni studi sviluppati nell'ambito dell'attività svolta sia alla linea SYRMEP sia al TOMOLAB, attinenti alla scienza dei materiali. I risultati presentati si estendono dall'acquisizione del dato all'estrapolazione dei risultati quantitativi associati.

Il primo materiale esaminato è una schiuma poliuretanica, con struttura a celle aperte, impiegata nell'industria automobilistica e dei trasporti per le sue ottime proprietà di isolamento vibro-acustico. Essa costituisce un tipico esempio di materiale poroso omogeneo a due fasi, il cui comportamento fisico a livello macroscopico è determinato dall'interazione tra lo scheletro solido ed il sistema di vuoti - tipicamente saturi d'aria -

- che lo compongono. Alcuni parametri di natura puramente geometrica, richiesti come dato di input nei modelli matematici comunemente utilizzati (Biot, 1956) vengono determinati attraverso l'elaborazione del dato tridimensionale. Tra questi la porosità, la tortuosità e la lunghezza caratteristica termica. A validazione del metodo di analisi proposto, vengono analizzati campioni di materiale con caratteristiche molto distinte in termini di prestazioni.

Il secondo caso di studio presentato riguarda un materiale poroso naturale quale il legno. In particolare, si prenderà in considerazione la caratterizzazione microstrutturale del legno di risonanza (Abies Picea) impiegato per la realizzazione di strumenti musicali quali tavole armoniche per pianoforti. Sebbene in questo campo le conoscenze siano di origine mista, basandosi sia su studi scientifici, ma anche e soprattutto su regole empiriche legate all'esperienza, alla tecnica magistrale e alla sensibilità dei liutai, si è voluto tuttavia mettere in luce il contributo della microstruttura, evidenziata tramite μ-CT, alle proprietà acustiche che determinano una migliore (o peggiore) qualità del legno medesimo. A questo scopo sono stati presi in considerazione e messi a confronto legni di abete di diversa provenienza tramite metodi di analisi di immagine e simulazione agli elementi finiti del comportamento vibro-acustico del materiale.

Il terzo studio proposto, di carattere completamente diverso rispetto ai precedenti, riguarda la valutazione dei difetti nei giunti di alluminio saldati tramite una tecnica innovativa quale la Hybrid Friction Stir Welding (HFSW). Il processo di saldatura così definito nasce dall'unione della tecnica di saldatura allo stato solido FSW con l'aggiunta di una torcia TIG che ha il compito di preriscaldare il materiale prima del passaggio dello strumento, allo scopo di aumentare la velocità di saldatura e ridurre gli stress indotti nel materiale saldato. Nello studio vengono prese in considerazione alcune leghe di alluminio, su cui sono state effettuate saldature doppie e triple, volendo valutare il grado di difettosità presente nella zona di saldatura. Si è osservata inoltre la dimensione dei difetti riscontrati al variare di alcuni tra i parametri relativi alla torcia TIG (come la corrente impostata) e ritenuti significativi. Infine, si è visualizzato il rimescolamento, con trasporto di materiale, che avviene in seno al campione durante il processo di saldatura.

Introduction

High-resolution X-ray Computed Tomography (μ-CT) is a relatively recent non-destructive testing method which offers an attractive opportunity for the three-dimensional insight of the inner structure of objects and materials. Nowadays, due to the great technological advances and the computational power of modern calculators, μ-CT systems are massively employed for a wide range of purposes in the scientific and industrial sectors, whenever a correlation is required between the macroscopic behaviour of matter and its microscopic properties.

In order to extract from the tomographic data all the information necessary to the physical characterization of complex media, appropriated methodologies are required.

The overall objective of the present study is to define a procedure suitable for the characterisation of the materials microstructure exploiting the potentialities of the μ-CT technique. This involves several aspects, from the facility optimization, through the image acquisition, to the quantitative analysis of the reconstructed data.

This thesis has been carried out at the Elettra Synchrotron Radiation Facility (Trieste, Italy). Particularly, first I acquired the necessary experience on the tomographic method working at the hard X-ray imaging beamline of Elettra, the SYRMEP beamline.

It is proved that a synchrotron radiation monochromatic beam with parallel geometry is an ideal tool to perform quantitative studies about the sample mass density, morphology, phase mapping, in-situ imaging and dual-energy applications. However, the increasing interest in the μ-CT practice for industrial applications and its widespread applicability to a large variety of disciplines has brought to the need of overcome some intrinsic limitations of the SYRMEP μ-CT set-up, concerning the type and size of the samples that can be studied. The know-how developed in the SYRMEP group has

leaded us to design and realize a complementary state-of-the-art μ-CT system based on a micro-focus source: the TOMOLAB facility.

The TOMOLAB station has a flexible and open configuration: similarly to a beamline set-up, all the components can be substituted and upgraded, opening the way to new projects and experiments. Another important feature of the facility is that it has been specifically designed with the purpose of operating either in absorption or in phase-contrast imaging mode.

The first part of this dissertation will focus on the assembling, the testing and the characterization of the TOMOLAB facility.

In fact, the reliability of the obtained tomographic results as well as the global quality of the acquired data depends on the spatial resolution achieved with the machine which in turn is set by the technical features of the single components. Thus we will conduct a rigorous characterisation of the machine in order to fully exploit its capabilities. The activities devoted to the machine characterization will furnish useful results for the optimization of the working parameters. We will also carefully investigate the causes responsible for the image degradation, analyzing the main artefacts that concur in altering the image aspect, in order to improve both the acquisition and the reconstruction processes. The main effort will be done in order to eliminate, or at least to reduce, the causes of those artefacts (e.g. beam hardening, ring artefacts, uncertainness associated with the cone-beam geometry).

During my stay at Elettra, I had the opportunity to be involved in many different research projects in the field of material science and earth science, performed both at the SYRMEP beamline and at the TOMOLAB facility. Our research activity has been developed in collaboration with different research groups affording many different topics (geology, material science, engineering, archaeology). In all cases, the main effort was usually done to provide an effective support for the subsequent data processing.

In the past, the characterisation of three dimensional pore space and of the intrinsic texture of porous material has been based mainly on direct laboratory tests or pore filling procedures. The visualization and image analysis of the materials structure were often limited to bi-dimensional views, obtained via optical or surfaces methods. Nowadays, the extension of many concepts to the 3D case represents not a trivial task. We studied and developed specific procedures intended at the geometrical and morphological characterisation of the 3D microstructure. The procedures comprehend

both the operations dedicated to the improvement of the image quality (filtering equalization, etc.) and to the quantitative measurements and feature extraction. Practical examples will be furnished on a wide set of materials which we experienced during this thesis work.

Hereafter, a concise outline about the thesis organization will follow.

The first chapter will provide an introductive overview on X-ray μ-CT. The basic set-up of a μ-CT station will be described and fundamental notions on the data reconstruction process will be provided. Physical principles of X-ray production and interaction with matter will be also briefly illustrated. Finally, a description of the SYRMEP beamline at Elettra will be given.

The second chapter will furnish a detailed description of the TOMOLAB cone-beam μ-CT system. We will focus on the assembling phase of the machine, discussing the specific characteristics of the single components. We will illustrate the tests carried out during the commissioning time period in order to confirm the achievement of the foreseen targets. At the end of the chapter some preliminary imaging results will be reported that we obtained on test-objects, including several phase contrast images.

In the third chapter we will provide a characterization of the TOMOLAB imaging system on the basis of the real spatial resolution of the images related to mathematical parameters such as the point spread function (PSF) and the modulation transfer function (MTF), evaluated both on acquired radiographs and on the reconstructed slices. We will examine, giving practical examples, the typical artefacts appearing on the reconstructed slices. In this chapter we will define specific procedures to manage the deleterious effects of the main encountered artefacts.

In the fourth chapter advanced tools aimed at the intensive digital image processing of the acquired data will be introduced. We will present automated computer methods tailored for a wide range of applications, each one requiring its own customization. The PORE3D program will be presented: it is a custom-designed software package, developed within a collaborating project carried out at Elettra by Dr. Parnian Kasae and financed by the ICTP in the framework of a TRILL program. The software, developed on the basis of the practical experience we acquired on the tomographic datasets, is aimed at the extraction of quantitative measurements from the images. In this chapter, we will focus our analysis to the description of the 3D porous space via powerful tools like skeletonization and network characterisation. Since features extraction from 3D segmented images is generally a computationally heavy task, we calculate the skeleton

which reduces a digital object to a simpler version that still retains the essential features of the original one. At the end of the chapter, an interesting approach will be presented which allows extracting, on the base of morphological considerations only, the centred and shortest paths inside the pore space of a 3D complex media.

In the fifth chapter, three examples, selected among the many activities carried out at Elettra, will be presented. They concern μ-CT studies for material science which look rather representative. The first example will describe the development of semi-automatic digital image processing in order to obtain a geometrical and morphological characterisation of a light porous material as polyurethane foams employed for their acoustical and vibrational insulating properties. The second case will illustrate an innovative approach followed in order to characterize the resonance spruce wood microstructure, in order to model by means of a finite element method the acoustical behaviour of this material. The third application concerns a metallic material such as aluminium, demonstrating the capabilities of μ-CT coupled with image processing to reveal defects in hybrid-friction stir welding joints, thus guiding the optimization of the process parameters. In all cases, the main aim is to give an overview on the different applications, spread on a wide range of areas, in which the realized μ-CT facility, combined with the quantitative measurements performed by mean of the developed digital image processing tools, can successfully help the material investigation.

Chapter 1

X-ray computed tomography

X-ray computed tomography (XRCT or CT) is a relatively recent non-destructive testing (NDT) method which offers an attractive opportunity for the three-dimensional insight of the inner structure of objects and materials. Originally invented for medical diagnostics by Hounsfield in 1972, XRCT has been significantly improved and adapted to be used for industrial applications since early 1990's.

Nowadays, due to the great technological advances and the computational power of modern calculators, high-resolution X-ray computed tomography (micro-CT or μ-CT) systems are massively employed in a wide range of areas: from medicine to biology, from geology to archaeology, from mechanic and electronic engineering to material sciences, when a correlation is required between the macroscopic behaviour of matter and its microscopic properties.

In this introductive chapter an overview on X-ray μ-CT is presented. Physical principles of X-ray production and interaction with matter are briefly illustrated. Different methodologies are today available for μ-CT, capable to reach a micrometric spatial resolution on centimetric samples: the best results in terms of the achievable image quality are obtained employing third-generation synchrotron light sources as Elettra. A description of the SYRMEP hard X-ray imaging beamline at Elettra is given.

1.1 Micro-Computed Tomography

X-ray μ-CT is based on the same physical principles of medical CT but takes the advantage of an improved spatial resolution up to few micrometers. As the Greek words τόμος (slice) and γράφειν (to write) suggest, tomography is an imaging method consisting in the reconstruction of cross-sectional slices of the observed object. Micro-

CT directly descends from digital radiography based on the attenuation of X-rays interacting with the investigated matter.

The basic components forming a μ-CT system are the X-ray source, characterised by a micrometric or sub-micrometric focal spot size, the detection system, to collect the transmitted radiation emerging from the sample, and the sample positioning stages. The μ-CT scan is done recording on the detector, which is placed behind the sample, a set of planar projections while the sample rotates inside the incident beam over approximately the angular range between 0 and 180/360 degrees. A sufficient number of those angular views should be acquired at regular or known steps, in order to efficiently reconstruct a set of horizontal cross sections (the *slices*) of the object by mean of a well-established mathematical procedure known as the filtered back-projection (FBP) algorithm. It's worth mentioning that the rotation of the sample is a relative movement: in medical-like scanner the patient is stationary and the source-detector block rotates, while in tabletop facilities typically the sample is moved. Figure 1.1 illustrates the main components needed for μ-CT.

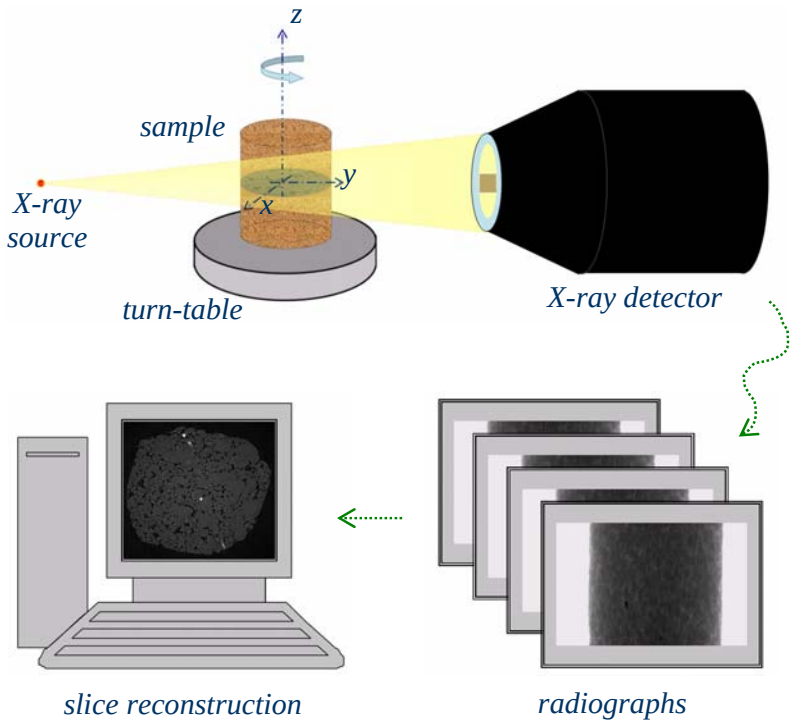

Figure 1.1 – Main components of a typical μ-CT set-up.

The ultimate product of the tomography process is the slice, which represents a virtual thin-section of the sample, whose thickness is strictly related to the achievable

spatial resolution. A grayscale value is assigned to each voxel[1] of the reconstructed slice, proportionally to the local X-ray attenuation map.

Once a set of consecutive slices is reconstructed, it is possible to create a three-dimensional digital data set of the sample just combining the slices into a stack (see Figure 1.2). This can be done for data visualization or volume rendering as well as for the detailed inspection of internal structures of the investigated object.

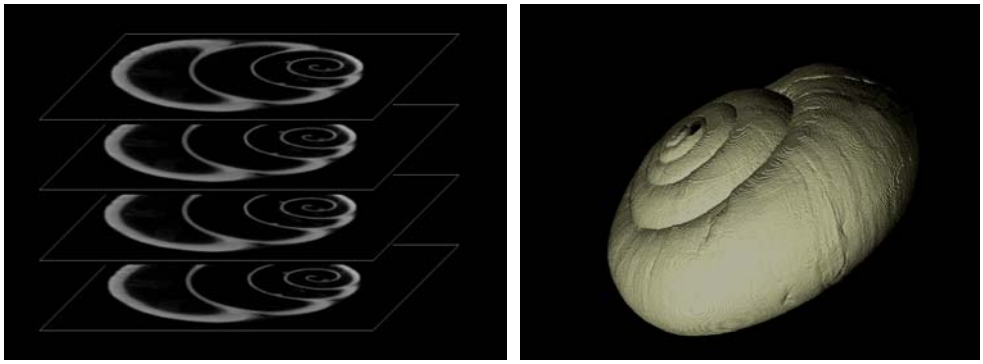

Figure 1.2 – Reconstructed slices of a snail-house (left) are used to create the 3D volume (right).

Actually, μ-CT doesn't require particular sample preparation, except to check that the object size fits the available field of view (FOV) of the detector. The experimental parameters instead should be optimized for the specific conditions. Once the radiographs are collected, the whole μ-CT process chain can be subdivided into three basic steps: the *pre-processing* includes all the operations that can be performed on the acquired radiographs in order to improve the image quality or prepare them to the reconstruction process (e.g. normalization, filtering or re-binning). The *processing* consists into the reconstruction process of the slices. Finally, because in most of cases numerical analysis of the reconstructed dataset is desirable, a *post-processing* step is usually necessary in order to extract quantitative measurements (e.g. morphological, geometrical or topological parameters) from the tomographic data by mean of specific tools offered by the different digital image processing (DIP) techniques.

Figure 1.3 describes the relevant aspects of the μ-CT (cone-beam) geometry. X-rays are generated by an ideal point-like source. For clarity, only the mid-plane is highlighted. The (x, y) coordinates system is rotating together with the investigated

[1] We refer to the voxel (volume element) as to the three-dimensional extension of the bi-dimensional pixel (picture element).

object, forming an angle ϑ with the source-to-detector path which is supposed to be the central ray of the beam. On the detector plane the projections of the sample are recorded onto the pixel grid having coordinates (u,v). The object axis of rotation z is aligned with the vertical axis v, i.e. with a pixel column of the detector.

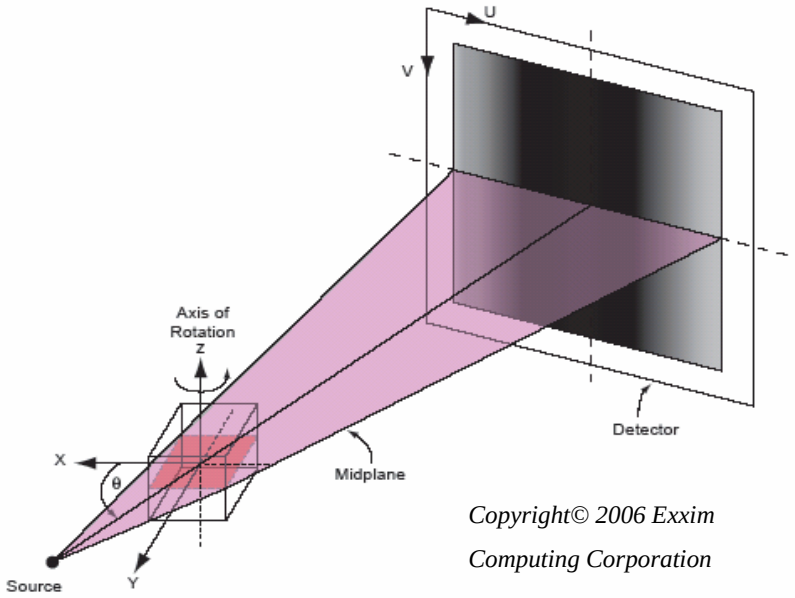

Figure 1.3 – Scheme of the μ-CT cone-beam geometry (from the Cobra User Manual v.5.0).

One of the advantages of working with such cone-beam geometry is the geometrical magnification of the projected sample as function of the mutual distances of the source, the object and the detector (D_{so} and D_{od} respectively). On the other hand the finite dimension of the source focal spot causes the blurring effect at the object contours: this is the reason for keeping the focal spot size as small as possible, in order to reduce the so called geometrical unsharpness intrinsically related to the penumbra zone surrounding the object contours, as better illustrated in Figure 1.4.

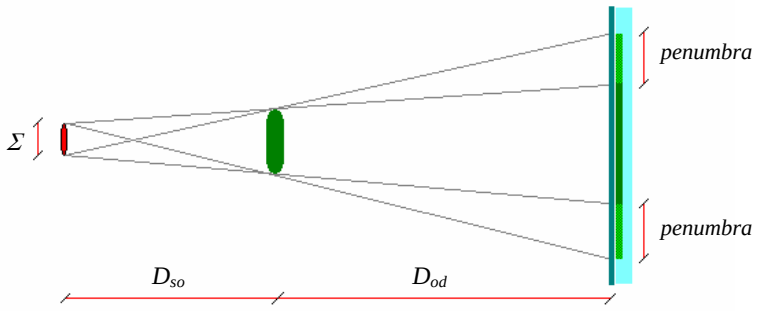

Figure 1.4 – The blurring effect at the object contours due to the finite size of the source focal spot.

Nowadays micro-focus X-ray source are routinely adopted for μ-CT systems allowing spatial resolutions of the same order as the focal spot size. As better discussed in the next, due to the cone-beam geometry, to set the achievable spatial resolution, the contribution of the focal spot size should be combined together with the proper detector pixel size. In particular, for larger geometrical magnification the focal spot size imposes the limit for the spatial resolution (Schena et al., 2005).

1.1.1 The slices reconstruction

Let's consider the reconstruction of a single slice from a set of projections acquired at different angles all around the sample. The simplest case for reconstructing this image is when the beam of X-rays is parallel. In this circumstance, the mono-dimensional projection of each cross-section of the investigated object should be transformed back into a bi-dimensional image, i.e. the slice (see Figure 1.5). Intuitively, as the transmitted X-rays are recorded onto the detector plane, it is then possible to obtain the slice from the information stored into each row of the detector.

In other words, for parallel beam geometry it is possible to reduce the reconstruction problem into the serial reconstruction of the two-dimensional slices from the one-dimensional shadow lines in the projections acquired at different angular views.

The reconstruction of the slices is done by the filtered back-projection algorithm (Kak and Slaney, 1987).

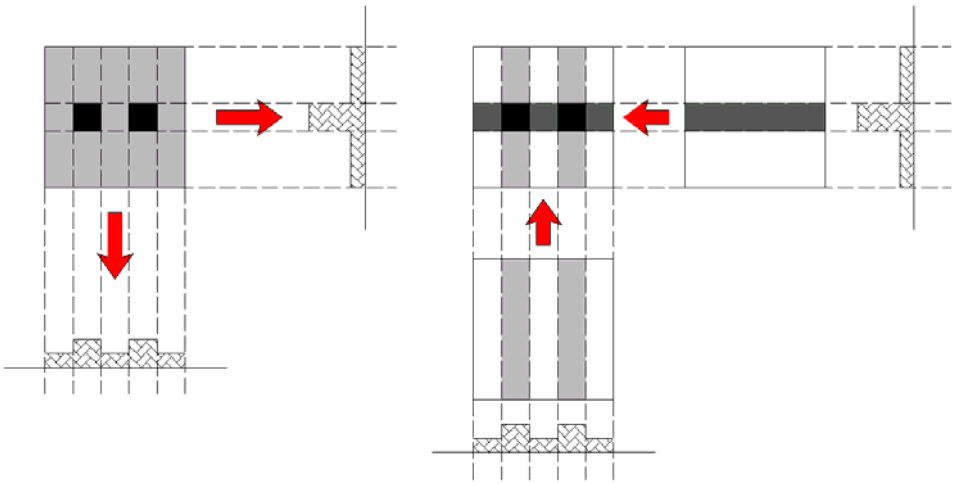

Figure 1.5 – The acquisition of the north-south and west-east projections onto the detector plane as line profiles of the transmitted X-ray photons (left). The reconstruction process is done back-projecting the acquired line profiles onto the slice plane (right).

The cone-beam geometry creates some additional difficulties for the reconstruction process, as the projections are now a function of many geometry-related parameters, e.g. the source angle, the horizontal and vertical positions on the detector plane. In this case, the algorithm that is currently widely used to reconstruct the slices is an extension derived from the FDK (Feldkamp, Davis and Kress, 1984) algorithm.

The filtered back-projection theory bases on the Fourier Slice Theorem. This theorem relates the Fourier transform of a projection to the Fourier transform of the object along a single radial line: thus, each projection represents a nearly independent measurement of the object, and the projections acquired at enough angles could be assembled into a complete estimate of the two-dimensional transform of the object. The last has to be inverse transformed in order to get the original object.

According to this theorem, in the frequency domain of coordinates (u,v) the polar version $P(\theta,u_\theta)$ of the Fourier transform of the projection at an angle θ corresponds to the bi-dimensional Fourier transform $F(u,v)$ of the object function:

$$P(\theta,u_\theta) = F(u,v) \qquad [1.1]$$

Thus the filtered back-projection algorithm states than the object function $f(x,y)$ can be then related to the inverse of the bi-dimensional Fourier transform weightened by the filter function $H(u)$:

$$f(x,y) = \int_0^{\pi} \left[\int_{-\infty}^{\infty} P(u_\theta) \cdot H(u_\theta)\, e^{j2\pi t u_\theta}\, du_\theta \right] d\theta = \int_0^{\pi} Q(\theta,t)\, d\theta \qquad [1.2]$$

where $Q(\theta,t)$ is the weigthened projection at an angle θ represented in the spatial domain. The rotating coordinate axis t is related to the (x,y) fix coordinate system (see Figure 1.3) by the following relationship:

$$t = x\cos\theta + y\sin\theta \qquad [1.3]$$

As the name implies, there are two steps in the filtered back-projection algorithm: the filtering part occurring in the frequency domain, which can be viewed as a simple weighting of projection's Fourier transform, and the back-projection part, which is equivalent to smearing each filtered projection over the image plane and can be readily done without excessive computational effort. Usually, a modified ramp filter is applied with the aim to cut off the highest frequencies, thus reducing the noise (e.g. the Sheep-Logan or the Ram-Lak filters are used).

However, a detailed description of such theoretical background is beyond the aim of the present thesis, and can be found in the related specific literature (Herman, 1980; Lewitt, 1983; Kak and Slaney, 1987).

Before continuing our discussion on the μ-CT methods, it could be useful to briefly introduce some physical aspects related to the X-rays production and their interaction with matter.

1.2 X-rays

1.2.1 X-rays production

X-ray radiation covers the wavelength range of 0.1 – 100 Å. The energy E of each X-ray photon is inversely proportional to its wavelength λ by the relation:

$$E = \frac{hc}{\lambda} \qquad [1.4]$$

where $h = 6.6261 \cdot 10^{-34}\ Js$ is the Planck's constant and $c = 3 \cdot 10^{8}\ m/s$ is the speed of light. Typical photon energies up to 140 keV are used for μ-CT.

In μ-CT the X-rays cone-beam used to illuminate the examined sample is generated by an X-ray tube: electrons are emitted at the cathode by a current heated filament and then accelerated inside the vacuum tube towards the anode by mean of the high voltage which is applied between the two electrodes. The anode represents the target material: when the electrons hit this target, an electromagnetic radiation is produced together with a large amount of heat (corresponding to around 99% of the total original kinetic energy of the electrons). The power of such a source is usually limited by the amount of heat that can be dissipated on the micrometric focal spot area by air or water cooling systems.

When an electron hits the anode target material, it can interact with the nucleus of an atom slowing down its speed while releasing its energy by the so-called Bremsstrahlung effect. This effect is responsible for the continuous part of the X-ray energy spectrum showed in Figure 1.6. But an incoming electron can also collide with an inner-shell electron of the target atoms, ejecting it. An outer-shell electron refills the vacant hole emitting X-ray photon with a particular energy equal to the difference between the binding energy of the two involved shells. Such effect therefore yield the characteristic peaks in the X-ray spectrum, which are clearly visible superimposed onto the continuous Bremsstrahlung spectrum. This radiation is usually referred to as the

characteristic radiation (or K-radiation) and is typical of each target material which is used. X-rays tubes represent the most diffuse way to generate X-rays.

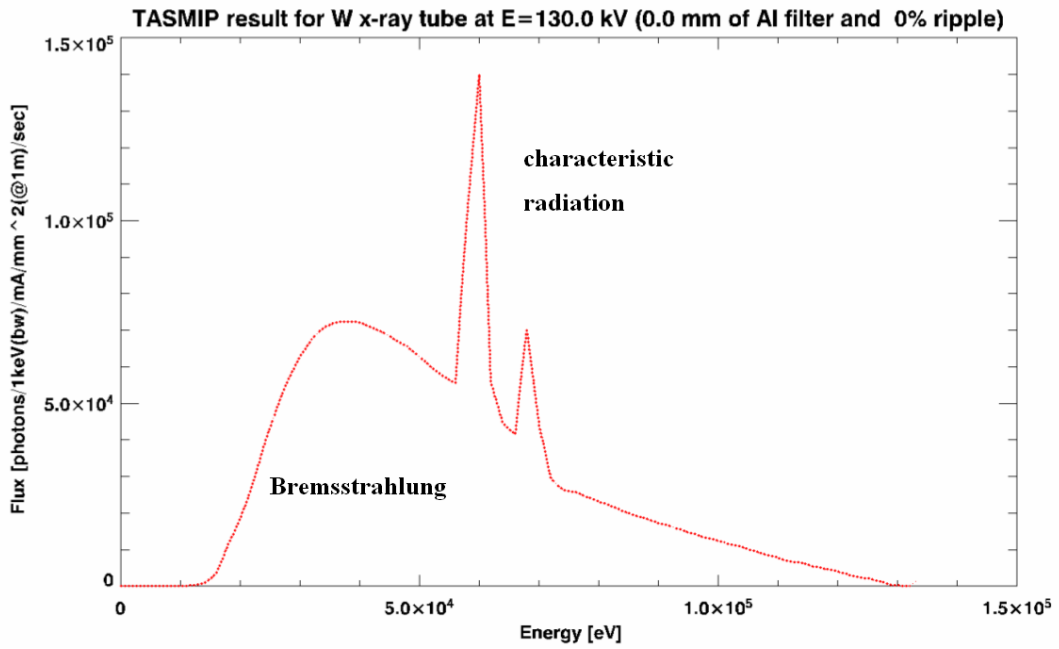

Figure 1.6 – The X-ray emitted spectrum of a tungsten anode tube (created with XOP 2.11).

However, the construction, during the last decades, of third-generation synchrotron facilities has opened the way to the possibility of synchrotron light radiography, of great interest to investigate materials and soft matter due to the characteristics of the radiation delivered by the photon source. At synchrotron radiation facilities electrons are stored in bunches inside a vacuum ring (the so called storage ring) and forced to travel in a closed loop by strong magnetic fields. When the particles are accelerated perpendicular to their travel direction by bending magnets or wiggler devices, the synchrotron radiation is emitted tangentially to the storage ring (see Figure 1.7).

Because part of the μ-CT experiments presented in this thesis was conducted at the third generation Elettra Synchrotron Radiation Facility, we introduce the peculiar aspects of this kind of sources for X-ray imaging.

These aspects are associated to the high energy and low emittance[2] of the electron beam. This allows to study heavy or bulky samples in transmission geometry, and to perform *in-situ* or *real-time* (at the temporal scale of about 0.1 sec) experiments. Indeed,

[2] The emittance is defined as the product between the size of the electron beam and its divergence.

the low emittance implies that the source dimensions are reduced with respect to the older generation synchrotron facilities and, due to the high distance between the source and the experimental hutch, the *geometrical* resolution R of the images, given by:

$$R = \frac{D_{od} \cdot \Sigma}{D_{so}} \qquad [1.5]$$

is significantly improved. In the formula Σ is the vertical source size. As a consequence, from an experimental point of view, the beam geometry can be considered approximately parallel, thus allowing observing details in the images with a high spatial resolution (of the order of few micrometers) for D_{od} higher than 1 meter. Furthermore, this reduces the geometrical constrains for *in-situ* experiments when a cumbersome apparatus surrounding the sample is used (i.e. cryostats, ovens, mechanical testing machines).

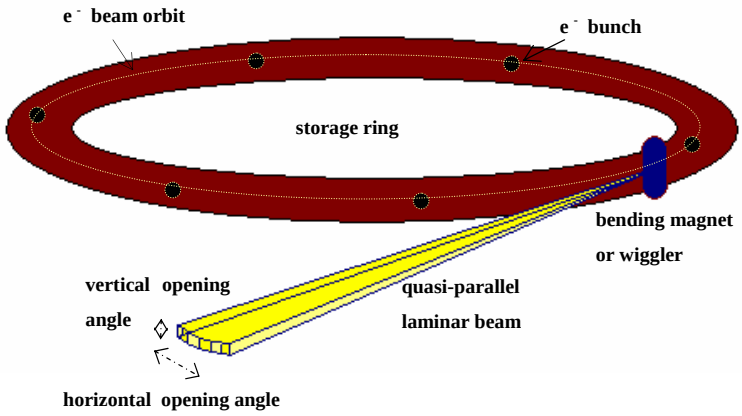

Figure 1.7 – A laminar shaped beam coming out from a bending magnet.

The parallel geometry of the laminar shaped beam simplifies the slices reconstruction and reduces the geometry-related artifacts that classical cone-beam μ-CT usually introduces. The other peculiar characteristic, which represents a major advantage of the synchrotron light, is that, due to the very high brilliance[3] of the produced beam, a monochromator can be inserted into the beam trajectory which allows a precise tuning of the photon energy according to the thickness and composition of the sample.

[3] The brilliance is defined, for any given energy, as the number of photons/sec/mm^2/mrad^2.

1.2.2 X-rays interaction with matter

Traditional absorption μ-CT provides a 3D distribution map of the linear attenuation coefficient μ of the investigated matter, which is related to the local density ρ, the atomic number Z of the contained elements and strongly depends on the beam energy E too. The following expression correlates the number of X-ray photons I_0 that enter the investigated object to the number I of those that leave after traversing a path long ℓ inside the object thickness:

$$I = \int_E I_0(E)\, e^{-\int_\ell \mu(s,E)ds}\, dE \qquad [1.6]$$

where the external integral is done on the whole energy spectrum emitted by the specific X-ray source. Under the assumption that a monochromatic X-ray beam is emitted equation [1.6] can be simplified. In such a case the Beer-Lambert law states that:

$$I = I_0\, e^{-\int_\ell \mu(s)ds} \qquad [1.7]$$

As one can observe rearranging equation [1.7] a line integral of X-ray attenuation is the log of the ratio of monochromatic X-ray photons impinging the object to the transmitted ones:

$$\int_\ell \mu(s)\, ds = -\ln\left(\frac{I}{I_0}\right) \qquad [1.8]$$

In order to eliminate the density dependency of μ, usually the so called mass attenuation coefficient μ/ρ is considered instead of the simple μ.

In the energy range used for μ-CT two fundamental physical processes dominate to attenuate the incoming X-rays, as Figure 1.8 illustrates. The first one is photoelectric absorption which dominates at the lower energies (up to 50–100 keV), the second is Compton scattering which dominates at the higher energies.

By the photoelectric effect the incoming X-ray photon transfers its whole energy to an atomic electron from the inner-shell of the interacting atom, which is ejected: another electron from the outer-shell will replace the removed electron, while electromagnetic energy is emitted. By Compton mechanism the incoming photon yields part of its energy to an outer-shell electron, which is ejected from the atom while a scattered photon with lower energy emerges deviated from its original trajectory.

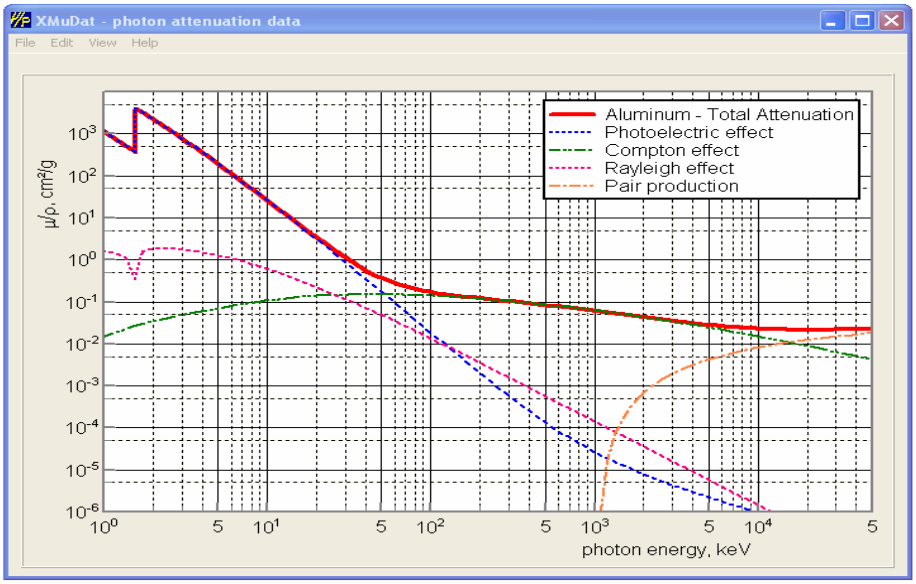

Figure 1.8 – The contribution of different attenuation mechanisms (calculated for aluminium with XMuDat 1.0.1 by Robert Nowotny).

Different materials reveal different values of μ/ρ, allowing distinguishing them in the reconstructed images, as illustrated in Figure 1.9 for aluminium and carbon graphite.

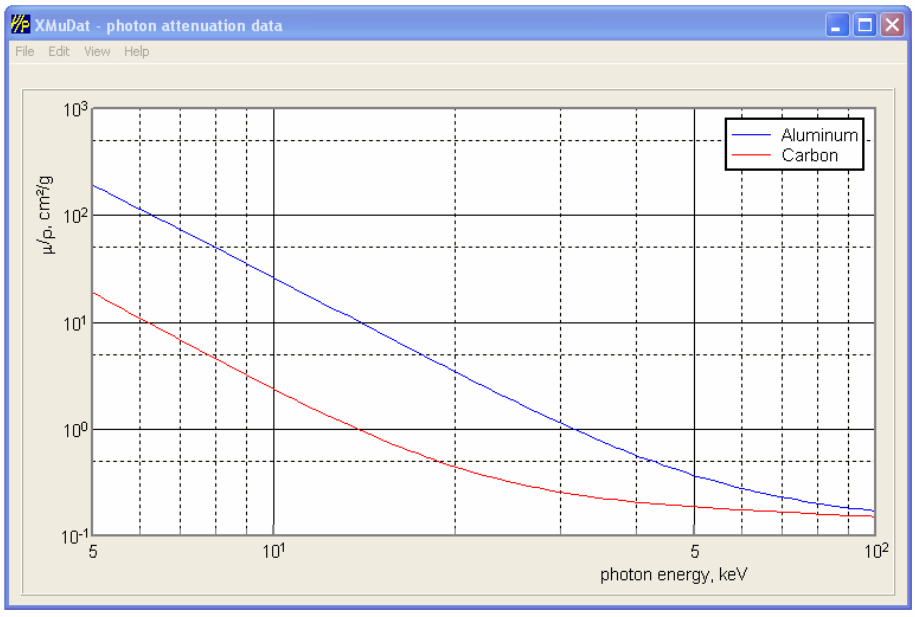

Figure 1.9 – The mass attenuation coefficient as a function of the energy for aluminum and carbon.

However, approaching the Compton domain one can assume that μ/ρ is weakly dependent on photon energy E. As a consequence, by purely absorption tomography

two elements are no more distinguishable at the higher energies. The low-energy X-rays instead appear much more sensitive to the density variances and this helps to enhance the absorption contrast between the elements. Other possibilities can be exploited to discern between similar attenuating elements or also to reveal poor attenuating materials when the whole incident radiation is transmitted: such a methods lie in the phase contrast (PHC) imaging and the phase retrieval imaging, as better discussed in the next paragraphs.

1.3 The SYRMEP beamline at Elettra

The hard X-ray imaging beamline at Elettra, where part of the experimental thesis work has been carried out, is named SYRMEP (SYnchrotron Radiation for MEdical Physics). This station has been designed in cooperation with the University of Trieste and the National Institute of Nuclear Physics (INFN). It was originally devoted to investigate and develop innovative techniques for medical imaging and recently, thanks to the upgrades of the experimental set-up and of the procedures for the three-dimensional data processing, a parallel research activity in material science, involving also μ-CT, has been introduced.

The light source, having a vertical size Σ (full width at half maximum - FWHM) of about 100 μm, is produced by the electrons deviated from their straight path by the magnetic field of a bending magnet. The beamline is basically made up by:

- the optic hutch where the X-ray beam is prepared (energy selection, geometry definition and intensity modulation) for the specific application;
- the experimental hutches where the sample and the instrumentation are placed for investigation;
- the control room.

As illustrated by the sketch of Figure 1.10, the main components of the optic hutch of the beamline are the entrance vacuum slits systems, the double-crystal Si (111) monochromator and the exit air slits (Arfelli et al., 1993). The optical elements are inserted between a couple of beryllium windows: the first one divides the beamline from the storage ring, the second one separates the vacuum propagating part of the beam with the air propagating one. The lower energy components of the beam are cut traversing the first beryllium thickness.

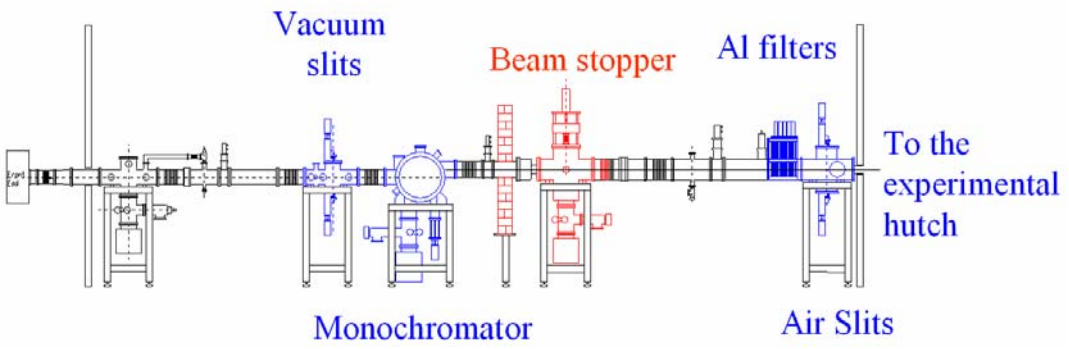

Figure 1.10 – Sketch of the layout of the SYRMEP beamline.

Furthermore, a thick block of tungsten, the so called beam stopper, controlled by a pneumatic piston, can be inserted into the beam to prevent the beam reaching the experimental hutch. A set of aluminium foils of different thickness can be selected to pre-filter the incident beam thus lowering the available flux at the sample when required by the experimental conditions.

In the experimental hutch there are the ionization chamber (to continuously measuring the incoming photon flux), the sample holder, endowed with 4 degrees of freedom and the turn-table on the top, and the detectors for image acquisition (see Figure 1.11).

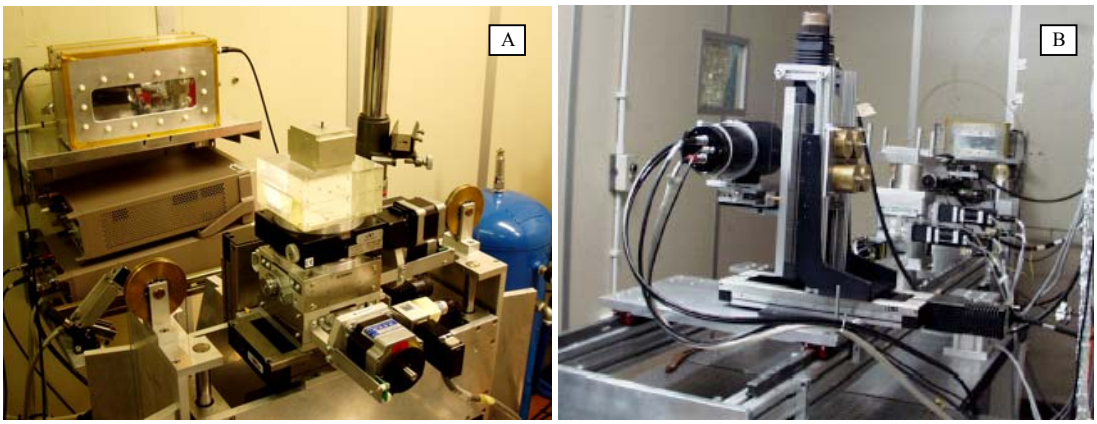

Figure 1.11 – The experimental hutch of the SYRMEP beamline. The ionization chamber is portrayed together with a specific setup for μ-CT measurements mounted on the turn-table (A). The CCD camera can move forward and back along the railway (B) together with its horizontal and vertical motor stages.

The monochromator works in an energy range between 8.3 keV and 35 keV, covering the entire angular acceptance of the beamline (i.e. 7 mrad) in Bragg configuration. The beamline provides at a distance of about 23 m from the source, a monochromatic, laminar-section X-ray beam with a maximum area of about 160x6

mm^2, measured as the FWHM of Gaussian vertical and horizontal profiles across the beam.

The described technical features of the beamline provide a geometrical resolution R (calculated by equation [1.5]) of about 0.4 μm at the D_{od} of 10 cm.

High quality images can be acquired by two charge coupled device (CCD) cameras available at the SYRMEP beamline: the first one is a wide dynamic range 16 bit water cooled 2048×2048 pixels, with a pixel size of 14 μm, that can be coupled with different optics allowing to work at different spatial resolutions: a point spread function[4] (PSF) of about 13 μm with a FOV of 7.8 mm × 7.8 mm was measured, and of about 30 μm with a FOV of 28 mm × 28 mm. The second camera is a new conception 12/16 bit CCD, with a very short read out time, allowing halving the time of each tomographic acquisition. The camera is water cooled too with 4008×2670 pixels and a pixel size of 4.5 μm. Calculated spatial resolution (PSF) is around 13 μm with a FOV of 18 mm × 12 mm. The setup for μ-CT allows performing measurements on samples having lateral dimensions slightly lower than the horizontal FOV of the CCD cameras, while different devices can be mounted on the turn-table and/or around the investigated sample for any particular *in-situ* measurements.

1.3.1 Phase contrast radiography

Although conventional X-ray imaging bases on the absorption contrast due to the interaction of X-rays with matter, phase shifts occurring at the X-rays wave-front can be also revealed. This effect is produced by the path-length variations of the X-rays travelling within the sample. The refractive index n may be written as:

$$n = 1 - \delta - i\beta \qquad [1.9]$$

where δ is the real part and β the imaginary one. In absorption mode emphasis is given to the imaginary component $i\beta$ (related to linear absorption coefficient of the material), while in PHC mode the deviation from unity of the real part δ of the refractive index becomes significant.

[4] The PSF, representing the impulsive response of an imaging system, is generally used to estimate the spatial resolution.

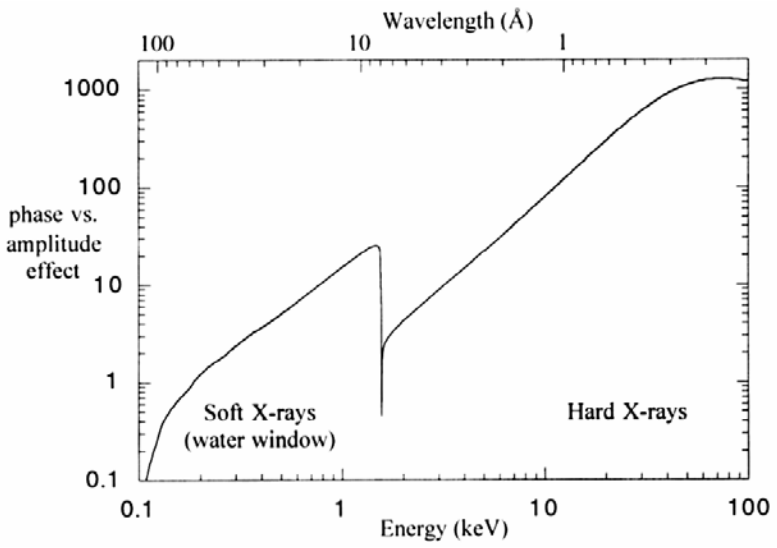

Figure 1.12 – Ratio δ/β of the refractive index decrement and the absorption index as a function of the X-ray energy for the aluminium element.

Both δ and β are small, typically of $10^{-5} \div 10^{-6}$ and $10^{-8} \div 10^{-9}$ respectively for light materials, indicating the power of phase-contrast imaging compared to the X-rays absorption. Figure 1.12 shows the ration δ/β, as a function of the X-ray energy for aluminium. The energy range includes soft and hard X-rays. In the hard X-ray range (energies above 6 keV) this ratio increases with energy to huge values[5] (up to 1000). Practically, selecting an energy of 25 keV to pass a thick aluminium sample, a hole in this metal should have a diameter of at least 20 μm to produce 1% of absorption contrast while in the same situation exploiting the effects of the phase the minimum detectable hole size is around 0.05 μm (Baruchel et al., 2000).

Thus the PHC radiograph is extremely precious for the investigation of details inside the materials exhibiting a small absorption with respect to hard X-rays, but producing significant variation of the optical path length. This is the reason why we applied the PHC on samples presenting heterogeneities inside the volume of the sample.

In the common experimental practice of in-line phase contrast imaging, free space propagation transforms the phase modulation of the transmitted beam into an amplitude

[5] In fact δ varies as a function of the wavelength as λ^2, whereas β as λ^4, so that the relative weight of δ increases with the energy (Mayo et al., 2002).

modulation, when the wave is allowed to propagate beyond the sample enough for Fresnel diffraction to occur (see Figure 1.13).

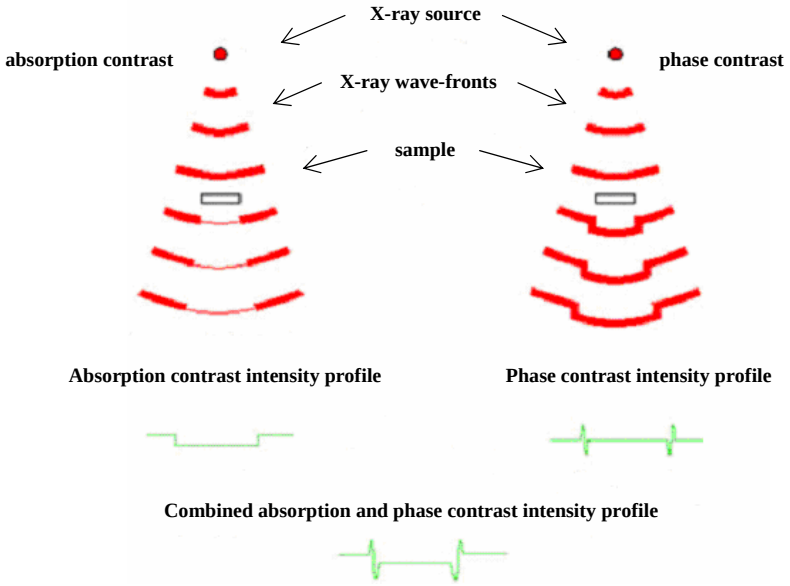

Figure 1.13 – Scheme of the combined effect of absorption and PHC on the propagating front wave.

A position-sensitive detector can be set at a distance D_{od} from the sample. It's worth noticing that a purely absorption-based image is possible, in principle, only on the object plane (i.e. where the object-to-detector distance D_{od} is zero), whereas a phase contrast image occurs throughout the entire Fresnel region (Bronnikov, 2002). According to the choice of D_{od} with respect to the size a of the feature to be identified perpendicularly to the beam direction, one may discriminate between two different regimes: the edge-detection regime ($D_{od} << a^2/\lambda$) and the holography regime ($D_{od} \approx a^2/\lambda$), where λ is the X-ray wavelength (Cloetens et al., 2001). The edge detection regime can be used directly to extract morphological information once standard tomographic reconstruction technique is applied. The PHC results we will present in the next chapters refer to data acquired in the edge-detection regime. At SYRMEP it is possible to work at variable sample-to-detector distances from few millimetres up to about 2.5 metres.

It's worth observing the simplicity of the implementation of this technique when a transversal coherent X-ray beam is available, which means that the amplitudes of the travelling X-rays waves are highly correlated between different points transverse to the direction of propagation (Wilkins et al., 1996). This condition can be achieved by using

a small source size (like laboratory microfocus sources) or a source with a small angular size (synchrotron source).

The lateral coherence length L_c can be defined by the formula:

$$L_c = \frac{\lambda \cdot D_{so}}{2\Sigma} \qquad [1.10]$$

In the last decade considerable advances have been made towards the achievement of a high degree of spatial coherence using both laboratory-based X-ray sources and synchrotron ones (Wilkins et al., 1996; Stevenson et al., 1999). In the case of third-generation synchrotron sources such as Elettra it is possible to obtain X-ray beams with a high degree of coherence. At the SYRMEP beamline a typical value of L_c at 15 keV is about 10 μm. This value is extremely high with respect to older synchrotron facilities; for instance at the ID25 beamline of LURE (Orsay, France) L_c was on the order of 0.5 μm (Mancini, 1998). An intermediate value can be obtained by using a modern microfocus source. In this case, we consider 2Σ as the diameter of the focal spot size: at the energy of 35 keV, with a focal spot size of 5 μm and $D_{so} = 0.3$ meters, we obtain a value of L_c around 2 μm.

Quantitative measurements are possible in the holographic regime, combining the classic tomographic reconstruction algorithm with the so called phase retrieval method, based on the use of few images recorded at different distances from the sample to recover the phase shift from the diffracted intensity distribution in the image plane (Beckmann et al., 1997; Donnelly and Price, 2007).

The phase contrast method was pioneered by Ando and coworkers since 1970s and has later produced phase imaging and tomography results in many application fields such as medicine for the investigation of bones (Xu et al., 2001) and soft tissues (Momose et al., 1995) as well as study of plant roots (Moran et al., 2000) and material science (Stevenson et al., 2003). Although phase-contrast improved the reconstructed imaged from a qualitative point of view, the lack of a mathematical theory of reconstruction comparable with that of conventional absorption tomography limited the quantitative measurements on the reconstructed data (Bronnikov, 2002).

In its simplest form, in-line phase-contrast imaging provides images of samples in which edges and boundaries are enhanced by near-field Fresnel diffraction. The phase contrast mode allows to successfully identify tiny high spatial frequency features (i.e., smaller than the pixel size) which cause a sharp separation interface between objects

showing little density's variation. Typically by phase contrast technique structures as cracks, voids and surface texture, generally not detectable by traditional absorption tomography, can be visualized and investigated.

Conclusion

By this introductive chapter the reader has been introduced towards the tomographic technique, purchasing the basic concepts about X-ray μ-CT: the physical background of X-ray production and interaction with matter was briefly pointed out and the tomographic scheme illustrated both from the acquisition point of view and from the slice reconstruction one.

It is proved then synchrotron μ-CT provides nowadays the best image quality, due to the many advantages of this X-ray source with respect to conventional sources. Indeed, a synchrotron radiation monochromatic beam with parallel geometry is an ideal tool to perform quantitative studies about the sample mass density, morphology, phase mapping, in-situ imaging and dual-energy applications.

The increasing interest in the μ-CT technique for industrial applications and its widespread applicability to a large variety of disciplines has brought to the need of overcome some intrinsic limitations of the SYRMEP μ-CT set-up concerning the type and size of the samples that can be studied.

The know-how developed in the SYRMEP group has leaded us to design and realize a complementary state-of-the-art μ-CT system based on a micro-focus source: the TOMOLAB facility.

This will be the subject of the next chapter of this thesis.

Chapter 2

The TOMOLAB X-ray CT laboratory

In this chapter we will present the cone-beam μ-CT system which was designed and developed at Elettra: a detailed description of the facility, named TOMOLAB, is furnished. An overview of the tomographic set-up is given and the specific characteristics of the instruments are discussed.

The TOMOLAB facility has a flexible and open configuration: similarly to a beamline set-up, all the components can be substituted and upgraded, opening the way to new projects and experiments. Another important feature of the facility is that it has been specifically designed with the purpose of operating either in absorption or in phase-contrast imaging mode.

Because the choice of the single components is fundamental to set the effectiveness of the entire system, the selection of an appropriate source and detector for the desired particular applications was done in order to achieve the optimal combination between the image resolution, the field of view (FOV) and the data acquisition time.

In this chapter we will focus on the assembling phase of the machine and the following commissioning time period devoted to test and confirm the achievement of the foreseen targets. At the end of the chapter some preliminary imaging results are reported that we obtained on test-objects. Moreover, phase contrast images will be showed to demonstrate the capabilities of the facility on this topic.

2.1 The facility

The TOMOLAB facility (http://www.elettra.trieste.it/Labs/TOMOLAB) was created through a project involving Elettra and the University of Trieste. The main idea was to create a μ-CT system complementary to the SYRMEP beamline of Elettra.

A new conception laboratory was then designed based on a cone-beam μ-CT station equipped with a sealed micro-focus X-ray tube. Designing such an open and flexible tomographic facility revealed as a very attractive benefit for many applications with reference to the scientific research as well as to the industrial area, in particular when a monochromatic and coherent beam is not needed. The higher penetrating power of the X-rays produced at TOMOLAB make them capable to traverse thicker samples in comparison with those ones analyzed at the SYRMEP beamline. At the same time the larger field of view available, together with the wide cone-beam, allows to image bigger samples at once.

At the TOMOLAB station the basic components (i.e. the X-ray source, the detection system and the sample positioning motors) are placed into a lead shielded cabinet, thick enough in order to attenuate the maximum energy emitted by the adopted X-ray source. The cabinet (2×1×1 meters) has a door on the front side, in order to routinely access to the sample, the motors and the CCD. Motors consist mainly into two high-precision translation stages (x and z axis) and a rotation stage. Both the motors and the CCD are mounted on two separate carriages that can slide on a Bosch guide rail translating along the source-to-detector axis (see Figure 2.1).

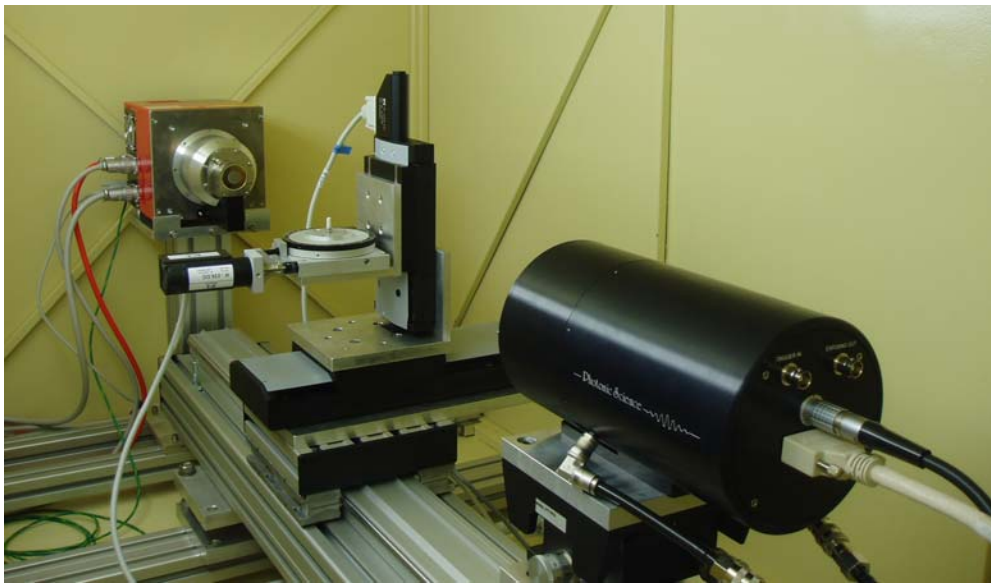

Figure 2.1 – Internal appearance of the TOMOLAB station.

To easily and accurately set the desired magnification factor for a specific experiment, according to the mutual distances between components, one can rely on a graduated stick which is placed on to the front side of the guide rail (see Figure 2.2). The magnification factor M is then given by the formula:

$$M = \frac{D_{sd}}{D_{so}} \qquad [2.1]$$

where D_{sd} is the source-to-detector distance and D_{so} is the source-to-object one.

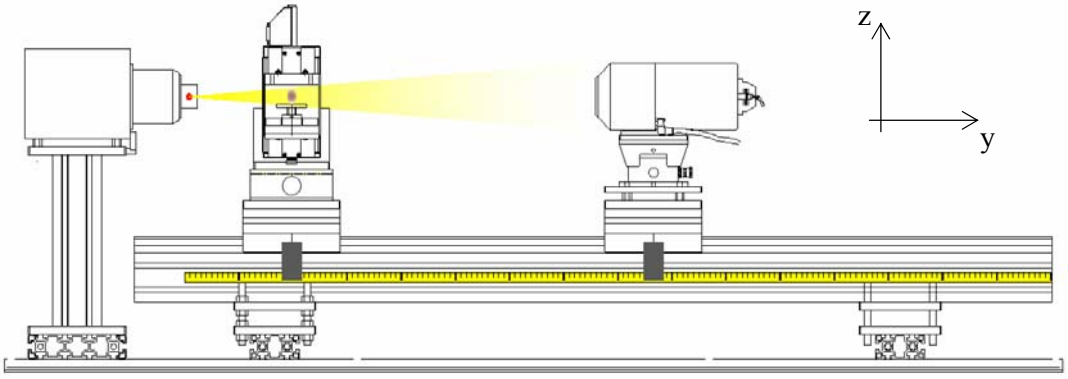

Figure 2.2 – Scheme of the instruments placed inside the TOMOLAB station.

Under the motors and the CCD carriages a rectangular plate is hanged, which is used to exactly evaluate their position. The values that can be read for D_{sd} and D_{so} take into account the actual position of both the focal spot of the source (approx. 13 mm behind the tube external surface) and the precise position of the CCD grid inside the detector. The object rotation axis is considered to be placed exactly in the centre of the turntable.

Among the advantages of a home-built facility it's worth mentioning the possibility to accommodate inside the cabinet, and thus to scan, objects having a wide range of shapes and sizes. Similarly, special devices or external equipments can be introduced inside the cabinet to satisfy particular experimental conditions (e.g. temperature controlled tests, stress-strain monitoring, real-time fluid injection, forced magnetic fields or other specific needs). However the cone-beam geometry, when compared with the parallel beam delivered at synchrotron beamlines, poses some limitation to this topic. In fact, before placing any special device surrounding the sample - which eventually interposes between the source and the object during the tomographic scan - , one should consider the dependency of the resolution with the source-to-object distance, if this distance is increased to locate the device.

In μ-CT the only request for the examined sample and its container is to fit the FOV of the CCD camera. In principle in fact the tomographic reconstruction is still possible when part of the specimen exceeds the FOV, by applying the so-called local tomography technique (Ohgaki et al., 2007), but this particular aspect is beyond the scope of this dissertation and will not be discussed in the next. The examined samples

should have preferentially a cylindrical profile, because this represents the most adaptable shape to fit the FOV, even if there are absolutely no limitations for other irregular shape which eventually can be further enveloped into a regular container to simplify the scan alignment or reduce the geometry-related artefacts (Davis and Elliott, 2006).

The external appearance of the station is shown in Figure 2.3: a shelf is placed under the cabinet to accommodate the power supplies of the components, the cables and other external devices useful for the control of the instruments. The basic skeleton of the structure is made of a steel frame on which individual sheets of lead are attached, accurately welded together and superimposed at junctions to avoid the formation of holes, and then painted on both the sides. On the bottom of the cabinet, holes were foreseen to pass the electrical cables needed by the instruments: to eliminate any non tolerable X-ray leaching, the holes were protected by extending lead shielded pipes toward the exterior of the cabinet. To further guarantee personnel and users to safe operate at the laboratory, the X-ray radiation was monitored by a Geiger counter during the normal tomographic conditions and when the maximum power is emitted by the X-ray source, with particular attention close to the holes on the bottom of the cabinet and all around the front door. The measured level is everywhere compatible with the fluctuation range of the environmental residual dose.

Figure 2.3 – External appearance of the TOMOLAB station.

An environmental dosimeter is permanently fixed onto the external front wall, with respect to the X-ray source, where the most part of X-rays is supposed to impinge.

In order to facilitate the first positioning of the main instruments inside the cabinet and to favour other extraordinary maintenance operations, the lead cover of the cabinet can be removed thus allowing to the technicians a comfortable access from the top.

A safety lamp is placed on the top of the cabinet, lightening when the X-ray source is on. An electrical box is placed on the bottom shelf which provides all the electrical connection to the lights, the control PC, the safety interlock circuits and the other components of the TOMOLAB station. A water flow cooling system is visible on the bottom-right side of the cabinet, which is necessary to cool the CCD camera.

The TOMOLAB facility is equipped with a control PC and a powerful workstation for the slices reconstruction, the 3D visualization and the further data processing of the acquired data. The control PC is exclusively dedicated to command the different components (X-ray tube, CCD, motors, webcams etc). From the control PC the planar images collected by the detector are then transferred to the workstation via a fast LAN cross connection (Gigabit Ethernet). The workstation is a Dual Core AMD64 Opteron Processor with 2.00 Gb of RAM, working under Microsoft Windows XP Pro x64 Edition. These characteristics were chosen to guarantee the best performance of the commercial software used for the reconstruction. Actually, the acquired tomographic data are reconstructed on a high performance graphic card (NVIDIA GeForce 8800 GTX, based on a GPU architecture). Slices can be then locally saved on a 500 Gb hard disk until their final transfer to a definitive storage.

With the described configuration a cubic volume of 2004×1335×1000 voxels can be reconstructed in less than one hour from a set of 900 projections.

2.1.1 The X-ray source

The cone-beam employed at the TOMOLAB desktop facilities is generated by a sealed X-ray tube: in such apparatus, electrons emitted at the cathode by a current heated filament are accelerated towards a stationary anode by mean of the high voltage field applied between the two electrodes. The anode represents the target material: when the electrons hit the target, an electromagnetic radiation is produced together with a large amount of heat. The power of the source is generally limited by the amount of heat that can be dissipated at the anode - which has to be kept very small - by air or water cooling systems.

Figure 2.4 – The Hamamatsu L9181S X-ray tube.

TOMOLAB is furnished with a *Hamamatsu L9181S* tube with micrometric focal spot size (5 μm are assured operating at 4 W, while the maximum achievable power is 39 W), which can operate at a maximum voltage of 130 kV and a maximum current of 300 μA. The number of photons emitted per unit of time is controlled by the cathode current (usually expressed in μA). The energy of the emitted photons (expressed in eV) is controlled by the tube voltage (expressed in kV). The polychromatic emitted spectrum is showed in Figure1.6.

The X-ray tube was mounted separately from the other components, fixed at the top of a Bosch column, in order to provide an adequate isolation against vibrations under the normal operating conditions.

Other significant specific parameters of the X-ray tube are summarized in the following table.

Parameter		Value/Description	Unit
X-ray Tube		Sealed Type	-
Cooling Method		Forced Air Cooling	-
Window Material		Beryllium	-
Target Material		Tungsten	-
Window Position		End-window	-
Target Voltage		40 to 130	kV
Target Current		0 to 300	μA
Maximum Output Power		39	W
Focal spot Size	Small Spot Mode	8 (@ 8 W), 5 (@ 4 W)	μm
	Middle Spot mode	20 (@ 16 W)	μm
	Large Spot Mode	40 (@ 39 W)	μm
Beam Angle (Maximum)		100	degree
Minimum Distance Focus/Object		13	mm
Operation		Continuous	-
Focal length from outer surface of enclosure		13	Mm

Table 2.1 - Technical characteristics of the Hamamatsu L9181S X-ray source.

The cone-beam geometry is generated when X-rays exit from an end-window made of a Beryllium foil. The source is powered by an external power supply.

It's worth mentioning that the reported focus-to-object distance of 13 mm represents the distance between the focal spot and the exterior side of the output window, thus it corresponds to the minimum distance at which one can place the object: this parameter can be of great importance when considering the optimum magnification factor achievable for that machine (it should be small enough in order to reach high magnification values while keeping high the photon flux). In fact, placing the sample closer to the detector reduces the blurring due to the X-ray focal spot size. On the other hand, increasing the X-ray source-to-detector distance decreases the X-ray photon flux resulting in longer data-acquisition times or poorer contrast resolution.

As previously mentioned, to prevent accidental exposure to ionizing radiations the X-ray cabinet was designed and equipped with two safety interlock circuits and a safety lamp on the top of the cabinet lightening during X-ray emission. The source has got an automatic wattage control which works during the middle and small focal spot regimes limiting the maximum wattage achievable. Tube current stability is not guarantee at tube voltages below 40 kV.

2.1.2 The detector

A CCD consists of a silicon wafer patterned in the manner of integrated circuits into a rectangular grid of voltage adjustable capacitors, called gates, on which electrical charge can be stored, and among which charge can be shifted around. The signal produced by a CCD is a rectangular array of voltages, each of which is proportional to the number of photons collected in a certain element, i.e. the *pixel*, of the image.

X-rays need to be converted into visible photons in order to be revealed on the CCD: conversion involves stopping the X-ray photons by a so called scintillator screen, e.g. a phosphor or semiconductor layer. Then, various coupling methods, e.g. lenses or fiber optics, are adopted to transfer the visible photons to the CCD, where they are finally converted into electric charges. During the so called read out time, such electric information is transferred via an ADC (analog to digital converter) unit from the detector to a storage medium as a digital image file.

The TOMOLAB facility is equipped with a high resolution X-ray sensitive CCD detector (FDI VHR Camera by Photonic Science, see Figure 2.5).

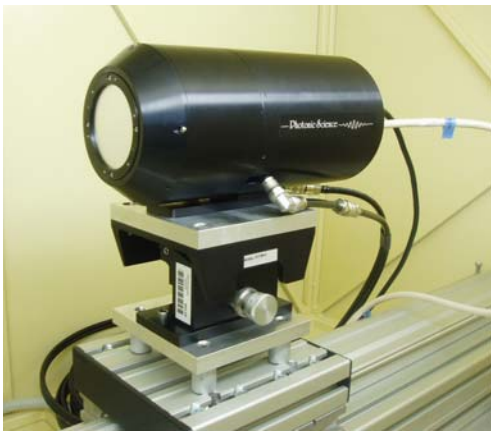

Figure 2.5 – The Photonic Science FDI VHR Camera.

It provides a really good combination between a large field of view (4008×2670 pixels) and small effective pixel size (12.5 microns square). The CCD is optically bonded to a tapered fiber optic which gives a magnification factor of 1.39× and an input active area of approximately 50×33 mm. On the front of the taper a GADOX scintillator (Gd2O2S:Tb)[1] layer is deposited in order to make the detector optimized for resolution with X-ray energies in the range given by our source.

The thickness of the screen, given by the areal density divided by the mass density of the phosphors, can be optimized. The useful thickness of a luminescent screen is largely a compromise between its X-ray conversion efficiency and its spatial resolution. The scintillator screen is always the bottle-neck limiting the achievable spatial resolution of the detection system. Moreover, also the coupling of the scintillator screen with the CCD array via a fiber optic bundled taper (magnifying or de-magnifying) is a delicate process, introducing some degradation of the overall spatial resolution.

The CCD used at TOMOLAB has a very high readout rate, which is a great benefit when several images are to be taken during the tomographic scan. In its standard mode the detector produces 12 bit digital images data. It is however possible to extend the dynamic range thus producing, by multiple acquisitions, a true 16 bit image.

[1] The phosphor layer in the screen typically contains a rare earth element such as Gadolinium (Gd) suspended in a polymer matrix. Commonly the screens contain Terbium-doped Gadolinium Oxysulphide (Gd2O2S:Tb) which emits light in the green part of the spectrum at 540 nm. Since Gd has a K-edge at 50 keV, absorption of X-rays via photoelectric interactions is very efficient.

The CCD is cooled by a Peltier device: a stable water flow rate is used to dissipate the generated heat guaranteeing a CCD standard temperature around -3°C during operation in order improve the signal to noise ratio (S/N) of the acquired images and to prevent serious damage to the CCD camera.

All the significant parameters of the detector are summarized in the table below.

Pixel resolution	4008×2670 (3:2 aspect ratio)
Input Pixel Size	12.5 μm^2
Input diagonal	~ 60 mm
Input active area	~ 50×33 mm
Scintillator	GADOX doped with terbium
Light exclusion	10 μm Al foil
Cooling	Water cooled
Readout Speed	20 MHz pixel rate
Saturation	~ 50˙000 e^- at minimum gain, 12 bit mode
Gain	~ 800˙000 e^- at minimum gain, 16 bit mode
On-chip binning	User selectable 1×1 to 8×8
Exposure time	User selectable from 10 ms to 30 min

Table 2.2 - ***Technical characteristics of the Photonic Science FDI VHR Camera.***

2.1.3 The other components

Once the sample is placed on the centre of the turn-table for scanning, it can be moved both in the horizontal direction (i.e. along the x axis orthogonal to the guide rail) and in the vertical one, in order to accurately fit the FOV of the CCD according to the selected geometrical magnification. To provide those movements two linear translation stages by Physik Instrumente are combined in a stack below the turn-table.

A brief description of the motors characteristics will follow. The horizontal stage is furnished with an integrated stepper motor controller: it has a large travel range of 204 mm, a minimum incremental motion[2] of 0.1 μm and maximum velocity of 20 mm/sec.

[2] The *minimum incremental motion*, sometimes referred to as the operational resolution, represents the motion that can be repetitively executed. This concept is different from the *design resolution* (i.e. the theoretical minimum movement that can be done, purely calculated on the basis of the drive components):

Such a device guarantees high-accuracy, which can be considered as the maximum tolerable difference between the ideal position and the actual one, and high-repeatability. A position reference sensor is also located approximately in the middle of the operating range which can be used to reference the absolute position of the stage.

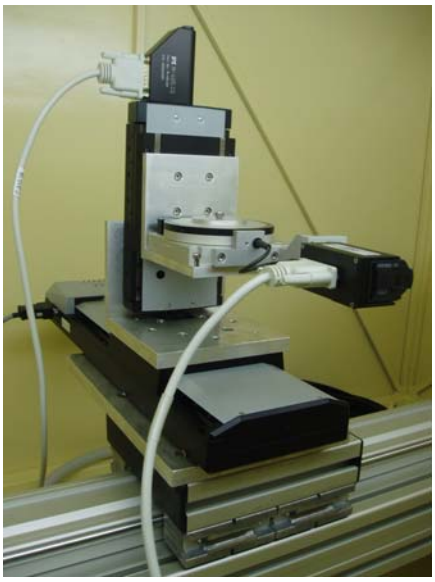

Figure 2.6 – The two translational motorized stages and the turn-table to mount the sample.

The vertical movement is controlled by another translational stage with a travel range of 50 mm providing 0.1 μm of minimum incremental motion and maximum velocity of 1 mm/sec. The stage utilizes a closed-loop DC motor, equipped with position encoders and limit switches.

The rotational stage has a minimum incremental motion of 3.5 μrad and a maximum velocity of 6 degrees/sec. It has a diameter of 100 mm and is equipped with a closed-loop DC motor with worm gear drives allowing unlimited rotation in either the directions without backlash. The user can deduce coarse angular position from a graduated ring placed on the outer edge of the turntable. A position reference sensor is also foreseen to reveal the absolute position.

The rotational and the vertical motors are externally directed by two daisy-chained motor controllers for the simultaneous control of the rotational and vertical movements.

---

generally, the minimum incremental motion may be significantly less than the design resolution. Instead in our case the two quantities coincide.

Position, velocity and other motion parameters can be changed on-the-fly by setting high-level commands via specific macros.

In order to assure the detector plane to be orthogonal to the incoming cone-beam, it is necessary to regulate the tilt angles of the CCD camera, in particular the pitch and roll movements. Thus, under the CCD camera a manual high precision tilt with decoupled and orthogonal axial motion is placed, providing a mean for levelling and tilting the camera over a ±10° range. The mechanism exhibits a reduced creep or backlash and a good repeatability.

After this preliminary descriptive part which led us to the assembling of the TOMOLAB facility through the description of its key features, let's enter now deeper inside into the core of the dissertation. To characterize the performances of the machine we spent a commissioning period conducting several tests in order to exploit its potentialities. The first step consisted in providing the software tools necessary to assure an effective communication between the components as well as an efficient management of the whole facility.

2.2 Controlling the TOMOLAB

During a tomographic scan as well as during the pre-processing operations of sample alignment and parameters optimization, the shielded cabinet should be obviously closed, thus a visual inspection of inside is prohibited. To help the user aligning the sample, and to visually control its position, a webcam is placed inside the cabinet (see Figure 2.7).

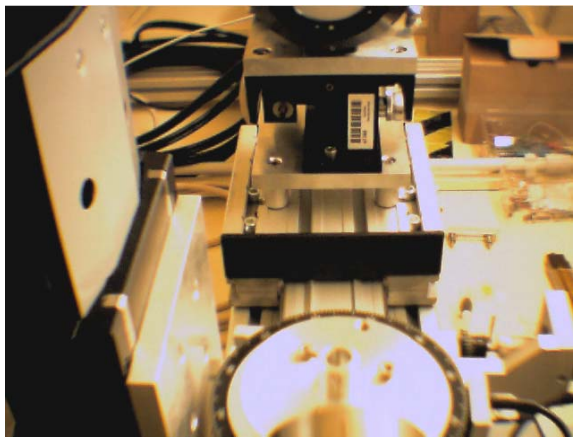

Figure 2.7 – A typical view from the webcam located inside the TOMOLAB.

The X-ray source, the motors for sample positioning and the CCD camera can be independently controlled via dedicated programs. The X-ray tube communicates via serial port with the control unit PC (see Figure 2.8). Similarly, all the motors for the sample positioning can be remotely controlled via serial ports, setting the motor speed as well as the desired movement given in relative coordinates with respect to the *Home Position* of each stage. The actual position of each motor can be checked and, in case of errors or troubleshooting in the experimental set-up, any movement can be immediately stopped.

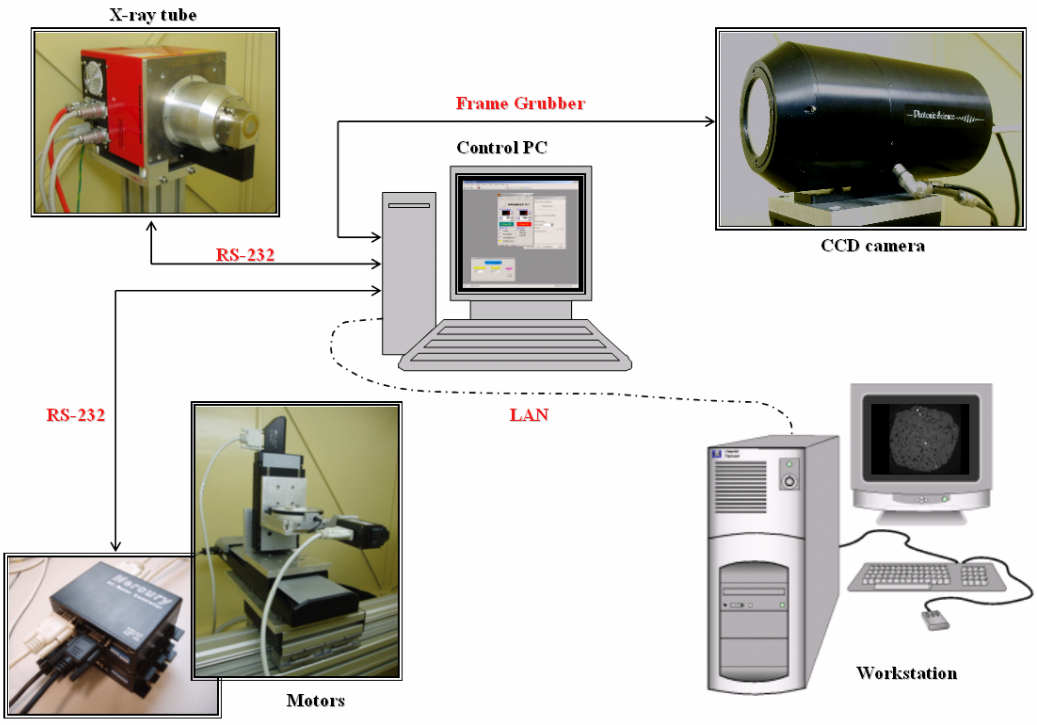

Figure 2.8 – The controlling scheme for the TOMOLAB station.

The CCD camera is controlled by the commercial *Image-Pro Plus* program, both for the acquisition of single planar images and to lunch a tomographic scan, when synchronization with the rotational motor is required. Several parameters need to be set according to the specific experimental activity which has to be carried on. Most of them concern the CCD camera available options. Among these it's worth mentioning the binning[3] and the exposure time. A good compromise between resolution, speed and

[3] The binning involves the possibility to sum together the signal collected from two or more adjacent pixels. This operation of course affects the nominal pixel size, for example doubling it when using the

handling of the acquired data is achieved working at binning 2×2 (i.e. with an effective pixel size of 25 μm). The exposure time of each planar radiograph should be determined maximizing the number of counts of the CCD camera. Any condition of pixels saturation (local or diffuse) is deleterious and should be always avoided: with the CCD operating at 12 bit saturation will occur at 4095 counts (around 64.000 if 16 bit mode is activated). Finally, the choice of the proper region of interest (ROI) on the CCD camera depends on the lateral sample size and on the optimal centring of the rotation axis.

In addition to the photo-generated charge, the CCD normally collects charges that are due to various forms of non-ideal leakage and thermal activation: these effects represent the so called *dark current*. Usually, the dark current increases linearly with the integration time. Another non-ideal behavior is the non-uniformity of response of the CCD pixels: usually the electric charges that can be read from the different pixels, although under the same illumination condition, may be not the same. Thus, all the images acquired by the CCD camera require a normalization procedure before using. The dark current effect is reduced acquiring a dark field image (i.e. an image with the X-ray source off containing the electron noise of the CCD camera). Instead, the effect of the non-uniformity can be corrected by acquiring a flat field image (i.e. an image without the sample). The normalization procedure of the original image I_{Raw}, usually applied off-line before the slices reconstruction, is finally carried out according the following formula:

$$I_{Norm} = \frac{I_{Raw} - I_{Dark}}{I_{Flat} - I_{Dark}} \qquad [2.2]$$

where I_{Flat} and I_{Dark} the flat and dark field images respectively and I_{Norm} is the correct normalized image to use for the reconstruction process. As an example in Figure 2.9 the normalization procedure is illustrated for a titanium screw implanted into a medullar bone. One can clearly notice on the background of the original raw image the honeycomb structure due to the fiber optical taper, which completely disappears after the normalization.

---

option *binning 2x2*. Binning can also couple asymmetrically the pixels in the vertical or horizontal direction.

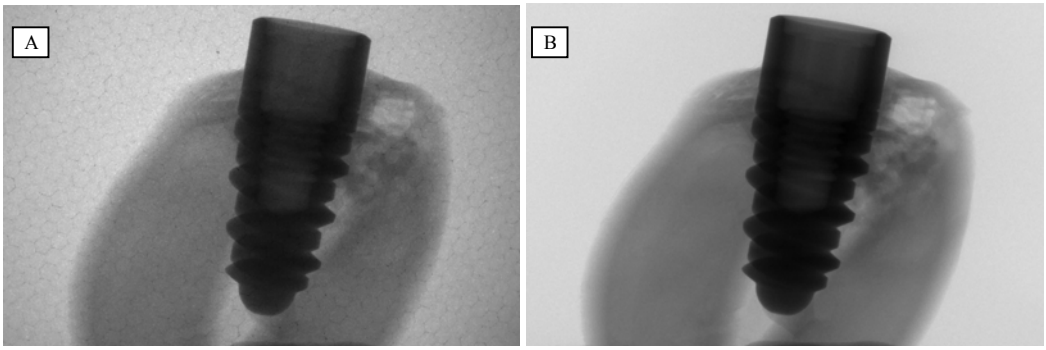

Figure 2.9 – The normalization procedure illustrated for a titanium screw implanted into a medullar bone: the original raw image (A) and the final result after normalization (B). Acquisition parameters: 80 kV, 200 μA, M = 4×, bin2×2.

Once the tomographic scan is completed and all the projections are transferred to the workstation, the slices reconstruction process starts. Commercial software *Cobra Exxim* is employed (www.exxim-cc.com). Calculations assume the object as placed in a rotating coordinate system (the scan geometry was reported in Figure 1.3), the source at a radius D_{so} in the mid-plane, the central ray running from the source through the origin to the detector which is perpendicular to the central ray at distance D_{sd} from the source.

2.3 Preliminary tests

2.3.1 The components arrangement

The mechanical components, the X-ray tube and the detector platform were arranged inside the TOMOLAB cabinet with maximum care to the precise manual alignment later refined by mean of a laser level. Motors were assembled and tested outside the cabinet and finally mounted on the sliding platform on a customized Bosch guide, (see Figure 2.10).

We developed custom remote control system in LabWindows/CVI, which is an ANSI C integrated development environment. A fundamental aspect to consider when carrying on tomographic scans is the perfect synchronization of the detector acquisition and the rotational movements of the sample: the object in fact is supposed to be stable during the whole scan and particularly motionless during the image acquisition, which sometimes can take several seconds. Once all the devices were installed and aligned, several preliminary tests were performed.

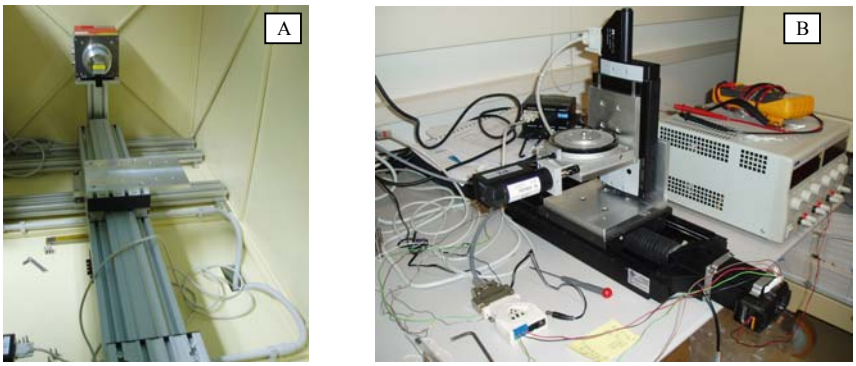

Figure 2.10 – The X-ray source mounted inside the cabinet (A) while preliminary test are carried out on the assembled motors (B).

During this preliminary test, an external trigger signal was sent to the CCD and the rotational motor to separately control their synchronization by a custom developed program.

2.3.2 A comparison of planar images

The first images colleted by the CCD camera consist of planar images of simple real objects spanning the basic material categories typically investigated at the tomographic station.

One should keep in mind that the TOMOLAB station, as it is intended to be complementary to the SYRMEP beamline particularly in terms of the delivered energies, was specifically designed to deal with heavy materials exhibiting high X-ray absorption. However, we verified that the implemented configuration of the facility is suitable enough for the imaging of light material too, exhibiting absolutely high quality results also at the lower energies. Another aspect that we like to confirm is possibility to work by the phase contrast imaging mode, which is theoretically possible thanks to the coherent source provided by the small focal spot size, as discussed in the first chapter.

In Figure 2.11 some practical examples are showed concerning different types of samples, starting with the high absorbing sandstone rock, then a wood sample and finally the light polyurethane foam. A rough and qualitative comparison with the same images obtained at the SYRMEP beamline by synchrotron light is also presented.

The polystyrene sample represents a very interesting and crucial test as it is typically considered a pure phase object. In recent years the potential of inline phase contrast imaging using laboratory sources has been exploited, demonstrating that phase-contrast images can be produced also by polychromatic micro-focus x-ray sources (Wilkins,

1996). This enables also weakly absorbing or non-absorbing samples, as the polystyrene showed here, to be successfully imaged by revealing their thin microstructures.

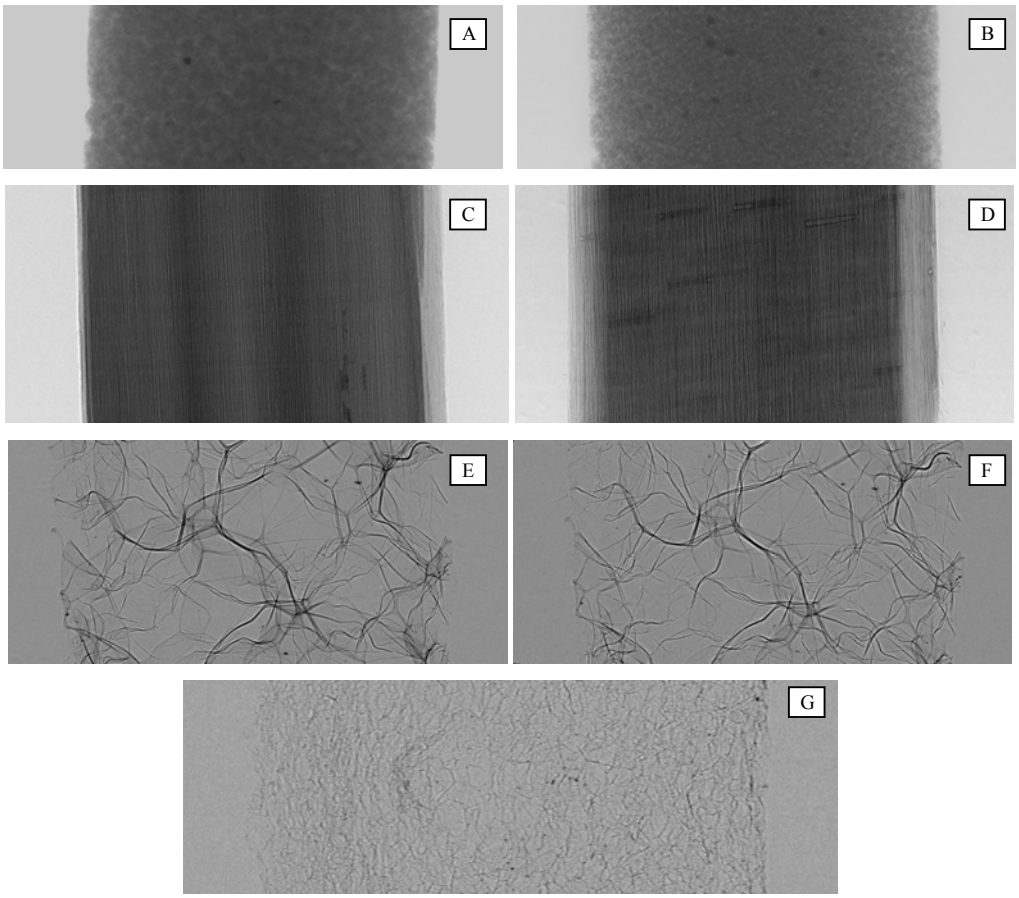

Figure 2.11 – Comparison between images of different materials. (A) sandstone rock at TOMOLAB (70 kV, 200 μA, pixel size = 5 μm, D_{od} = 40 cm) and (B) at SYRMEP (20 keV, pixel size = 3,85 μm, D_{od} = 10 cm); (C) spruce wood at TOMOLAB (50 kV, 200 μA, pixel size = 3,57 μm, D_{od} = 60 cm) and (D) at SYRMEP (13 keV, pixel size = 3,85 μm, D_{od} = 4 cm); (E) polyurethane foam at TOMOLAB (40 kV, 200 μA, pixel size = 4,16 μm, D_{od} = 50 cm) and (F) at SYRMEP (12 keV, pixel size = 3,85 μm, D_{od} = 30 cm); (G) polystyrene sample at TOMOLAB (40 kV, 200 μA, pixel size = 4,16 μm, D_{od} = 50 cm).

The phase contrast depends on the object-to-detector distance: just increasing D_{od} up to 75 cm, as illustrated in Figure 2.12 using an electric connector as a test-object made of a plastic cladding with void in its inner part, phase contrast fringes can be revealed at the border constituted by the interfaces of two low density materials (e.g. in the case of Figure 2.12, the double interfaces due to the air-to-plastic and the plastic-to-air passages).

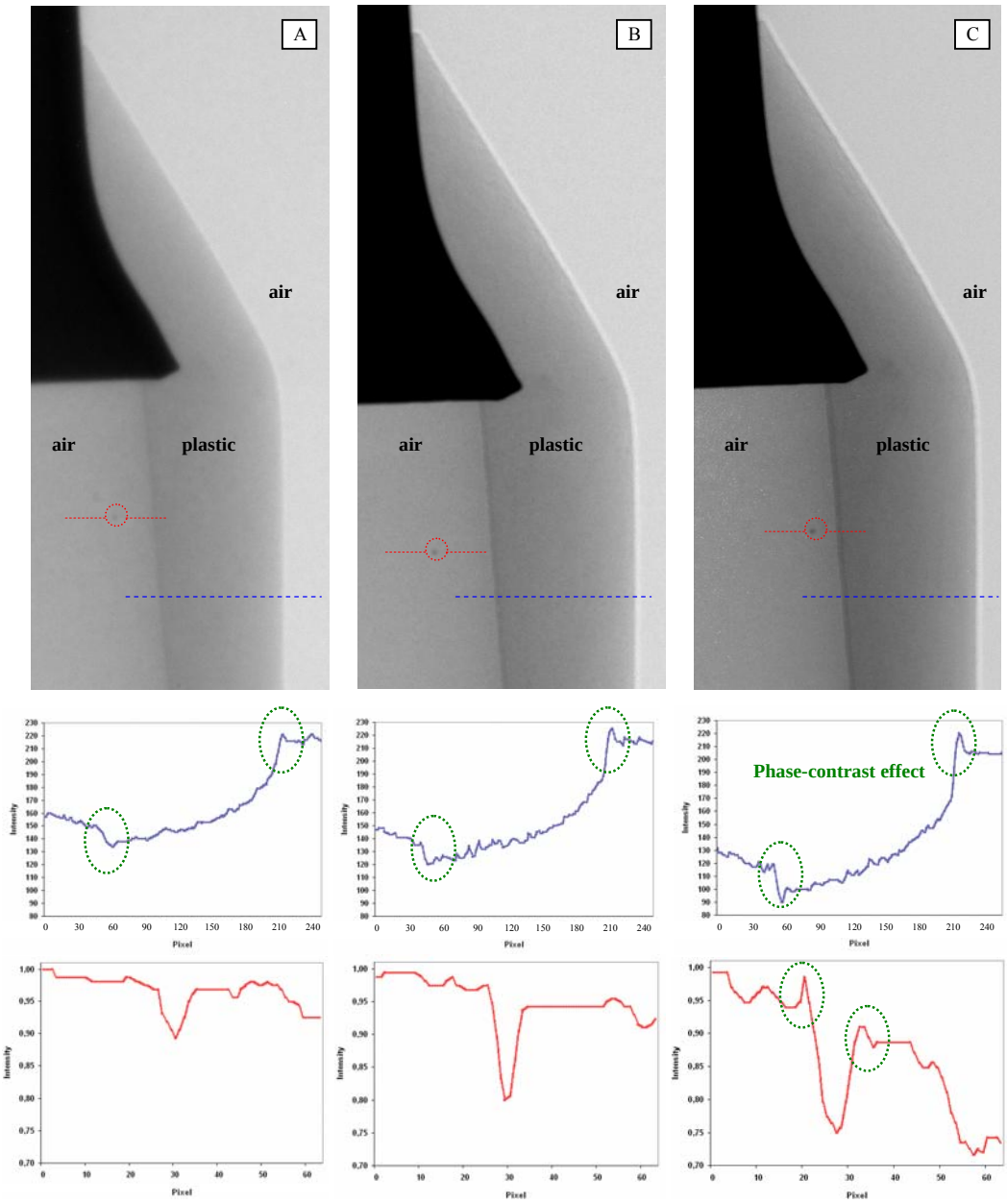

Figure 2.12 – The phase contrast effect as a function of the object-to-detector D_{od} distance in an electrical connector. The source-to-object distance D_{so} is kept constant at 10 cm. The phase contrast fringes become more visible at the air/plastic interfaces (blue profiles) as D_{od} increase; the contrast of a small defect in the plastic is also enhanced increasing D_{od} from 10 cm (A) to 50 cm (B) and 75 cm (C), as showed by the red line profiles. The axis values are scaled.

Moving back the CCD camera, thus increasing D_{od}, the phase contrast effect produces an edge enhancing which is noticeable in the perturbations highlighted in the lower profiles. Furthermore, also a small defect in the plastic part of the electrical connector is better revealed (see the defect borders on the reported linear profiles): in

this case, however, also the increased magnification factor, which increases the spatial resolution, plays a role on the improved visibility.

Other planar radiographs of real objects showed in Figure 2.13 can better illustrate the phase-contrast effect obtainable at the TOMOLAB facility. Due to the low absorptive properties of biological samples as the butterfly or the leaf showed here, they seem invisible by pure-absorption radiography as the X-ray attenuation is too poor. Instead, recording on the detector plane also the phase shifts introduced by the sample on the X-rays which experienced different paths through the object, a lot of details can revealed the presence of the object by mean of the edge enhancing effect. For instance, the thin line of the butterfly wings is visible as well as the secondary vessels of the leaf structure.

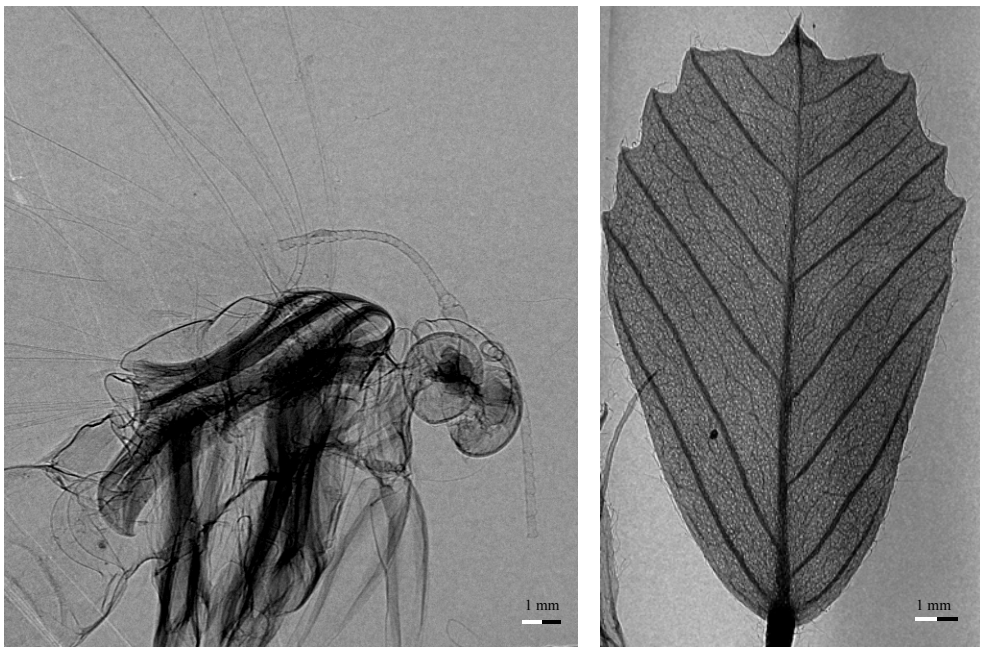

Figure 2.13 – The phase effect noticeable in the images enhances the contrast of thin and light particulars of a butterfly (A) and a leaf (B). Acquisition conditions: 40 kV, 200 μA, pixel size = 6.25 μm , D_{od} = 30 cm)

Conclusion

In this chapter the main components of the TOMOLAB facility have been examined in details. It's worth stressing once more how the scrupulous combination of the single devices makes the whole instrument powerful: the right choice of the X-ray source, coupled with the particular detector, the proper mounting of the positioning system as

well as, least but not the last, the cabinet design, should match all together to assure the best performances of the μ-CT station.

Furthermore, for a custom facility like TOMOLAB we gave an idea of the difficulties that one meet for the precise control, the coordination and the accurate synchronization of the equipments. All these requirements in fact have to be satisfied in order to produce good images.

To whom it concerns the image quality, we qualitatively demonstrate, through several preliminary tests, that our expectations are roughly fulfilled.

However the acquired and reconstructed images are far away to be artefacts-free. A rigorous characterisation of the machine is needed in order to fully exploit its capabilities; on the other hand, a comprehension of the causes responsible for the image degradation is useful to optimize the acquisition and reconstruction processes. The third chapter of the dissertation will lead us deeper inside into these topics.

Chapter 3

Characterisation of the facility

In this chapter we will provide a characterization of the TOMOLAB imaging system on the basis of the real spatial resolution of the images related to mathematical parameters such as the point spread function (PSF) and the modulation transfer function (MTF), evaluated both on acquired radiographs and on the reconstructed slices.

The final image quality of the reconstructed slices is degraded by different kind of artefacts caused by the intrinsic limitations of the digital acquisition, the peculiar characteristics of the emitting tube and the collecting detector as well as the geometrical uncertainness associated with the system which influences many of the parameters feed into the subsequent reconstruction process. In this chapter we will define specific procedures to avoid, or at least to reduce, the deleterious effects of the main encountered artefacts like beam hardening, geometrical misalignment and ring artefacts.

3.1 General concepts

One of the key points in order to characterize an imaging system is based on the determination of the spatial resolution which is achievable using that particular machine under different set-up conditions.

The simplest definition of spatial resolution, intuitively related to the resolving power of the human eye, can be done in terms of the smallest spacing between two details that can be clearly imaged. A second definition of resolution can be introduced which is related to the contrast needed to distinguish the object from its background.

To evaluate the final spatial resolution, contributes of single components should be separately considered (i.e. hardware devices like the X-rays source, the CCD camera, its

scintillator layer or other optics as well as software elements like the slices reconstruction process e.g. filtering, interpolation etc.).

The contrast degree appearing in the output images depends not only on the attenuation properties of the chemical components inside the original object, but also on the characteristics of the device used to acquire the images and on the energy spectrum of the incident X-rays.

Another concept that has to be considered is noise, defined as the uncertainty or imprecision with which a signal is registered. The presence of noise, which is intrinsically derived from several processes occurring all through the tomographic measurement (e.g. the X-ray generation, the scattering phenomena originated inside the investigated object, the electronics of the detector), definitely deteriorates both the spatial resolution and the contrast resolution that is ideally achievable. To improve the signal to noise ratio (S/N), in order to emphasize the signal variations due to the real object features respect to those ones due to stochastic noise, one should increase the photons counting registered onto the detector plane. This can be done just reinforcing the flux or rising up the exposure time. Both the solutions include their drawback, as the first one will tend to enlarge the focal spot size thus inducing additional blurring to the acquired images, while the last one will exalt also the beam instabilities and, if the long exposure time is routinely adopted, will reveal to be a quite expensive solution as it will also shorten the life expectance of the components.

The need of acquiring a signal which is strong enough compared with the background noise practically imposes some restrictions to the maximum size of the investigated objects: if the object is too thick, the incident beam is highly attenuated, thus just few photons reach the detector and low-quality images are produced.

These descriptors, here intuitively explained, of resolution, contrast and noise seem deeply linked to each other and need the introduction of some intermediate concepts to clarify such connections. Considering a point-like object of a diameter d, ideally, one would expect to perfectly reproduce a circular shape of the same diameter d on the image plane. Instead, according to the real experience, the acquired image will be always affected by a certain amount of blurring which is introduced by the imaging system. In the spatial domain, this distortion can be quantified in terms of the point spread function PSF of the imaged object (see Figure 3.1). Thus, we could assume that two close details in the image can be separated by the particular imaging system if they lie at a distance larger than the full width at half maximum (FWHM) of the measured

PSF. In other words, for a given imaging system (whose characteristics are a-priori unknown) the PSF can be viewed as the system response to a spike unitary input.

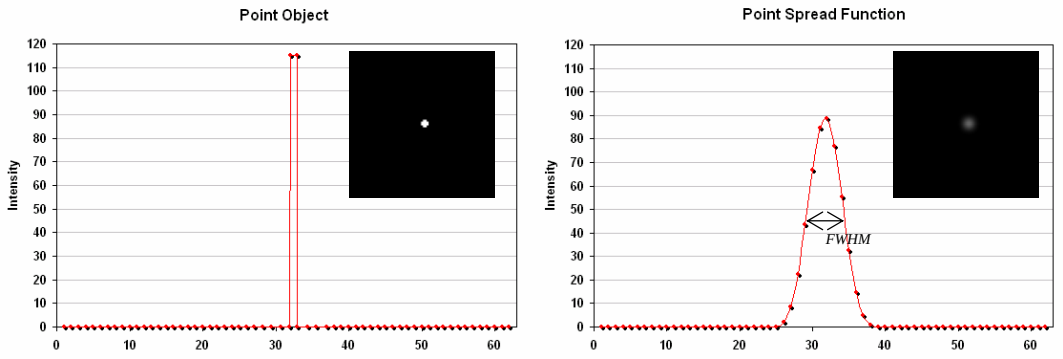

Figure 3.1 – The spike produced by a point like object and its PSF as the result of the acquisition process (simulated data). The full width at half maximum of the PSF is also indicated.

Thus one can consider the output image as the convolution of the original object with the system PSF. Similarly, in the frequency domain, the MTF, which is related to the magnitude of the Fourier Transform of the PSF, describes the contrast level which is preserved by an imaging system as a function of the spatial frequency content of the original object.

In the next paragraphs, the concepts here introduced will be practically applied to estimate the potentialities of the instrumental components assembled into the TOMOLAB facility.

3.2 The different contributions to the achieved spatial resolution

In 3D, the nominal spatial resolution is associated with the voxel size of the digital reconstructed object. Thus the resolution along the z axis (i.e. the slice thickness) is also roughly determined by the detector pixel size. This usually implies that the spatial resolution is the same for the three directions, even if, in principle, this should be verified case by case due to directional dependency that can be introduced by the detector design or the reconstruction process (i.e. the PSF could be asymmetrical).

Furthermore, during the tomographic acquisition, a sufficient number of projections should be taken at regular angular steps to guarantee a complete sampling of the object up to the highest frequency that one desire to identify: a semi-empiric rule set the minimum number of views, for a tomographic scan of 180°, by the following formula:

$$N_{proj} = \frac{N_x \pi}{2} \qquad [3.1]$$

where N_x stands for the image width on the detector plane measured in pixels.

Through the above formula the number of projections is implicitly set to the same as the number of rays per projection when a parallel X-rays beam is considered (Kak, 2001). If angular or planar undersampling occurs then the so called aliasing distortions usually affect the reconstructed images appearing as thin white or dark streaks, which are particularly evident close to the object corners.

Dealing with tabletop cone-beam facilities as TOMOLAB several parameters can be listed affecting the image quality and spatial resolution. Most of them can be considered strictly machine-dependent (Coenen, 2004), as for example the geometrical magnification, the focal spot size, the pixel size of the CCD, the X-ray energy and spectrum, the geometrical alignment with respect to the rotation centre, the mechanical precision and accuracy of the rotating table and so on. When considering the reconstruction process of the slices, one introduces a lot of additional factors that influence the final results, whose identification and relationships are usually of difficult comprehension.

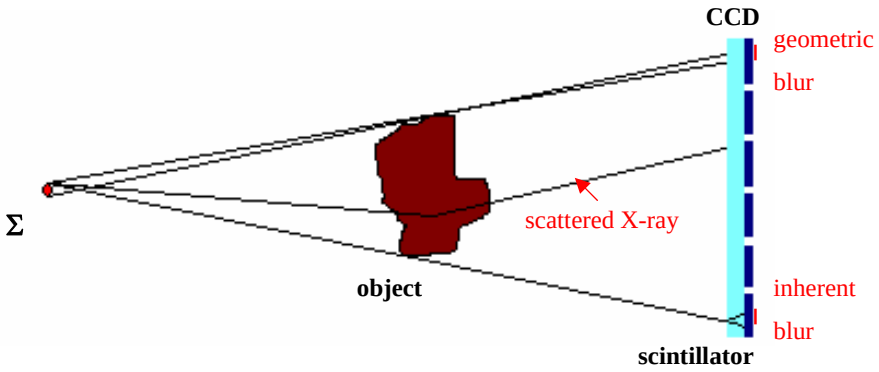

Figure 3.2 – Scheme of the cone-beam geometry and the main related blur causes.

The first observation concerns the finite spot size: X-rays emanated from opposite sides of the source track different paths through the investigated object, although travelling towards the same detector element. As a consequence, on the detector plane a blurred attenuation profile occurs (see Figure 3.2).

Additionally X-rays scatter, whose relative amount depends to the selected energy and to the object characteristics, generally causes a background noise that should be later removed or mitigated.

Actually, the focal spot size of the X-rays source and the pixel size of the detector combine together their effect to establish the final spatial resolution of the images: the blurring due to the pixel spacing and the X-ray source focal spot size are independent

functions. As a general rule, in fact, when acquiring high resolution data at relatively higher magnification the size and shape of the X-rays source seems to affect the image resolution and appearance, while at lower magnifications the resolution is limited by the pixel size of the detector (see Figure 3.3).

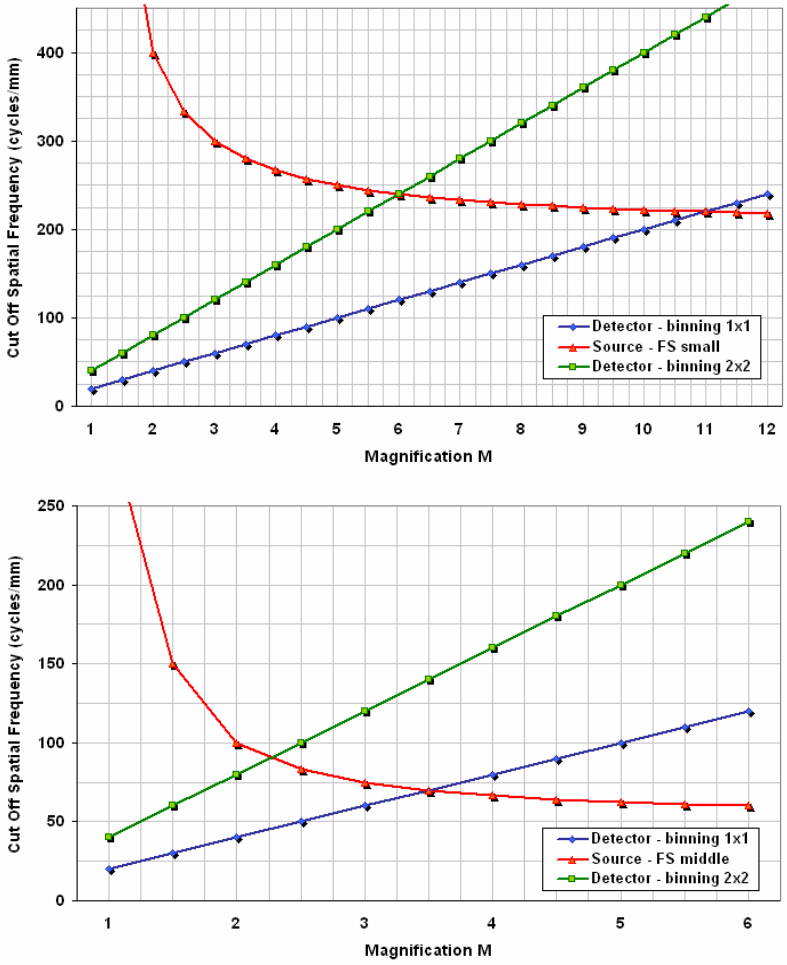

Figure 3.3 – The combination of source-related and detector-related spatial resolution as a function of the magnification factor as well as of the focal spot mode and the pixel binning. The optimum match of the two components is achieved at the intersection point of the two curves.

One can assume that the X-ray source is responsible for the so-called geometrical unsharpness U_g (i.e. the blur effect due to the finite focal spot size as above illustrated) and for the instability both for drifts in the source flux and in the focal spot position. The geometric unsharpness is described by the following relation:

$$U_g = \Sigma \cdot (M - 1) \qquad [3.2]$$

where M is the magnification factor adopted and Σ is the focal spot size.

The source instability is particularly appreciable for long-term operation, when the focused electron beam is capable to erode or melt the anode (Grider et al., 1986). The overall quality of the produced images depends largely on reliable and consistent positioning of the focal spot: vice versa the movement of the focal spot introduces an imprecision that, altering the scan geometry, can significantly interfere with the reconstruction process as it assumes a fixed position during the scan.

Various factors related to the construction or operation of the X-ray apparatus (including among the others, for example, vibration caused by moving parts or thermally induced effects as a result of high operating temperatures or thermal gradients) often compromise the quality of the reconstructed images.

Particularly, physical changes that occur in the X-ray device components due to high operating temperatures impose significant mechanical stress and strain on the X-ray source, causing the components to deform, either plastically or elastically. Particular care should be taken concerning the effects of the elastic deformation of the X-ray source components on the focal spot location and positioning.

Until here, the contribution of the X-ray source was highlighted. On the other side, the detector should be considered. It is in fact responsible for the so-called inherent unsharpness U_i basically due to the scattering occurring inside the scintillator screen, to the electronic noise and to the detection efficiency of the light conversion into electrons. Increasing the thickness of the fluorescent screen improves its efficiency as it will absorb a greater amount of the incident photons, but at the same time decreases the overall spatial resolution because it introduces a higher scattering effect of the visible light inside the fluorescent layer itself.

The measurements and combination of the different causes of unsharpness has been studied since the beginning of non-destructive testing (Klasens et al., 1946).

The above discussed observations should drive the design of the single components, whose combinations should provide the best flexibility and image quality for the specific purposes.

3.3 The MTF measurements

Both the previous introduced concepts of PSF and MTF may be used as performance measures applicable to the single device alone or to the whole acquisition chain (i.e. including the X-ray source) responsible for the achievable spatial resolution. However, in the general case, the determination of the unsharpness function (1D or 2D) is a quite

hard task. Heavy mathematical tools are required to establish the unsharpness as 2D convolution (Dougherty and Kawaf, 2001) or Monte Carlo simulations (del Risco Norrild et al., 2001).

Assuming the whole acquisition chain to be a black box whose input signal is the original object and the output one is its reconstructed image, the unsharpness function represents the impulse response of the system. This can be ideally considered as a point like object, or a small hole inside an attenuating planar phantom. However, this is practically difficult to realize, so that the unsharpness function is usually recovered via simple derivation of an edge signal. Because an edge response is much easier to collect, a widespread practical method adopted to evaluate the performances of an imaging instrument chain bases on the extraction of an oriented edge profile (i.e. the so called edge spread function - ESF) along the intensity gradient of a sharp test object border.

3.3.1 Planar radiographs

To evaluate the spatial resolution (together with the image contrast) of the planar radiographs acquired by the detector, a simple approach can be followed, just placing a sharp rectangular attenuating profile on a transparent background. The ESF can be calculated from an intensity profile through the edge of the contour. The line spread function (LSF), in analogy with the PSF, can be then obtained as the first derivative of the collected ESF:

$$LSF(x) = \frac{d\,ESF(x)}{d\,x} \qquad [3.3]$$

Finally, the Fourier Transform of the LSF can be used to get the MTF:

$$MTF(\nu) = \left| \int_{-\infty}^{+\infty} \left(\frac{d\,ESF(x)}{dx} \right) e^{-2\pi i \nu x} dx \right| \qquad [3.4]$$

The spatial resolution r can be estimated as the highest spatial frequency $(1/r)$ that can be revealed, usually expressed as line-pairs per millimetre.

Tests patterns composed of a regular spaced bar grid made of lead which is commonly refer to as the Funk phantom (see Figure 3.4) are also used to evaluate the achievable spatial resolution.

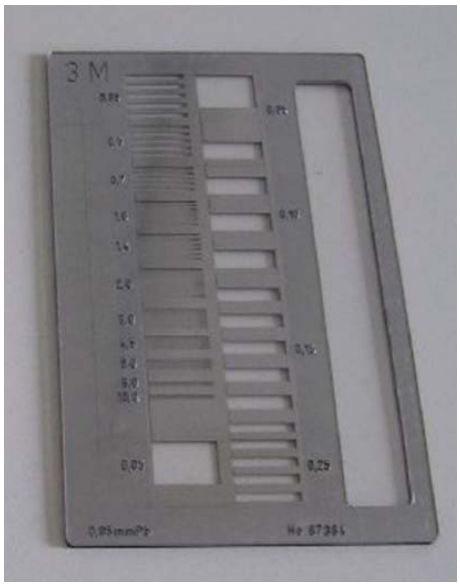

Figure 3.4 – The bar pattern (Funk phantom) used to evaluate the overall MTF of the facility.

The image of a sharp edge-object was used to collect the ESF (see Figure 3.5): several profiles were tracked orthogonally to the edge, and averaged to increase the statistic while reducing the random noise fluctuations. Measures were repeated for different conditions: detector binning 1×1 and 2×2 (which are the most adopted for scanning), tube voltage of 40 kV and 80 kV, and magnification distances of 2×, 4×, 6×, 8×, 10×, 12×, obtained via multiple images acquired with a fixed source-to-object distance of 10 cm, and an object-to-detector distance varying from 10 up to 110 cm, regularly stepped every 20 cm.

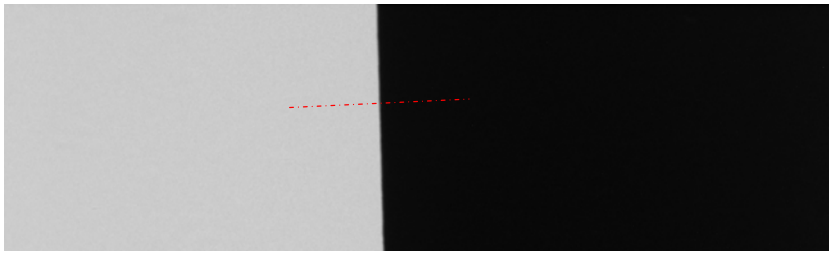

Figure 3.5 – The edge object test used to evaluate the ESF: binning 2x2, M = 6×, energy = 40 kV.

To fit the ESF, the following Sigmoid function can be used:

$$S(x) = \frac{a}{1 + e^{-\frac{x-b}{c}}} \qquad [3.5]$$

The LSF is calculated as the first derivative of the ESF, as illustrated in equation [3.3]. Adopting a more rigorous procedure, one can first calculate such a derivative and then fit the LSF by a Gaussian function:

$$G(x) = a \cdot e^{-\frac{1}{2}\left(\frac{x-b}{c}\right)^2} \qquad [3.6]$$

The spatial resolution of the whole system can be estimated as the FWHM of the obtained PSF. The described functions are reported in Figure 3.6.

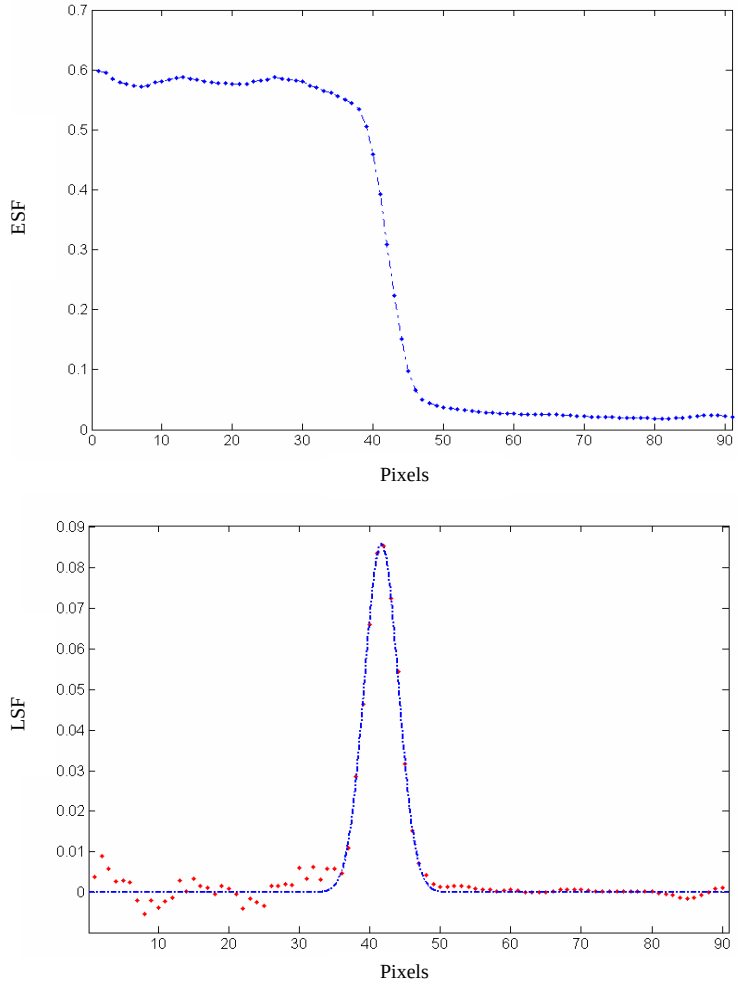

Figure 3.6 – The ESF evaluated as mean value of several cross profiles along the edge (up) and the correspondent Gaussian fit of the obtained PSF (bottom).

Figure 3.7 reports the resulting curves for different experimental conditions that we tested. The calculated spatial resolution is reported as a function of the magnification factor M, for binning 1×1, 2×2, and for low and high energy (40 kV and 80 kV respectively). As showed the resolution significantly improves until a certain value of M is reached, while after that it remains almost constant. This is basically due to the focal spot size effect which limits the resolution to further enhancement.

As expected, working at binning 1×1 gives better results in terms of the spatial resolution. However, the benefits are not always really important to justify this choice (which looks time consuming from the acquisition point of view as well as computationally expensive from the reconstruction one).

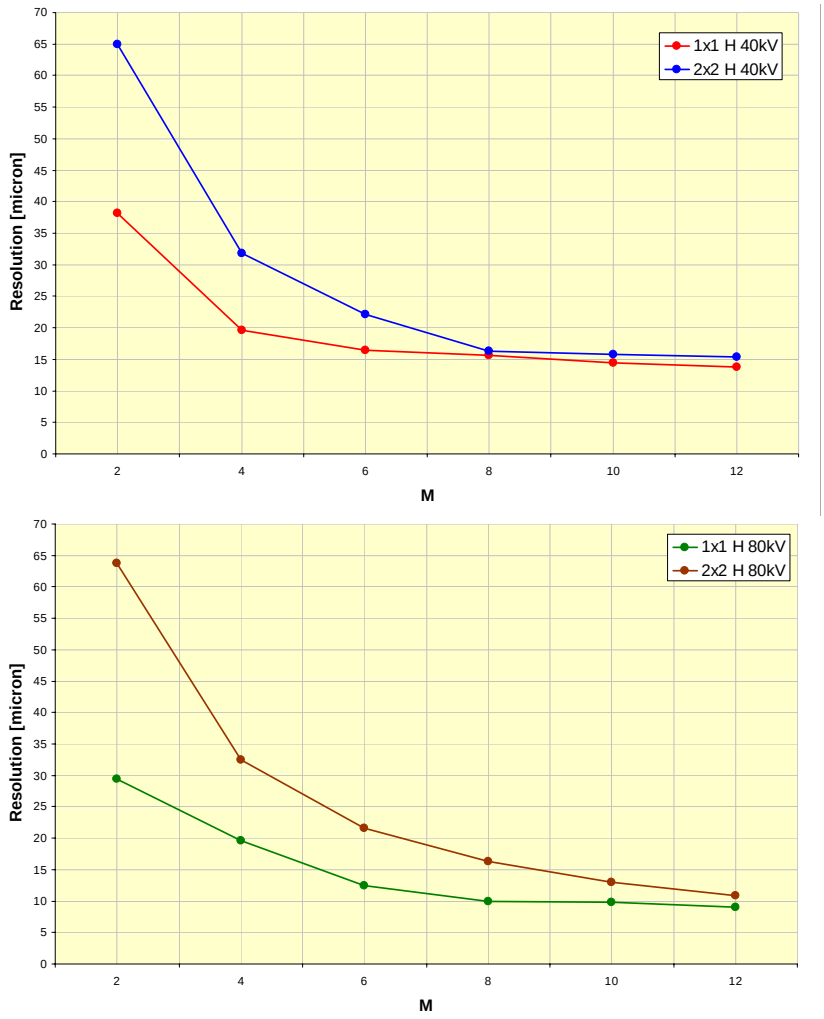

Figure 3.7 – The calculated spatial resolution (FWHM of the PSF) as a function of the magnification factor M, with binning 1×1 / 2×2 and tube voltage of 40 / 80 kV.

3.3.2 Reconstructed slices

Because the final output of μ-CT is a 3D product, which is nothing else than a stack of the 2D reconstructed slices, it is necessary to provide a characterisation of the global resolution deriving from the acquisition step plus the reconstruction process. In this condition we can represent the actual spatial resolution of practical interest for most of

the applications of material science, corresponding to the effective capability to resolve the investigated details achievable with a specific facility.

Thus we applied directly to the reconstructed slices the same method used for the characterisation of the planar radiographs. To do this a circular object has been chosen, as it provides the simplest geometry to reconstruct and because the ESF can be quite easily evaluated by a relatively simple algorithm, as illustrated hereafter.

First, the centre of mass of the cylinder is automatically calculated once the object contour is detected. A radius a bit larger with respect to the disk border is considered to extract the ESF from a set of cross line at the edge of the disk (see Figure 3.8). If the object is perfectly circular and the centre of mass is accurately estimated, the different edge profiles can be exactly overlapped to furnish an averaged and noise reduced cumulative ESF. However, because even very small shifts on the order of one or two pixels can alter the final result, profiles coming from different radii should be usually adjusted to precisely match.

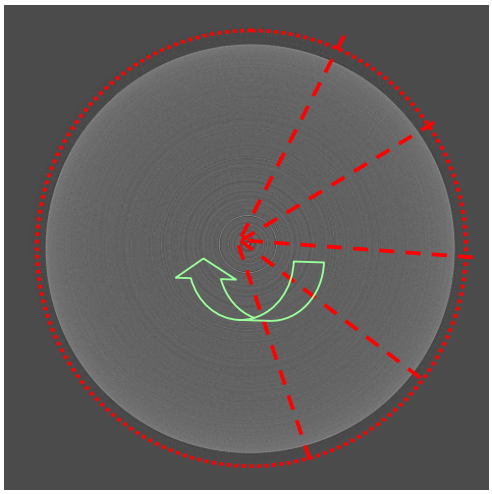

Figure 3.8 – To calculate the ESF, several edge profiles were collected along different radii of the reconstructed disk object.

As mentioned, the final spatial resolution can be also estimated via the MTF of the measured ESF (see [3.4]). We followed this method to evaluate the spatial resolution on the slices. Several parameters affect the achievable spatial resolution: first of all the selected magnification factor M, the binning mode which is set on the detector, the energy used which is related to the object material and the object thickness too and the focal-spot size of the X-ray tube (it can switch from the *small* to the *large* mode). Furthermore, also some artefacts occur which affect the reconstruction procedure of the

slices as we will discuss in the next paragraphs. This complicates the evaluation of the achievable spatial resolution on the slices.

Figure 3.9 shows a comparison between the MTF at two different magnification factors. MTF is plotted as a function of the frequencies for a Plexiglas cylinder, keeping constant the energy (40 kV), the binning mode (1×1) and the focal spot size (small). Usually the MTF value at 10% is taken as the detection limit of the imaging system. Assuming that the spatial resolution r is calculated from the spatial frequency (expressed as line pairs per millimetre) f by the formula:

$$r = \frac{1}{f} \qquad [3.7]$$

we estimate a spatial resolution of about 55 μm and 32 μm at $M = 2$ and $M = 4$ respectively.

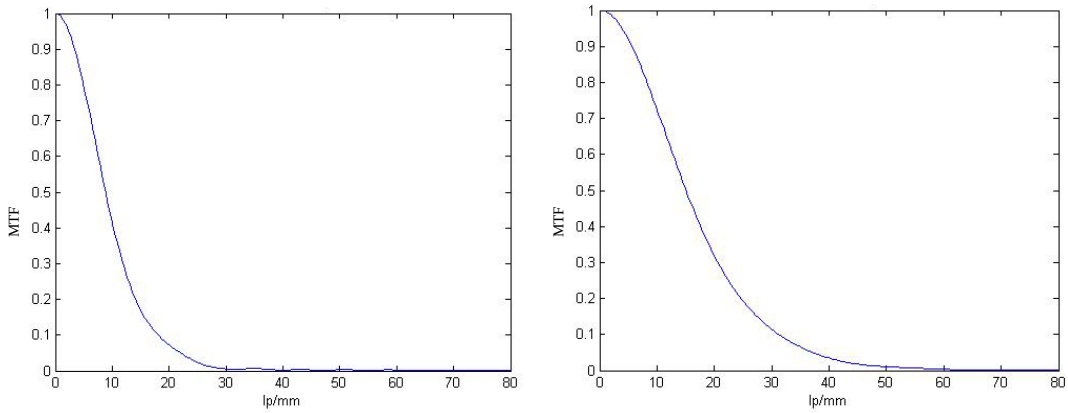

Figure 3.9 – The MTF plotted as a function of the frequencies for a Plexiglas cylinder (bin 1x1, Energy: 40kV, FS: small) at two different magnification factor: M=2 (left) and M=4 (right).

We also compare the effect of the focal spot size: in Figure 3.10 MTF is plotted as a function of the frequencies for the same Plexiglas cylinder, keeping constant the energy (40 kV), the binning mode (1×1) and the magnification factor ($M = 4$). The focal spot size is set to the small and large mode for comparison. Again, the spatial resolution r is calculated by equation [3.7] considering the MTF value at 10% as the detection limit of the imaging system: thus we estimate that spatial resolution changes from about 32 μm to about 38.5 μm for small and large case respectively.

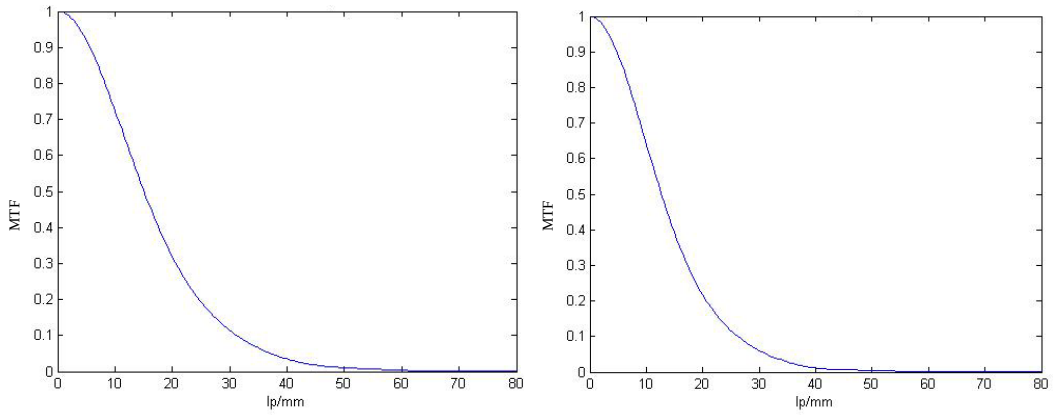

Figure 3.10 – The MTF plotted as a function of the frequencies for a Plexiglas cylinder (M=4; Energy: 40 kV; bin 1x1) at two different focal spot size: FS small (left) and FS large (right).

3.4 Artefacts on the slices

An artefact can be defined as any unphysical feature or any unrealistic distortion that is introduced, systematically or randomly, to the output slices during the acquisition or the reconstruction process.

To separate the contribution of different kind of artefacts is usually a hard task. Furthermore, there are some artefacts which are always present and can never be completely eliminated: the partial volume effect, for example, which rises from voxels containing two or more different phases whose CT number is averaged, the scattering effect which alters the transmitted signal to the detector with X-rays that are deflected from their original trajectory after interactions with matter, or the so called metal artefact which produces streaks around a high absorbing detail.

In the next paragraphs the focus will be directed to those artefacts which are the most important in cone-beam geometry CT, but significantly reducible, in principle, by relatively simple operative procedures or post-processing techniques.

3.4.1 Beam hardening

Maybe the most common and disturbing artefact of μ-CT systems operating by polychromatic X-ray tubes is the so called *beam hardening*. Because the source emits a wide range of energies, the linear attenuation coefficient μ of the Beer-Lambert's law (see Equation 1.7) should be integrated over the entire spectrum. When X-rays pass through the sample, the lower components of the spectrum are absorbed

disproportionately compared to the higher ones (Krimmel et al., 2005): this causes the spectrum become harder and harder since the energy average content is increasing as the X-rays penetrate deeper into the object thickness, while at the same time the overall intensity drops. As a consequence of such a non linear behaviour, the attenuation properties of the sample are no more proportional to its thickness. For this reason it is absolutely difficult to carry out quantitative measurements on slices corrupted by beam hardening.

The typical effect of beam hardening is the artificial brightening of the object exterior parts respect to the central ones, even if the material is perfectly homogenous (i.e. the so called *cupping artefact*, see Figure 3.11). Furthermore, in heterogeneous media, streaks can appear between two dense objects because the beam hardening extent changes form one view angle to another (Barret and Keat, 2004).

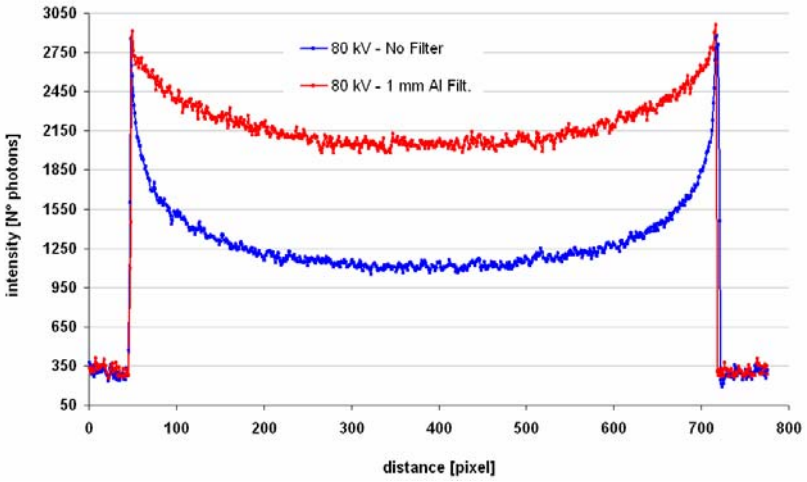

Figure 3.11 – The cupping effect due to beam hardening: the two intensity profiles are measured onto the slice of a homogenous aluminum cylinder.

It's worth noticing that the beam hardening artefact is strictly connected to the operating tube peak-voltage, which is related of course to the optimal energy needed to scan the sample. In other words, working at low energies (i.e. with tube voltages up to 50-60 kV) the beam hardening resulting in the reconstructed slices is generally poor: it means that this artefact doesn't affect so much the low absorbing samples (e.g. polymeric foams, biological samples etc.). On the contrary, at higher energies the effect is considerable (e.g. metallic samples, bones, rocks etc.).

As an example, Figure 3.12 shows the 3D virtual inspection of a damaged metallic sample, which is contaminated by severe beam hardening. Although the beam

hardening effect is much more evident close to the outer border of the sample, the inner part is influenced too. Thus is not possible to by-pass the problem just considering the central part of the sample for further measurements.

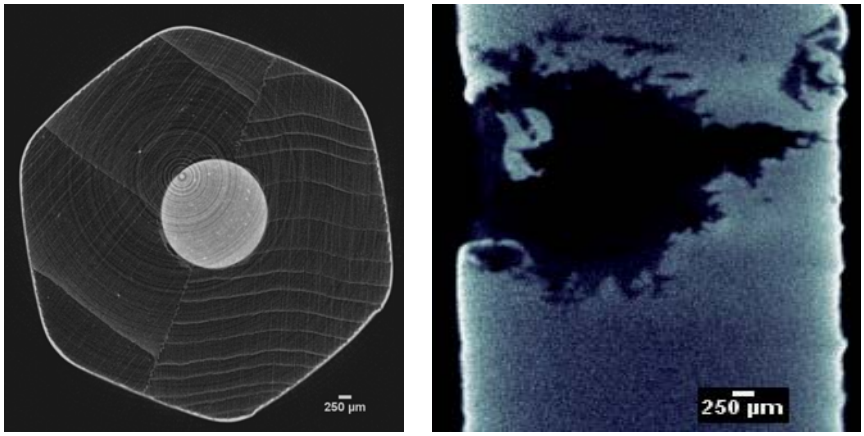

Figure 3.12 – The beam hardening effect is substantially absent when working with low absorptive materials like the wood pencil on the left (tube voltage 50 kVp), but it becomes considerable for high absorptive materials like the steel sample on the right (tube voltage 110 kVp).

Several authors have studied different methods to remove, or at least to reduce, the beam hardening effect, from the simplest to the most sophisticated one.

The first rough and popular method to control the beam hardening consists in placing hardware pre-filter between the source and the sample in order to attenuate the low level components of the emitted spectrum before the X-ray pass through the sample. This way the X-rays beam is kept almost uniform during its travel towards the interior. Typically such a mechanical filter is made of a thin foil of aluminum or copper of different thickness according to the operating conditions of the source.

Other methods aim to eliminate the non linear effect due to the beam hardening. When a radiograph of a wedge-shaped aluminum test object is taken, a non-linear profile is obtained along the direction of the increasing thickness (see Figure 3.13); instead, if a copper plate is placed into the beam, before the object, an almost linear attenuation profile will result, according to the Beer Lambert's law. Properly fitting the non linear curve affected by the beam hardening by a polynomial function a correction can be applied that tends to overlap the two curves. Such a correction could be theoretically applied to all the angular views of a tomographic scan.

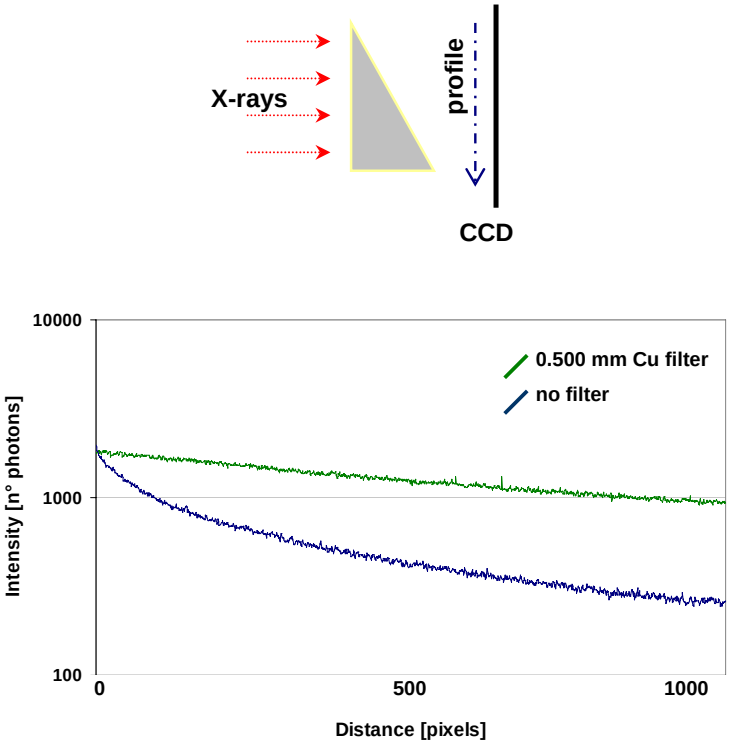

Figure 3.13 – A sketch of the aluminium wedge-shaped object used to evidence the non linear beam hardening artefact (top). Two profiles along the increasing thickness are presented (bottom): the blue one was obtained without any filter, the green one with 0.5 mm Cu filter. Tube voltage was 80 kVp.

Other authors proposed the so called wedge-correction (Rivers, 2005), particularly suited for homogenous materials. It consists of acquiring a tomographic data set of a cylindrical material with similar attenuating properties of the original object, which will be later subtracted from the images collected during the object scan.

Finally, bimodal energy model approach gives an alternative linearization method supported by a strong physical background (Van de Casteele, 2004).

Although the more sophisticated methods, when correctly applied, provide better results in terms of effectiveness, their practical applicability seems quite limited. The main reasons are because samples are rarely homogeneous, because the mathematical and physical background of such methods is generally complicated to be implemented into semi-automatic algorithms and because the global quality of reconstructed images is lowered by the application of any post-processing method.

3.4.2 Geometrical alignment

The achievable spatial resolution of the slices produced by a cone-beam μ-CT system can be dramatically deteriorated also by the geometrical misalignment of the components. In spite of the advanced design, the precise manufacturing of the single instruments and the scrupulous assembling of the whole system, the accuracy which describes all the geometrical parameters is generally inadequate to guarantee a perfect alignment for reconstruction (Smekal et al., 2004). In particular, the mutual positions of the X-ray focal spot, the sample rotation axis and the detector plane are of fundamental importance to optimize the slices reconstruction process.

For a cone-beam scanning geometry, the calculations for the reconstruction process are based on the coordinate systems showed in Figure 1.3 of the first chapter. The object is placed in the (x, y, z) rotating coordinate system. The axis of rotation is the z axis. The central ray runs from the source through the origin at an angle theta measured from the x axis. The detector, placed at distance D_{SD} from the source, has coordinates (u, v): ideally, u is parallel to the xy plane and v is anti-parallel to z. The central ray hits onto the detector plane at the pixel of coordinates (u_0, v_0).The object rotation axis is orthogonally intersected by the central ray of the mid-plane and it is placed at distance D_{SO} on the source side, and at a distance D_{OD} in the detector side.

To regulate the detector plane a manual tilt (pitch-roll) table is mounted under the CCD camera of TOMOLAB which covers, with 0.1 arc-second resolution, a ±10° range decoupled axis motion.

First, it is of fundamental importance to determine the position of the mid-plane. Particularly, the real (u, v) coordinates of the detector plane where the central ray impinges should be identified. With this scope a set of flat filed images is considered, acquired moving back the detector by constant steps along the rail on which it is mounted, while maintaining fixed the tube conditions in terms of voltage, current and focal spot size. An intensity distribution profile was then considered both in the horizontal plane and in the vertical one: assuming that the maximum of the intensity corresponds to the central ray, the statistical analysis of the polynomial fitting of the distribution for each rows and each columns of the detector, furnished the most probable coordinates (u, v) at the intersection of the horizontal and vertical maxima (see Figure 3.14).

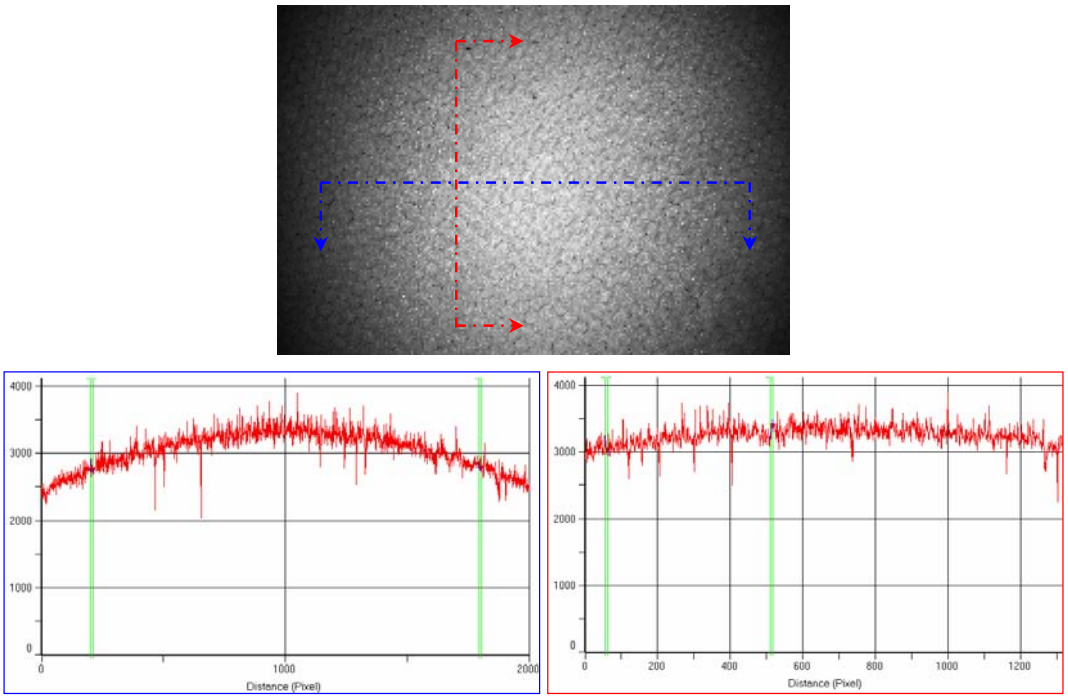

Figure 3.14 – One of the flat field images collected at 40 kVp (top) and two profiles of the i^{th} row (bottom left) and the j^{th} column (bottom right)of the flat image.

Figure 3.15 shows the calculated trajectory of the central ray from the tube focal spot to the detector plane. A vertical gap of around 16 pixels was found in 1 meter of length along the rail.

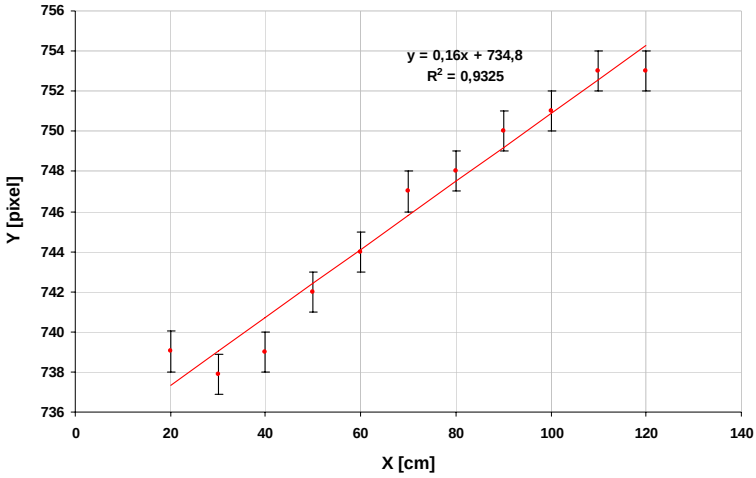

Figure 3.15 – Scheme of the instruments placed inside the TOMOLAB station (top) and the calculated trajectory of the central X-ray along the rail (bottom). Pixel size is 12.5 μm.

Secondly, to guarantee that the rotation axis is aligned with the pixel grid of the CCD camera, a special high precision tip-shaped cylinder was used as a guide-sample. The aim is to verify the alignment of the extreme border of the tip from two images acquired respectively at 0° and 180°. To do this the tip should be place with good precision in the mid-plane of the beam in order to avoid that the vertical magnification effect due to the small variations of D_{SO} and D_{OD} distances confuses the comparison between the two images. On the other hand, the horizontal magnification effect is almost inevitable but it will not influence significantly the comparison. Similarly, to regulate the tilt angle in the orthogonal direction respect to the source-detector line, two images of the extreme border of the tip can be compared, acquired at +10° and -10° with respect to the 0° position.

To verify that the mid-plane is correctly identified a further scan was taken of a Plexiglas cylinder on which a micrometric aluminium mark was inserted. The aluminium mark, when scanned in the mid-plane, should describe a theoretically plane orbit occupying the same row of the projected data. The obtained elliptic orbit showed in Figure 3.16 can be considered as a satisfactorily good approximation of the ideal case, keeping in mind also the limits set by the pixels resolution and the finite dimensions of the observed object.

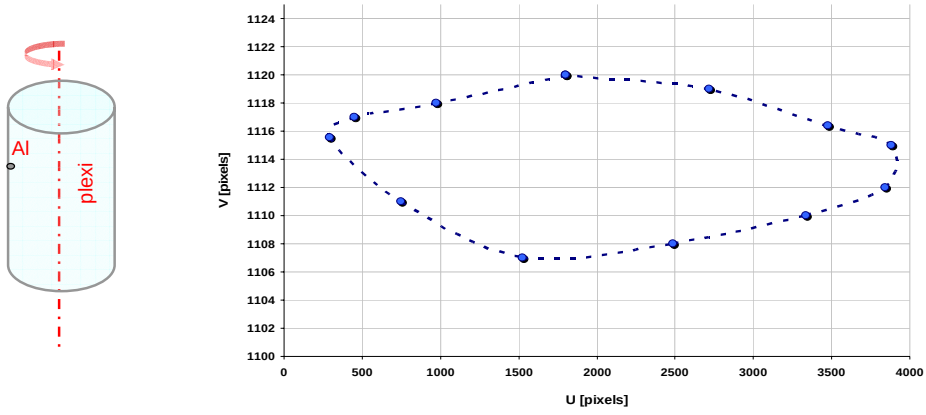

Figure 3.16 – The elliptic trajectory recorded onto the detector plane (u, v) of an aluminum mark glued onto the Plexiglas cylinder during a 360° rotation (pixel size is 12.5 μm).

Finally, the rotation axis should be translated horizontally in order to intersect the central ray. To discover the true position of the rotation axis one can operate on the mid-

plane, where again the vertical effect of the magnification is negletable and the cone-bean can be approximated to fan-beam. The sinogram[1] of the mid-plane slice can be constructed and the center of rotation can be derived. The double contouring effect showed in Figure 3.17 on the reconstructed slices is the typical effect of the horizontal offset, in terms of pixel onto the detector plane, between the rotation axis and the central ray.

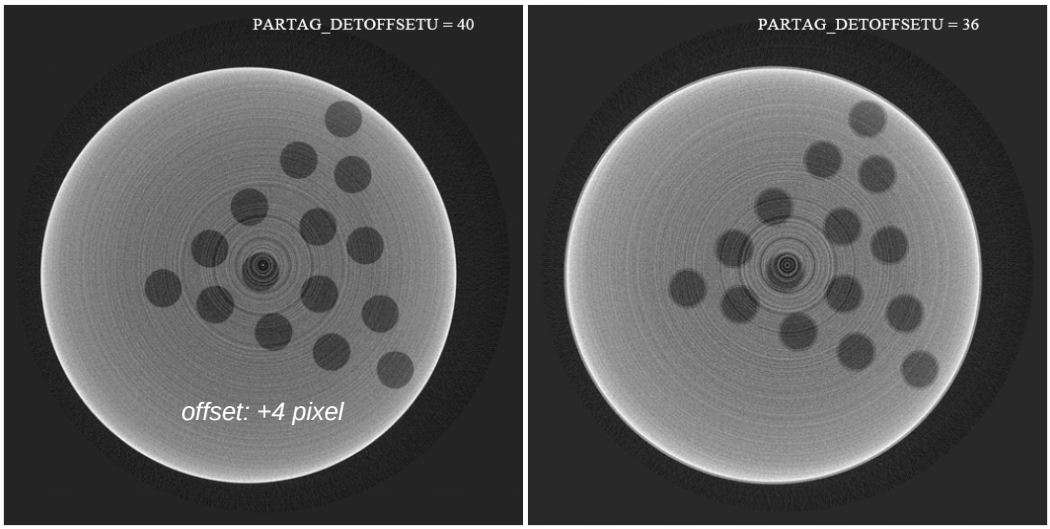

Figure 3.17 – A test object scanned to verify the detector offset: the double contouring effect is visible in the uncorrected slice on the left.

When all the above specified procedures were successfully completed, the CT system can be considered satisfactory aligned, with respect to the rotation axis, and the further acquisition and reconstruction procedures will be consequently simplified.

3.4.3 Ring artefacts

Ring artefacts appear as concentric rings superimposed to the true features of the reconstructed slice. They are generally due to the non linear response of some pixels of the detector (Sijbers et al., 2004) that can occur for several reasons as drifts of the CCD elements caused by electronic or temperature instability, beam fluctuations, local overloading of the incoming photons. Ring artefacts are also strictly related to the beam hardening. Further, it's worth noticing that the polychromatic spectrum, even when a

[1] The sinogram is the collection of the detector row corresponding to the mid-plane from all the projections acquired during a complete 360° rotation.

middle energy is selected, contains single high energy photons that can impinge onto the detector locally saturating some of its pixels.

Even if particular awareness can be used during the scan in order to control the beam hardening effect, to avoid the local saturation of the CCD pixels and to appropriately acquire the flat filed images (usually by multi-frame mode to minimize the fluctuations), the ring artefacts can never be completely removed.

Thus a post-processing cleaning procedure is normally needed. At the TOMOLAB a fast and quite efficient method was adopted which convert the output slices into polar coordinates, apply them the following filter and reconvert them to Cartesian coordinates:

```
ave = sum(PolarImage)/ntheta;
smo = medfilt1(ave,25);
dif = ave-smo;
for i = 1:ntheta
    PolarImage(i,:) = PolarImage(i,:) - dif;
end
```

where `ave` represents the average value of each column of the polar image, `smo` is the smoothed version of `ave` calculated by a mono-dimensional median filter and `dif` is the difference between the average and the smoothed values. It's worth noticing that the filter width is a free parameter that should be checked (here it is assumed of 25 pixels). Finally, each row of the polar image is subtracted with the previously calculated `dif`.

Figure 3.18 shows the result of the applied correction. The routine, written in the IDL environment, takes few seconds for the entire operation on the single slice working on a Dual Core AMD64 Opteron Processor workstation with 2.00 Gb of RAM.

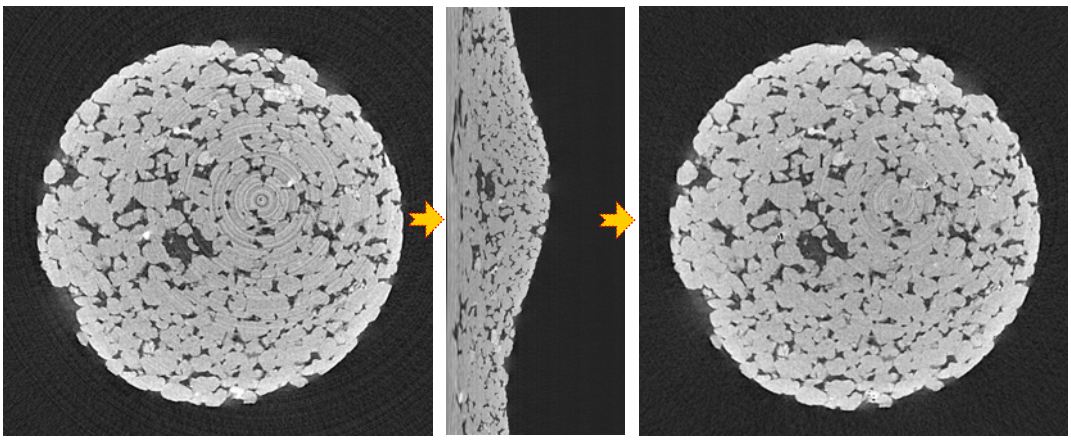

Figure 3.18 – A rock slice before (left) and after (right) the correction for ring artefacts. Filter is applied to the polar version of the slice (middle).

Conclusion

In this chapter we highlighted the main mechanisms that concur to set the final spatial resolution of the images which are mainly related to the intrinsic characteristics of each component and of their combination (cone-beam geometry, polychromatic beam, focal spot size, achievable magnification factor etc.).

We understood that each of these aspects contributes to alter the produced images. Noise, artefacts and distortions all corrupt the acquired radiographs and, even more, the reconstructed slices or volumes: they cannot be completely removed, as we demonstrate with many practical examples, but proper correction procedures can be adopted in order to reduce their harmful effects and to correctly interpret the obtained data.

After the optimization of the hardware facility parameters and the treatment of the arising artefacts, we could start to collect a high resolution digital data. All the information contained in the data need to be accurately analyzed and quantitatively investigated: this calls for advanced tools and intensive digital image processing which will be described in the next chapter.

Chapter 4

Digital Image Processing

The recent developments of X-ray μ-CT can provide high resolution images of natural and artificial porous media both by synchrotron light sources and desktop facilities. Such datasets are extremely rich in information although overwhelming in size, which sometimes makes difficult their manipulation. Automated computer investigation is then necessary in order to extract quantitative measurements from the images. Digital Image Processing (DIP) includes the fundamental tools to optimize and hence analyze the three-dimensional products obtained by μ-CT, in order to make it meaningful for most of the scientific or industrial purposes.

The DIP methods need to be tailored for a wide range of applications, each one requiring its own customization. Our research activity has been developed in collaboration with different research groups affording many different topics (geology, material science, engineering, archaeology): in all cases, the main effort was usually done to provide an effective support for the subsequent data processing.

In the present chapter an overview will be given on the main topics of DIP. Because the possibility of deriving physical properties of materials from the 3D digital images of their microstructure sounds very attractive, special emphasis will be reserved to the description of the three-dimensional porous space via powerful tools like *skeletonization* and *network characterisation*. Within a collaborating project, we have developed a custom-designed software package, named PORE3D, which will be presented here.

4.1 μ-CT & DIP

Due to its non-invasive nature μ-CT represents a suitable investigation tool in many different applications. As mentioned, there is a wide range of industrial fields of interest, from the mechanical components and electronic devices, to the aerospace manufacturing. Concerning materials science, a μ-CT examination is capable to reveal failure mechanisms, micro-cracks, internal defects, morphological details, stress-strain behaviours. It can provide the base elements for modelling the internal microstructure of the investigated materials for mechanical, thermal, acoustic or fluid transport simulations.

Among the wide spread of applications, porous media and multiphase systems represent the most intriguing ones. A porous material can be simply viewed as a kind of solid material that has holes inside: such an intuitive definition implicitly contains the assumption of homogenization as well as the concept of length scale (Garboczi et al., 1999), which imposes to quantitatively compare the voids size to the typical object size and to evaluate how voids are distributed throughout the sample.

The investigation of natural porous media like rocks and soils occupies a considerable position in the field of geosciences (Spanne et al., 1994; Coles et al. 1996; Wildenshild et al., 2002) for petroleum engineering purposes (Knackstedt, 2004; Al-Kharusi and Blunt, 2007) as well as for several environmental topics like contaminant remediation in aquifers, geothermal energy production, CO_2 sequestration (Iglauer et al., 2008), waste disposal or landfill design. For all the mentioned cases, the geometrical and morphological description of the rock pore space plays a fundamental role in governing fluid and thermal transport through the medium. The related research activities often involve the comprehension of multiphase fluid flow in complex systems with simultaneous presence of oil, water and air (Culligan et al., 2006).

On the other hand, several artificial porous systems are of great interest especially for their innovative industrial potential: metallic foams (Olurin et al., 2002) are massively employed in the automotive and building area due to their lightness and robustness, plastic foams (Saadatfar et al., 2004) are employed in the automotive and packaging industry because of their noise and vibration insulating properties, cellular materials exhibit many useful mechanical, thermal and acoustic properties (Maire et al., 2003; Knackstedt et al., 2005), amorphous ceramic foams are optimized for filtering (Appoloni et al., 2004), other composite and cementitious materials are continuously upgraded to satisfy new technological requirements (Baruchel et al., 2000; Gallucci et

al., 2007). Again, the internal microstructure of all these materials has to be accurately described to correlate their engineering performances via numerical models in order to reproduce and efficiently employ them.

Also in the bio-medical research field μ-CT is massively used in the study of hard tissue to characterize trabecular bone architecture related to artificial implants behaviour or teeth implants (Weiss et al., 2003; Rustichelli et al., 2004). The analysis of hydroxyapatite scaffolds was recently carried out by μ-CT (Fierz et al., 2006) for the optimization of the manufacturing process and the implant design needed in medical surgery for the substitution of large bone defects.

Other particular applications of μ-CT are in the field of food science (Falcone et al., 2004; Lim and Barigou, 2005; Mousavi et al., 2007), paper (Ramaswamy et al., 2004; Goel et al., 2006) or wood (Steppe et al., 2004) industry and the conservation of archaeological finds (Gerlach et al., 2006; Bertrand, 2007).

The solution of practical problems involving porous media requires the knowledge of microscopic properties of the porous matrix, like porosity, permeability, tortuosity, effective thermal conductivity, effective electric conductivity and others. The μ-CT scan and volume reconstruction represent the first step which contributes to qualitatively explore the internal structure of the samples; then, in most of the cases, the subsequent image processing of the digital dataset is absolutely necessary in order to catch the numerical values that allow the proper evaluation of the investigated parameters for each application.

In the past, the characterisation of three dimensional pore space and of the intrinsic texture of porous material has been based mainly on direct laboratory tests like adsorption (BET surface area) or pore filling procedures (e.g. Hg porosimetry). The visualization and image analysis of the materials structure were often limited to bi-dimensional views, obtained via optical or surfaces methods (e.g. thin sections, SEM).

Nowadays, the extension of many concepts to the 3D case represents not a trivial task, requiring a computationally heavy effort as well as the development of many specific new methodologies. Although the human eye is the best candidate to appreciate and distinguish in digital images the visualized texture and the hidden features (that usually can be difficultly discovered by automated procedures) the need of treating a huge amount of (3D) data, often in a short elapse of time, imposes to develop efficient and fast DIP toolkits.

Due to the fact that a digital image is already divided into single elements, i.e. the pixels, it seems naturally adapted to the application of discrete computational methods such Finite Differences Method (FDM), Finite Elements Method (FEM) or Lattice Boltzmann method (LBM). The computational mesh can be in fact directly based on the pixel-representation of a porous matrix, resulting from the reconstruction process of the slices. Care must be taken in obtaining the tomographic images with a resolution that both enables the identification of the smallest features of interest and, at the same time, provides in the reconstructed volume the sufficient data content adequate for the correct and meaningful calculation of the desired properties.

The processing of the reconstructed slices can be intended of two categories: commonly one refers to the Digital Image Processing (DIP) as to the manipulation of the original image in order to improve its quality, alter its visualization or modify its appearance, furnishing as the final product of such operations another (different) image. Instead, one refers to the Digital Image Analysis (DIA) as to the application of specific tools, algorithms and routines in order to extract numerical measurements from the original image. In the following of this chapter, we will use interchangeably these two definitions, as we consider globally the DIP as the procedure by which, starting from any given image, both qualitative and quantitative results can be achieved including the expression of the geometrical, topological or morphological parameters of interest.

4.2 The PORE3D package

In recent years many research groups, spread all around the word, developed software and custom codes for 2D and 3D image analysis. We acquired a wide experience on software aimed at the analysis of the 3D digital dataset. Particularly, for the aspects concerning the visualization, and basic image processing tools, freeware programs like MRIcro (http://www.sph.sc.edu/comd/rorden/mricro.html) or ImageJ (http://rsb.info.nih.gov/ij) revealed to be very useful, especially the last one that is continuously upgraded (Burger and Burge, 2007). Other specific targeted software has been deep experienced as, for instance: the 3DMA packages by Lindquist (http://www.ams.sunysb.edu/~lindquis/3dma/3dma.html), intended to the 2D and 3D analysis of the pore space of complex systems (Lindquist, 1999); the Blob3D program by Ketcham (http://www.ctlab.geo.utexas.edu/software/index.php), adopted for the quantitative analysis of 3D data (Ketcham, 2005). This also opened the way to a fruitful collaboration with Dr. Richard Ketcham of the University of Texas at Austin.

Our main aim was to merge together many of the features implemented in the above-mentioned software, customizing in some case their characteristics or adding new tools, on the basis of the specific know-how we have acquired inside the SYRMEP collaboration.

However, there is no versatile software capable to solve all the specific problems arising from images of different materials and structures. It sounds very dissimilar in fact the investigation of porous media made up of bubble-like pores (e.g. volcanic rocks, artificial metallic and plastic foams, products from the food industry like chocolate and cheese), fibrous materials (e.g. felts, natural wood, artificial composite materials) or randomly distributed materials (e.g. most of the reservoir rocks and many other industrial products).

This paragraph illustrates the specific tools that were developed for the micro-structural analysis of tomographic datasets collected both at the SYRMEP beamline of Elettra and at the TOMOLAB facility, forming the entire DIP procedure typically applied to porous media. The algorithms and routines were implemented and hence assembled into a home-developed program named PORE3D (see Figure 4.1). This is a research code designed to produce morphological and geometrical analysis on 2D and 3D digital images, written in MATLAB© language. It contains the basic tools to manage digital images (e.g. filtering, segmentation, visualization) and specific libraries for advanced analysis (e.g. separation, distance labelling, skeletonization, feature extraction) which have been tested with satisfactory results on our X-ray μ-CT data sets.

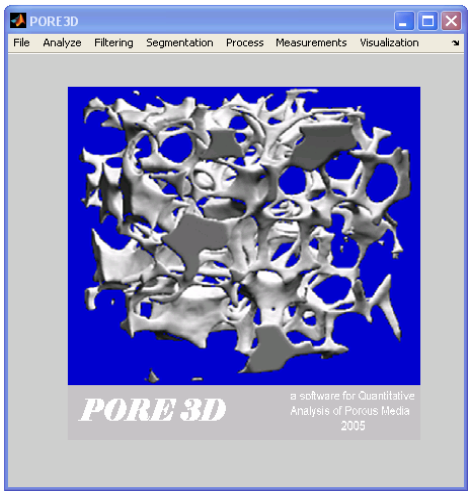

Figure 4.1 – The PORE3D main window: the program is a home-built package under MATLAB© language, aimed at the micro-structural analysis of tomographic dataset.

The PORE3D software follows the intent to create a user-friendly program suitable for a wide range of application and adaptable to different media, from low to high porosity systems. A completely self-contained version is working also as a stand-alone executable version capable to run without any MATLAB© license, under all Windows platforms. The program is designed with an open architecture, so that new modules and functions, devoted to solve specific claims, can be later easily added into the original main program.

4.2.1 Filtering

Before further quantitative estimation of the materials properties, tomographic images usually need to be improved in their quality, minimizing the noise and other artificial defects arising from the acquisition and reconstruction steps (Barrett and Keat, 2004). Particularly, with regard to the three-dimensionality of the observed objects, denoising plays an essential role, since the human eye is not able to extract the same amount of information (by interpolation, low-pass filtering, classification, etc.) as in the 2D case.

Generally speaking, a denoising algorithm should be able to preserve as much as possible the signal while reducing the noise sufficiently. As mentioned in the previous chapter, partial volume effects, beam-hardening, ring artefacts etc. all require specific algorithms to be corrected (Kak and Slaney, 1988, Sijbers and Postnov, 2004), which are often applied during the reconstruction from projections both in the spatial and in the frequency domains. However, many unphysical structures (e.g. edge and surface irregularities, random Gaussian noise, salt and pepper disturb etc.) can be later removed directly on the slices, thus allowing a better thresholding for segmentation (see next paragraph) and a more accurate evaluation of the object features. To this purpose, conventional noise reduction methods working on the 3D dataset were implemented.

The *median smoothing* filter is widely used to reduce noise in the images with minimal alteration to the object geometry. The filter replaces a voxel with a grayscale value equal to the median of the grayscale values of the neighbouring voxels. The filtration can be performed in 2D on the single slice, or in 3D. When possible 3D is preferable, in order to consider also the information content from the upper and the lower slices. In fact, operating by a bi-dimensional kernel on the single slices the filtering process introduces some kind of artefacts which appear in the coronal (*ZX*) and sagittal (*ZY*) planes (i.e. the planes orthogonal to the filtering direction) as slice-oriented

straight lines altering the image and affecting further steps of the objects analysis (see Figure 4.2). When filtering, the mask radius has to be chosen opportunely as well as the number of iteration the filter will be repetitively applied to the image.

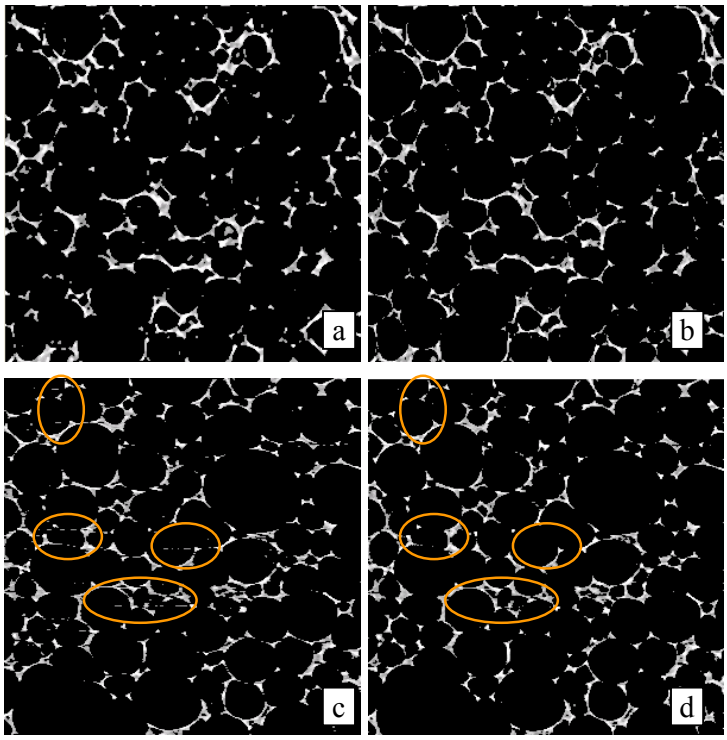

Figure 4.2 – A comparison between the median filter applied in 2D on single slices (a, c) and in 3D on the entire volume (b, d) of a polyurethane foam sample. The voxel size is 9 μm. The slice plane (XY) is showed (a, b) which is correctly filtered by both the methods and the transversal plane (ZX) is reported (c, d) for comparison. In the transversal plane numerous slice-oriented straight lines are visible when 2D median filter is used (some of them is highlighted in the yellow circles).

Similarly, the *averaging filter* computes the mean value of the gray-level voxel within a rectangular filter-window surrounding each pixel. The filter has also the effect of smoothing the image. A *Gaussian* filter instead can be applied to reduce noise in the image much more quickly than the median smoothing filter, but with the inconvenience of altering the geometry of objects as it tends to blur the boundaries. Gaussian filter has weights specified by the probability density function of a normal distribution. The *Wiener* filter is again a low pass one, specifically suitable when an intensity image has been degraded by constant power additive noise and blurring. It filters the image by means of pixel-wise adaptive filtering, using neighbourhoods to estimate the local image mean and standard deviation.

Figure 4.3 reports an overview of the described filters, applied to two kinds of materials exhibiting a quite different internal microstructure.

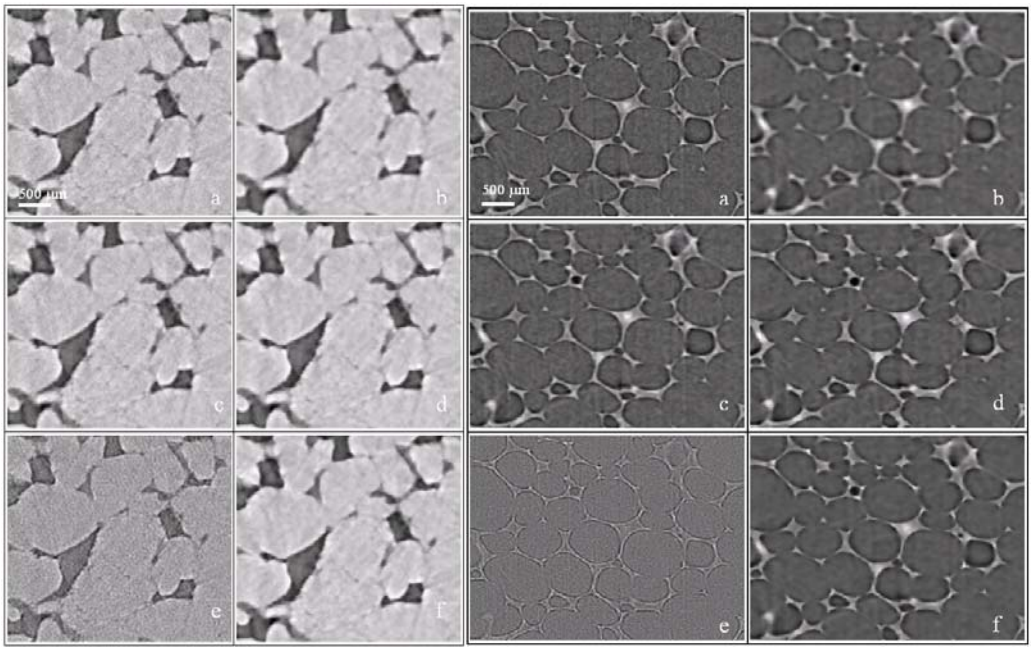

Figure 4.3 – A comparison between different filters is presented for rock sandstone (left) and polyurethane foam (right) exhibiting very different internal structures. The voxel size is 9 µm for both the samples. A ROI is visualized before filtering (a). Results are respectively from average (b), Gaussian (c), median (d), sharpening (e) and Wiener (f) filters.

Other kinds of filters can be used to re-modulate the image contrast, sometimes with the declared aim to enhance the visibility of particular details or of the objects edges. Thus, the *sharpening* procedure returns an unsharp contrast-enhancement filter, created from the negative of the Laplacian filter. It enhances the edges of the objects essentially subtracting an image from a smoothed version of itself. This can make edges appearing more distinct, although it may also increase image noise. However, sharpening represents one of the most impressive filters since it brings out details that seemed not to be there before. *Contrast Enhancement* transforms the values in an intensity image, so that the histogram of the output image approximately matches a specified histogram. One can refer this filter as to a histogram equalization method: this is particularly useful when you want to compare different grayscale images, or when you stack into a single volume slices that have each own grayscale.

4.2.2 Segmentation

Most of the 3D data obtained by X-ray μ-CT are grayscale images including void and solid space. To evaluate the porosity, as well as many other geometrical and morphological parameters, it is necessary to operate on a binary image that is an image containing only zeros - to represent the void phase - and ones - to represent the solid phase. Segmentation refers to the determination of the phase type of each voxel in the image. Although the most general case involves a two-phase system made of voids that need to be separated by the solid framework, also multi-phase separation is often required in order to distinguish different solid or liquid phases inside a composite material. Extracting the volumetric grade distribution of a particular phase from a μ-CT volume is in fact of a large relevance for many scientific/technical disciplines ranging from the environmental research to the modeling of normal operation in many chemical or process engineering installations.

Segmentation represents the first heavy modification of the image appearance in the DIP and can be considered as a key step propaedeutic to any further analysis. The basic concept lies in the proper selection of a threshold value on the intensities histogram of a grayscale image (i.e. the slice). Once this threshold value is identified, voxels are assigned, according to their value if lower or higher than the selected threshold, to one of the two (or more) classes representing that specific phase.

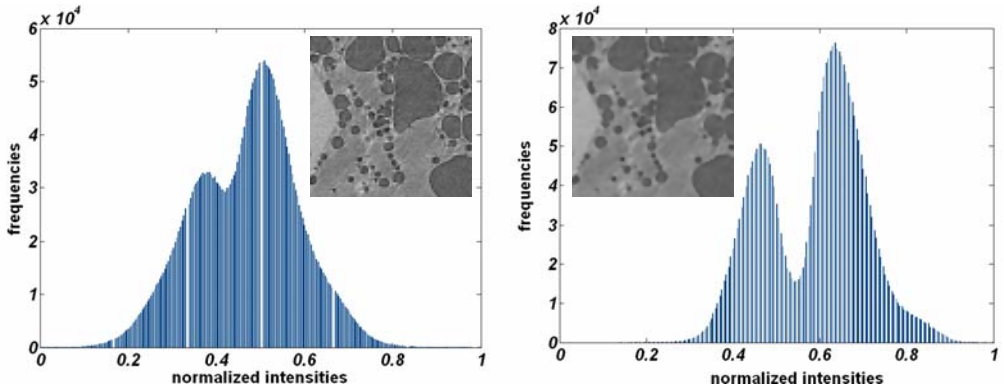

Figure 4.4 – A comparison between the intensities histograms of a VOI of a volcanic scoria sample, before (left) and after (right) a 3D median filter is applied: the bi-modal distribution represented by the two peaks is clear in the second case, thus a threshold can be selected. Images were acquired at TOMOLAB with a voxel size of 5.5 μm. Gaseous vesicles and a phenocrystal on the left are visible.

Several segmentation algorithms are widely described in literature (Otsu, 1979; Mardia and Hainswotrh, 1988; Pal and Pal, 1989; Oh and Lindquist, 1999). Advanced

methods based on efficient and elegant algorithms like local thresholding or edge detection are well suited when two or more phases have to be distinguished looking at an intensity histogram which does not exhibit evident valley between the peaks associated with each phase. The histogram showed on Figure 4.4 was obtained from a VOI of volcanic scoria sample and shows the typical bi-modal distribution of grayscale levels of two-phase systems (with the vesicles originated by the expanding gasses representing the void phase).

The simplest method to manually or automatically segment is the *simple thresholding* by which a single threshold value is chosen. The automatic thresholding method implemented into the PORE3D program computes global threshold using Otsu's algorithm (Otsu, 1979).

Segmentation can be done in two ways: either working slice by slice, looking at the intensity histogram of the single slices, or working on the 3D volume, considering the bulk intensity histogram. If the latter is the case, a preparatory equalization process among the different slices of the stack is needed.

However, after segmentation, it is usually preferable to perform a *cleaning* procedure in order to remove artefacts, small defects, undesired objects: these can be both isolated void voxels that are unphysical (i.e. produced during segmentation) and solid flecks eventually suspended into the void phase (see Figure 4.5).

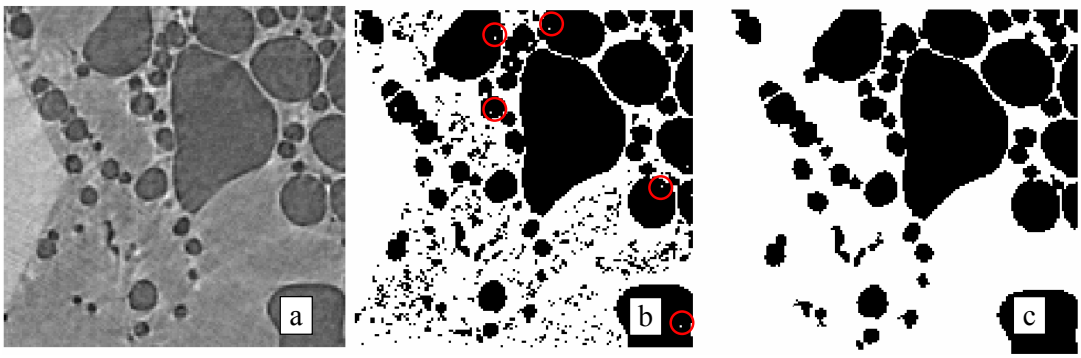

Figure 4.5 – The original ROI from a volcanic scoria sample (a) is segmented by simple thresholding method (b). No filtering procedure was applied in order to emphasize the noise effects: most of the noise content is still retained after segmentation. The result of a cleaning procedure performed both on the void and solid phase is showed too (c).

Basically, this is obtained by morphological (erosion/dilation) and topological (connectivity check, objects counting) operations; from another point of view this can be seen as a filtration procedure, that is implemented for both solid and void phase,

according to a previously determined size of the particles to remove. Both the operations can be easily performed in three-dimensions, thus allowing a better evaluation of the connectivity (e.g. a single black voxel appearing like the top of an iceberg in one slice could be connected in 3D to a bigger pore structure, so it should be preserved). It's worth mentioning that such a cleaning procedure is always very sensitive and should be carried out with maximum care. After segmentation it is also possible to remove the closed voids (i.e. the blind pores or bubbles definitely not connected to the border of the VOI) in order to get the so called effective porosity instead of the total one.

Instead of using a simple threshold method for segmentation, one can use more sophisticated algorithms, such as *indicator Kriging* (Oh, 1999), which is an iterative way that considers each voxel of the image and its neighbours to establish the membership to the void phase or to the solid matrix. This kind of local thresholding requires a-priori identification of an amount of voxels: this is not normally a problem in most of practical applications where a large percentage of voxels can be easily assigned to a class just looking at the intensities histogram. Instead, local methods help to identify the edge voxels (i.e. typically voxels occupying the valley between two peaks) which are affected by a severe partial volume effect (i.e. this means that part of each voxel is filled with one phase and part with the other phase).

In the *adaptive thresholding* method the threshold changes dynamically over the image, selecting an individual threshold for each pixel, based on the range of intensity values in its local neighbourhood (i.e. using the mean of considered neighbours as a local threshold). It is an efficient method for an image whose intensity histogram doesn't contain distinctive peaks for using global thresholding.

The *maximum entropy* method bases on the maximization of the inter-class entropy on the intensities histogram (Sahoo et al., 1988). It produces results similar to the Otsu's method, but it reveals to be more sensitive to the image random noise.

The *K-mean Clustering* (Cheung, 2003) algorithm is preferable when the original images have to be partitioned into three or more classes: it is an iterative scheme that operates over a fixed number of clusters. Each class has a centre which is the mean of all the samples in that class. Each sample (i.e. a voxel over the image) is assigned to the class whose centre has the minimum distance from it. The algorithm is recursively repeated until no class changes occur or after a predefined iteration number.

All the above mentioned methods are implemented into the PORE3D program, and will be used to process the μ-CT datasets in order to furnish the best results according to the investigated material type.

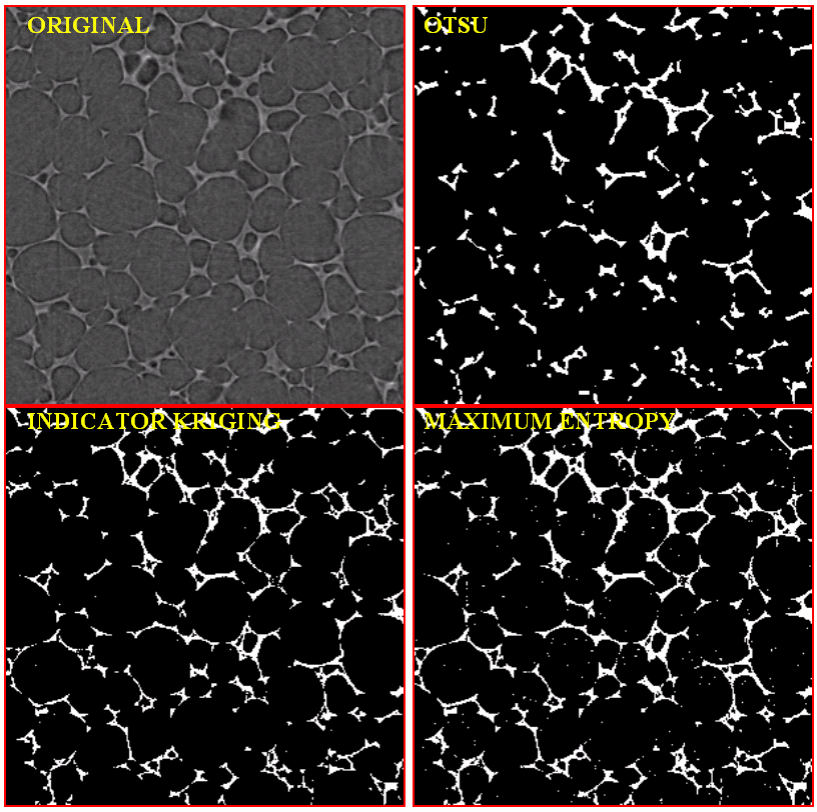

Figure 4.6 – Different segmentation techniques are applied to the same ROI of polyurethane foam.

4.2.3 The Representative Elementary Volume (REV)

The reconstructed grayscale slices are generally 16 bit images. When a volume is created by stacking multiple slices, several megabytes can be occupied and need to be managed for further image visualization and processing. Thus volumes are later converted to 8 bit format for further processing. To give an idea, an 800×800×800 voxels volume occupies 512 Mb or 1000 Mb respectively at 8 bit and 16 bit.

Also for these reasons it's a common practice first to crop out an appropriate sub-volume from the reconstructed dataset, on which any further measurements can be easier performed. The so-called Representative Elementary Volume (REV) should be small enough to be easily handled and at the same time large enough to represent almost all the internal features of the pore space: in other words it should comprehend both the

small features or small pores and the general texture of the material matrix in which they are immersed.

The REV concept differs from the idea of Region Of Interest (ROI), or of Volume Of Interest (VOI) in 3D, as the ROI is just a small portion of the reconstructed slices which contains the features of interest, but in principle is not representative of any property.

The REV analysis can be based on the rough stabilization of a selected parameter. Typically, the porosity ϕ could be chosen, which is defined as the ratio of the void voxels to the total ones:

$$\phi = \frac{\#\, voxels \in voids}{X \cdot Y \cdot Z} \qquad [4.1]$$

where X, Y and Z are the cube dimensions in pixels. Of course, instead of referring to the void phase for the calculation of porosity, the volumetric grade of any other phase could be considered.

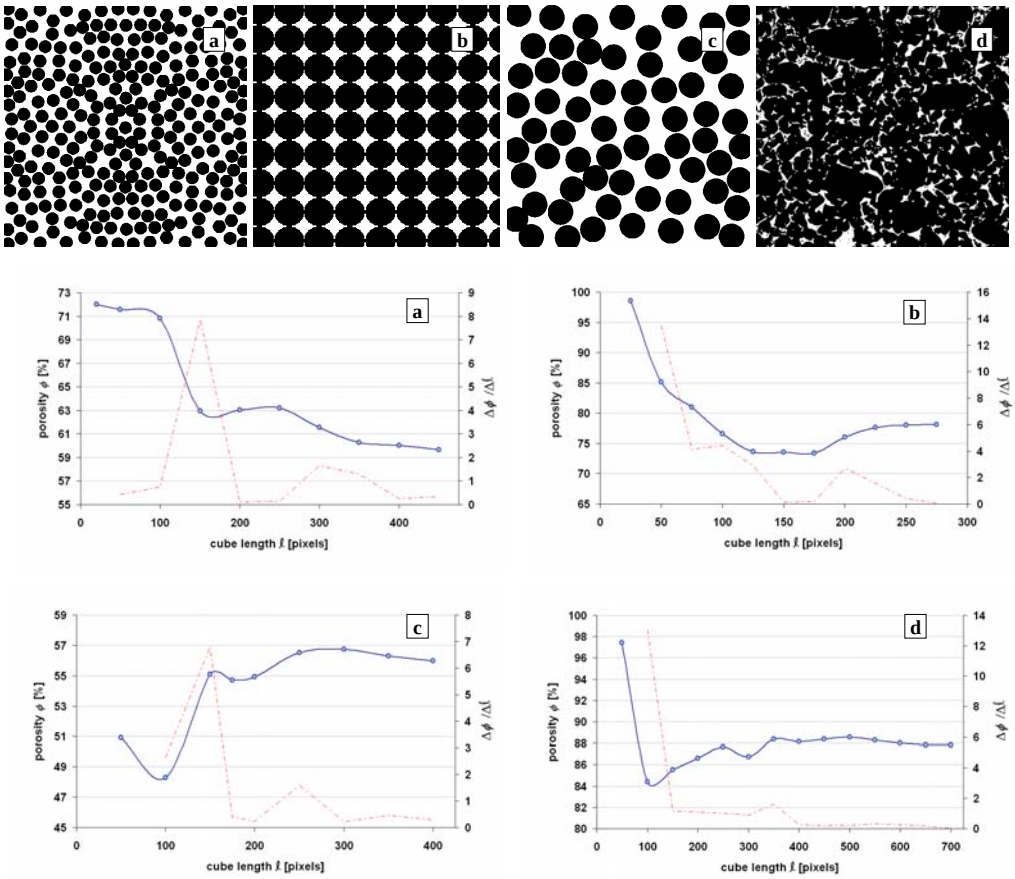

Figure 4.7 – The REV size evaluated for different artificial systems (a, b, c) and for a real randomly distributed sample (d). Graphs show the calculated porosity values as a function of the REV size (blue continuous line). The first discrete derivative is used to visualize porosity stabilization (red dotted line).

However, larger and larger VOI are considered and the porosity is evaluated until a stable value is reached. The process should take into account the material homogeneity and the degree of anisotropy, which can influence the measured values.

In PORE3D a tool is available that automatically compute the REV size for common porous media, trying to roughly stabilize the porosity value while the sub-volume size grows up (see Figure 4.7).

4.2.4 The two point correlation function

Some parameters of purely geometrical nature (e.g. porosity and specific surface area) can be calculated using correlation functions too. In general, an *n*-point correlation function is a measure of the probability of finding *n* points in the region of space occupied by one phase.

The one-point correlation function F_{n1}, for example, is directly related to the porosity ϕ since it can be viewed as the probability of finding a single point of the same phase. In other words, F_{n1} just counts the elements of a selected phase over the given volume. By formula, it can be written as:

$$F_{n1} = \langle f(x) \rangle = \phi \qquad [4.2]$$

where the angular brackets indicate a volume average over the spatial coordinate x. Similarly, the two-point correlation function F_{n2} can be interpreted as the probability of finding two points, separated by a lag distance r, both belonging to the same phase. The two-point correlation function should be evaluated on the entire three-dimensional dataset for statistically homogenous media, while could be calculated along a preferential direction for anisotropic media. By formula, it is:

$$F_{n2}(r) = \langle f(x) \cdot f(x+r) \rangle \qquad [4.3]$$

From the above definition, it derives that F_{n2} calculated at lag zero provides again the total porosity ϕ of the system (Al-Raoush and Wilson, 2005):

$$F_{n2}(0) = \phi \qquad [4.4]$$

From F_{n2} the specific surface area S of a two-phase medium can be estimated, which is defined as the area of the two-phase interface per unit of volume inside the medium. For three-dimensional elements, like those ones investigated by μ-CT, the specific surface area S is given by the slope of the F_{n2} at lag zero. By formula it is (Al-Raoush and Wilson, 2005):

$$\left.\frac{dF_{n2}(r)}{dr}\right|_{r=0} = -\frac{S}{4} \qquad [4.5]$$

It's worth noticing that, due to the discrete nature of a digitized medium, the evaluation of $F_{n2}(r)$, imposes that the distance r can conveniently be measured as an integer number, in terms of pixels, with the start- and end-points located at the pixel centres (Yeong and Torquato, 1998).

Also the mean object size can be roughly estimated by the two-point correlation function, taking the value at the first minimum (usually referred to as the decay length) of the function (Garboczi et al., 1999). For systems exhibiting a high degree of correlation (e.g. regular networks or repeated elements), F_{n2} reveal a certain periodicity, which is eventually related to the characteristic object size. In Figure 4.8 regular elements are showed as non-overlapping squares representing a system with a high correlation degree: the square size is about 8.2 units, which approximately corresponds to the first minimum of the function or to the periodicity length.

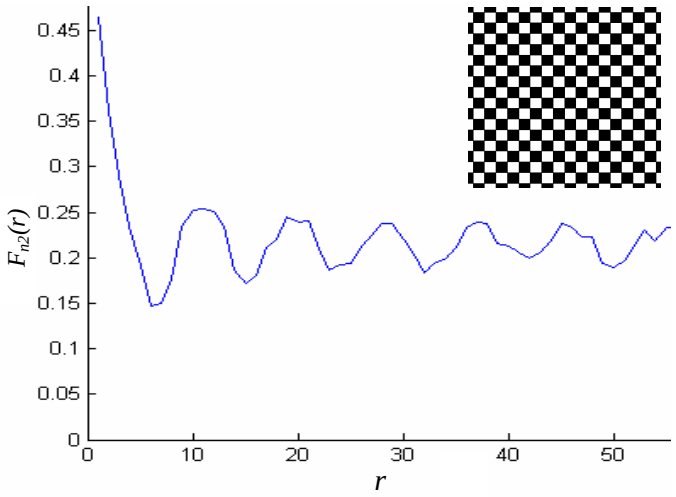

Figure 4.8 – A typical two-point correlation function, calculated for the regular elements showed in the top-right box. The non-overlapping squares represent a system with a high correlation degree: the periodicity, which is particularly evident for the short-range order, is roughly equal to the squares size.

Other descriptors such as the pore chord length, that is the length in the void between two solid voxels with a given direction, are also very useful to characterize the structure from 3D images (Levitz, 1998; Roberts and Torquato, 1999). The combination of one- and two-point correlation functions with these geometrical descriptors improves the capability to evaluate the connectivity and predict the macroscopic properties.

4.2.5 Object counting

Most of the algorithms adopted to extract quantitative information work on the segmented data. However, before measuring most of the object morphological properties like size, aspect ratio (i.e. the ratio between object principal axes), shape factor, roundness etc., the object itself needs to be identified and separated from the background and the other elements surrounding it. Thus, in the processing of bi- and three- dimensional images, a fundamental task is represented by object recognition.

The characteristic morphology (i.e. shape, thickness, connectivity with neighbouring objects etc.) of the observed objects plays an important role in the choice of the best method and algorithms to reach the final result. Regular shaped objects (like the rounded bubble inside volcanic rocks previously showed or, for instance, synthetic foams) require different strategies, if compared to irregular structures or directionally oriented objects (like those inside fibrous composite materials or the long fibres of the wood structure).

Generally speaking, after we get the cleaned segmented images, we cannot correctly identify all the objects yet. In fact, by applying an intensive statistical analysis like that one performed via the *n*-point correlation function (or, simply, via the autocorrelation function), a realistic representation of the microstructure and texture is obtained, but still no deep information on the single object properties are derived.

Instead, this is done by systematically inspecting each part in the data volume and processing it with morphology-based automatic tools. Usually, to correctly separate a cluster of two or more close objects, intelligent erosion/dilation operations have to be carried on, with maximum care in order to avoid deleting the thin structures while assuring the preservation of objects contours. Operations such as local erosion, ultimate erosion, dilation, propagation (Russ, 1999; Young et al., 1999), edge finding algorithms, watershed transform (Beucher and Lantejoul, 1979) are used to distinguish the individual objects, finding the three-dimensional connected groups of voxels which finally allow individual measures on distinct structures.

In Figure 4.9 the object counting (or labelling) operation is calculated by PORE3D via morphological processing on the thresholded image. Other tools are available in the PORE3D program based on the individual objects recognition, such as the measurement of the object volume, surface, specific surface area, as well as bi-dimensional information like the average number of objects per slice, which can give an idea of the homogeneity inside the material.

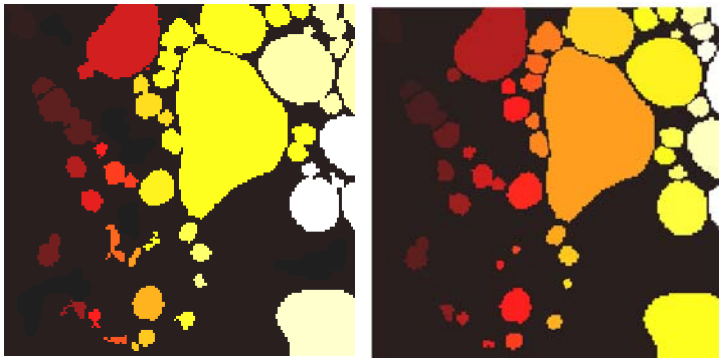

Figure 4.9 – Object counting before (left) and after (right) morphological separation. The volcanic scoria sample previously introduced is shown. Different colours are used to represent different objects. The algorithm is applied in 2D on the single slice.

To give an idea of the possibilities introduced by the morphological toolkits, in Figure 4.10 an original binary image (belonging to a 3D binary volume) is sequentially treated by ultimate erosion, distance transform, and watershed transform, to separate and thus label the different pore objects.

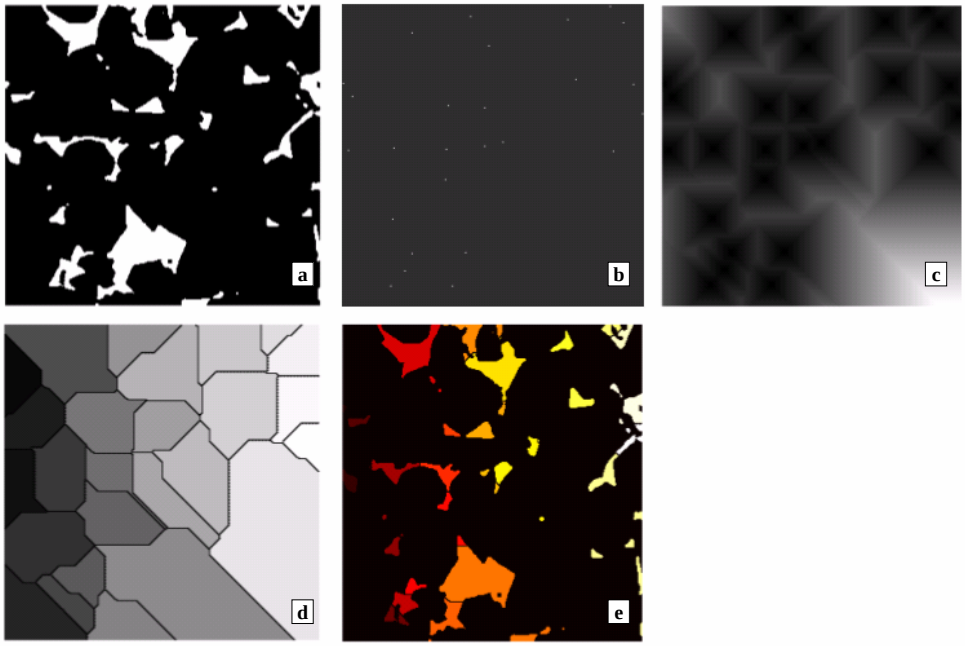

Figure 4.10 – Morphology-based functions are applied to the binary image (a) to separate and count the objects. The processing operates in 3D on the entire volume: for clarity reasons just one slice is shown. First, object centres are extracted via ultimate erosion (b), then distance transform is applied (c), followed by watershed transform (d): individual objects are finally labelled by different colors (e).

4.2.6 Skeletonization

Since features extraction from 3D segmented images is generally a computationally heavy task, we calculate the skeleton which reduces a digital object to a simpler version that still retains the essential features of the original one. Skeletonization is a thinning technique to reduce the dimensionality of the segmented image providing the topological invariance (Attali and Montanvert, 1997). When the skeleton is centred with respect to the boundaries of the original object, it is referred to as the Medial Axis (MA) or medial-surface. These are two well-established definitions in morphology literature (Silin et al., 2003; Giblin and Kimia, 2004).

For an object in continuum space, the MA is the union of one-dimensional curve segments. Medial axis is a morphological descriptor which significantly represents the geometrical and morphological feature of the original object (this implies that the original shape can be in principle completely reconstructed from its skeleton). Roughly speaking the skeleton is a network, made up of paths and nodes, from which important information about the connectivity, the tortuosity, the percolation properties and the permeability of a porous medium can be deduced. The complexity of such a network is self-evident. Medial axis extraction is a very difficult and delicate operation, whose success depends not only on the original images quality, but also on the efficiency of the particular algorithm which is applied.

Thinning is the process of reducing the shape of a digital entity which repetitively deletes the border points of an object satisfying topological and geometrical constrains until a smaller set of points is attained that approximates the true skeleton. We implemented into the PORE3D package the Lee, Kashyap, Chu (LKC) thinning algorithm (Lee et al., 1994), where the Euler characteristic and connectivity are preserved to guarantee the invariance of topological properties.

The procedures for skeletonization and MA extraction on 3D volumes move either from parallel thinning procedures on Boolean volumes with a continuous check on topology preservation and removal of the so-called simple-points only (Lohou and Bertrand, 2004), or from distance transform 3D matrices (Remy and Thiel 2005; Sanniti and Nyström 2005).

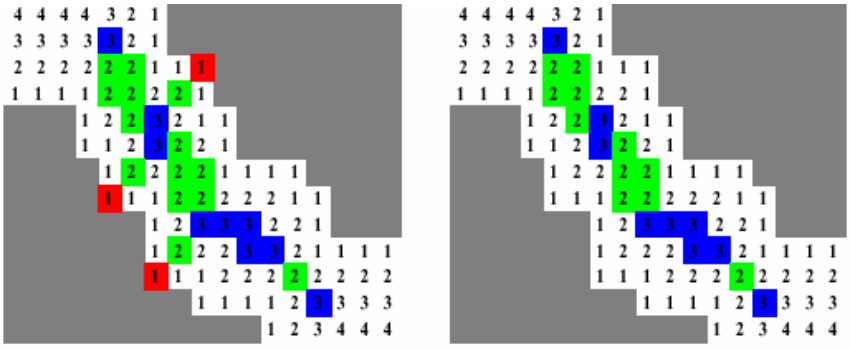

Figure 4.11 – The distance labeling used for burning the void space and extracting the skeleton. The skeleton raw version (left) contains spurious branches, due to the irregularities of the object contours, that should be later removed via specific criteria (right).

The so called *distance labelling* is an iterative procedure where the pore voxels are burnt layer by layer, starting simultaneously from the outer shell formed by voxels lying next to the grains, and progressively moving to the unburnt voxels at a rate of one layer per iteration (see Figure 4.11). The idea is to igniting everywhere at once on the objects external surface, allowing the fire to burn deeper layers at a constant rate, thus reducing the object layer by layer. The fire is said to directionally extinguish at a point if two fire components, travelling in opposite directions, arrive there at the same time. The set of all points within the object where the fire directionally extinguishes is the medial axis of the object. Thus the burn number (i.e. the numerical value that represents the distance between the voxel and the closest grain surface) gives the radius of the largest sphere centred at that point which lies entirely in that object (Lindquist et Lee, 1999). Considering this problem from a different point of view, the burnt volume can be seen as a sort of distance-transformed matrix that can be used to state a criterion for further void space analysis.

We followed two modifications suggested by Venkatarangan to the LKC algorithm (Venkatarangan, 2000). The first is to employ conditions at the boundary of the image region, to take into account the fact that the object shape is unknown beyond the boundaries of the VOI. The second is that the surface voxels (i.e. those ones that are candidates for burning) are processed in strict order according to the number of neighbours they have in the opposite phase (e.g. the solid phase), the highest first.

However, the irregularities at the void/grain interface (basically due to digitalization process) strongly affect the MA appearance (see, as an example, Figure 4.12 where skeleton is calculated for a simple object). This is the reason because many unphysical

and spurious branches come out and need to be further removed, generally according to a length criterion that penalizes shorter paths. Also isolated branches should be removed, or paths that form close loops.

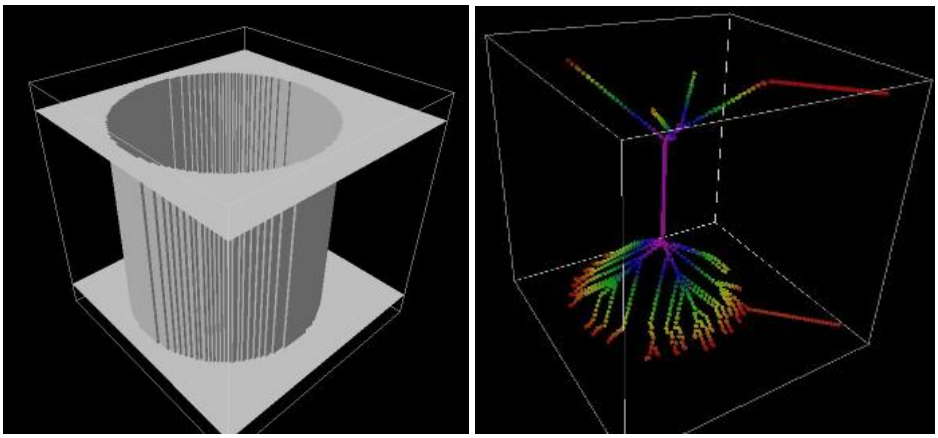

Figure 4.12 – The skeleton of a cylinder: irregularities of the surface (mainly arising from the digitalization) and boundaries effects strongly condition the MA appearance: the many spurious branches created need to be further removed. Rainbow color scale is proportional to burn numbers.

Once the medial axis has been pruned in order to keep only the useful information, a large number of parameters can be measured describing the real pore space topology and geometry (i.e., pore size distribution, connection number, path length, throat radius, pore shape factor etc.). The results are as much accurate as medial axis is representative of the porous medium and properly reduced to a mono-dimensional curve.

In Figure 4.13 the skeleton is obtained from an artificial dataset made of regular cubic elements together with the skeleton of a typical complex porous structure. A rainbow colour scale is related to the burn numbers assigned to each void voxel applying a distance transform to the digital pore space. Indeed, in principle, blue voxels are located on nodes contained in the largest bubbles, while red voxels are very close the solid phase and generally represent the terminal part of a blind path.

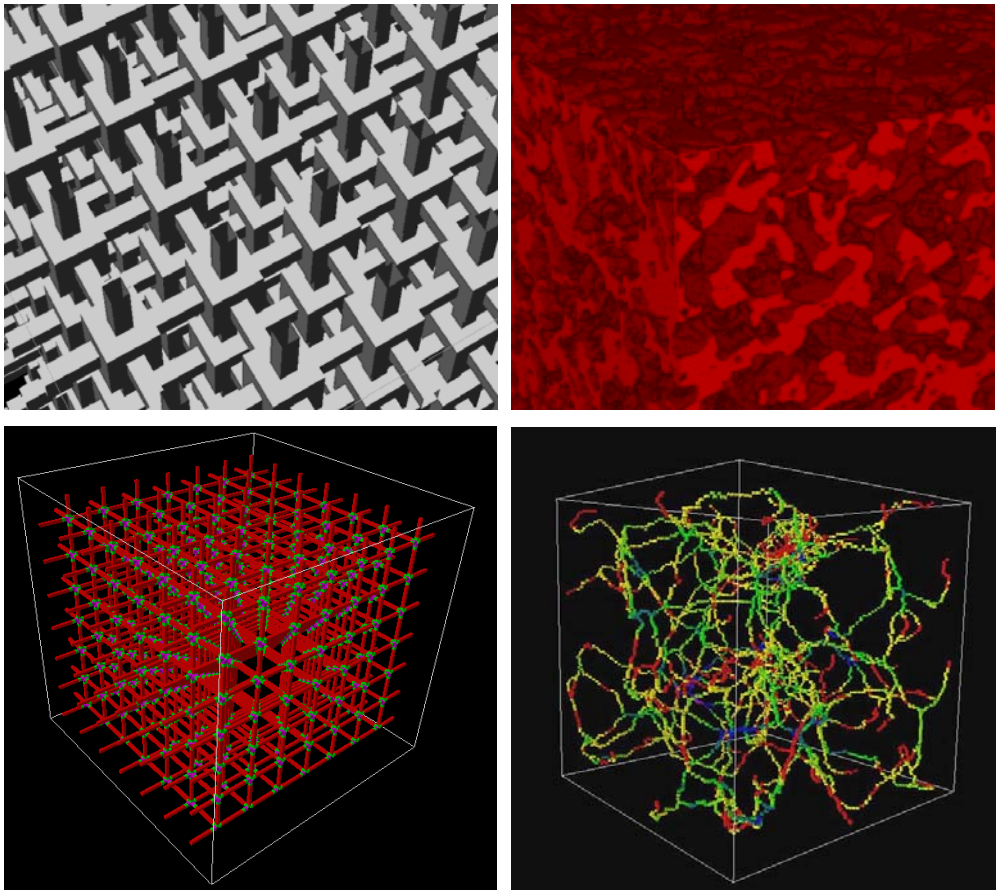

Figure 4.13 – Skeleton obtained from an artificial dataset of regular cubic elements (left) and from the pore space of a complex porous structure (right). A rainbow color scale related to the burn numbers is assigned to each void voxel applying a distance transform to the digital pore space.

Visualizations refer to cubic volumes of 300×300×300 elements, while MA were extracted using the commercial software 3DMA developed by Lindquist at Stony Brook University.

Employing the MA as a navigational explorative tool, many other geometrical and morphological parameters can be accurately quantified: for instance, the burn number distribution shows the relative number of voxels in each burn layer, i.e. at each discrete distance normal to the void surface (Lindquist, 1999). The burn number distribution can estimate the diameter of the minimal sections along each pathway. Instead, the connectivity is readily calculated from the medial axis as the average number of paths connected to each node. Connectivity has a critical influence on transport properties such as permeability and its quantification is important for understanding the relationship between microstructure and transport properties themselves (Wong, 1999).

One can measure the path length distribution which corresponds to the distance between the centres of any two adjacent nodes: the measured distance is not the straight line one, but the distance along the medial axis of the pore channel, so it is influenced by the tortuosity of the pore space.

4.3 A new pore space network characterisation approach

In the previous paragraphs we have described morphological measurements in 3D for the void[1] space characterisation (connectivity, pore-body/throat classification, shape factors, virtual fluid intrusion) based on computed intensive digital-thinning operations for skeletonization and medial axis extraction from 3D digital images. To what it concerns the skeletonization, the major algorithms include the thinning based method, the maximal ball method and the Voronoi diagram based method.

Delurue (2002) developed a methodology using the Voronoi diagram to find the skeleton from general 3D images to partition the pore space. Seeds for tessellation are selected on the border of grain and void to create discrete segments (Yu et al., 1998). Then the skeleton can be extracted based on a selection of Voronoi branches after the Voronoi diagram is generated based on these predefined segments.

The maximal ball algorithm (Silin et al., 2003; Silin and Patzek, 2006) starts from each voxel in the pore space to find the largest inscribed spheres that just touch the boundary. Then those included in other spheres are viewed as inclusions and removed; the rest are called maximal balls and describe the void space without redundancy. Locally, the biggest maximal balls and the smallest ones allow sorting the ducts by diameter, thus discriminating between their narrow and large portions.

In the next paragraph we present an alternative method that is measurably faster and allows sub-voxel definition of the void space network (Schena and Favretto, 2007). The method allows extracting - based on morphological considerations only - the centred and shortest stream-lines - i.e., the paths - to follow in order to go through the pore space from one given point to another and to exit. In addition the method penalizes long, narrow pore-throats in favour of short stubby/ones - i.e., it has a built-in

[1] We will refer here to the void space as to the phase of interest for performing the characterisation: of course, the method could be applied likewise to the solid phase or any other phase identified in the investigated materials.

exemplification capacity. It exploits well-established mathematical methods successfully applied in medical endoscopy. One of the valuable points of the method is the relatively high speed if compared with traditional methods, basically because we eliminate local voxel-based check operations thus avoiding any time consuming loops over the entire matrix.

4.3.1 Mathematical background

Instead of medial axis we introduce the definition of *path*. Although we will rigorously define it below, in simple words it can be described as the shortest centred walk-way that traverses the void space from a given point, called the start-point, to another given point, called the end-point. Even if we do not consider explicitly fluid flow, renouncing for an instant to a rigorous definition, the reader can think of the path and visualize it as the fastest fluid thread for laminar flow regime from the start- to the end-point. The procedure we present here to extract the path, uses recent mathematical results for the solution of partial differential equations, namely the fast marching methods proposed by Sethian (1999). The problem is set out in a continuous fashion and the paths, while maintaining original resolution of the μ-CT dataset as only voxel-scale information is available, can have sub-voxel definition. A single path can be seen as part of the MA, but the collection of all the paths does not include all the MA branches. Indeed, the method grades the paths and selects only the shortest ones. It is shown in the next section that the length measure is weighted by the local diameter of the void channel.

We use these paths to virtually follow the geometric penetration of a tracer particle intruding from the inlet (start-point) through its evacuation at the outlet site. Start- and end-point, i.e. the extremes of the paths, are automatically detected on the sides of the selected REV. It's worth mentioning that the set of extracted centred paths cannot be compared to a 3D curve skeleton because topology of the complete three-dimensional space is not conserved and segments of the MA passing through very narrow channels can be missed.

Since two or more paths extracted can have one or more overlapping sections we finally resolve this feature that visually results in the branching of the extracted paths at the intersection points and can be seen in violation of the uniqueness of the solution of ordinal differential equations. This apparent violation is due to the fact that each path is generated by a calculation with a different end-point.

Let S be the 3D volume of a porous media, associated 3D Boolean matrix:

$$\begin{aligned} S(i,j,k) &= 0 \qquad \forall\, i,j,k \in voids \\ S(i,j,k) &= 1 \qquad \forall\, i,j,k \notin voids \end{aligned} \qquad [4.6]$$

where the i,j,k coordinates identify each voxel inside the digital volume.

To each voxel where $S(i,j,k)=0$ the Distance Transform (DT) is applied to assign a number that is the distance between that voxel and the nearest nonzero voxel of S. To establish an intuitive parallelism with the previously mentioned methods, the maxima values of the DT are placed on the centres of the maximal balls that one can imagine to inflate in the void space. The 2D transects formed by the intersection of the void space with the sides of the rectangular parallelepiped volume (i.e., our REV) connect the void space with the external environment. The centroids of these transects are taken as extreme points for the void space.

We like to extract now, with sub-voxel definition, the particular 1D curve γ - i.e. the path - running in the void space that is the shortest path connecting the centroid point (initial or start point) of one transect with the centriod point (end point) of another transect. In addition, the curve γ is forced to be centred as much as possible with respect the edges of the void space (i.e. the points of the curve should also be close to the centres of maximal balls).

In a continuous fashion, the problem can be written as an optimization problem:

$$d(Start,End) = \min \int_{s(Start)}^{s(End)} \left\| \gamma'(s) \right\| \cdot D(\gamma(s))^{\alpha}\, ds \qquad [4.7]$$

where s is an arbitrary curve parameter, $d(Start,End)$ is the distance between the start and end-point and $D(x,y,z)$ is a cost function which assumes the value zero in the solid phase locations.

The values of D on the voxel grid (i,j,k) are given by the DT of S. At a point (x,y,z) the values of $D(x,y,z)$ are re-calculated by cubic spline interpolation from the voxel-grid values. On a point (x,y,z) that is also a centre of a maximal ball, $D(x,y,z)$ corresponds to its radius.

As a special case, when $D=1 \quad \forall (i,j,k) \in S$, the integral is the length of the curve and $D(Start,End)$ is the Euclidean distance between the start- and the end-point, and $\gamma(s)$ is not centred. The parameter α is set equal to -1, so that the minimum values of

$\gamma(s)$ are on the centre of maximal balls. To solve this problem we use the level set method (Sethian 1999). One can define the energy function:

$$U(x) = d(Start, X) \qquad [4.8]$$

The level set C is the set of points that can be reached with minimal cost t from the start-point:

$$C = \{X \setminus U(X) = t\} \qquad [4.9]$$

The minimal cost path is orthogonal to the level curves:

$$\frac{\delta C}{\delta t} = \frac{\vec{n}}{D} \qquad [4.10]$$

The gradient of U is normal to level set C and the gradient norm of U is the value of the derivative in the normal direction:

$$\|\nabla U\| = D(x, y, z)^{\alpha} \qquad [4.11]$$

thus the function U satisfies the Eikonal equation. An efficient method that uses level sets for solving the Eikonal equation was proposed by Sethian (1999). In practice, given the potential D values on the original voxel 3D grid, the values of the energy U are computed following an upwind finite difference scheme that moves from the start-point toward the end-point. The front U is propagated in a computationally efficient way using a technique proposed by Sethian that is called the fast-marching method.

The review paper by Cohen and Kimmel (1997) and the more recent review with applications to the medical field by Deschamps and Cohen (2001) can provide details on the minimal path approach. The minimal path between the start- and the end-point is calculated by back propagation. Starting at the end-point, the steepest gradient descent guides the search of the next point in the path chain:

$$\frac{\delta \gamma}{\delta s} = -\nabla U \qquad [4.12]$$

Generally, U is computed on the coarse original voxel-grid and during back propagation the value of U is refined by cubic spline interpolation to retrieve the value on the higher definition grid where the geodesic curve path is defined. The fast marching method has some in commonality with the Dijkstra algorithm used in graph theory but allows a continuous formulation of the problem.

For many sets of data (i.e. high resolution X-ray μ-CT volumes segmented to binary volumes) the extraction of the curve γ is successful and thus U is smooth.

The result of the extraction of the centred minimal paths of the void space of a volcanic scoria is shown in Figure 4.14: iso-surfaces with iso-normal lighting together

with semi-transparency are used to better visualize the paths. Figure 4.15 shows the calculated paths (note that no overlaps occur) with a colour palette that reflects the diameter of the local maximal ball having centre on the path.

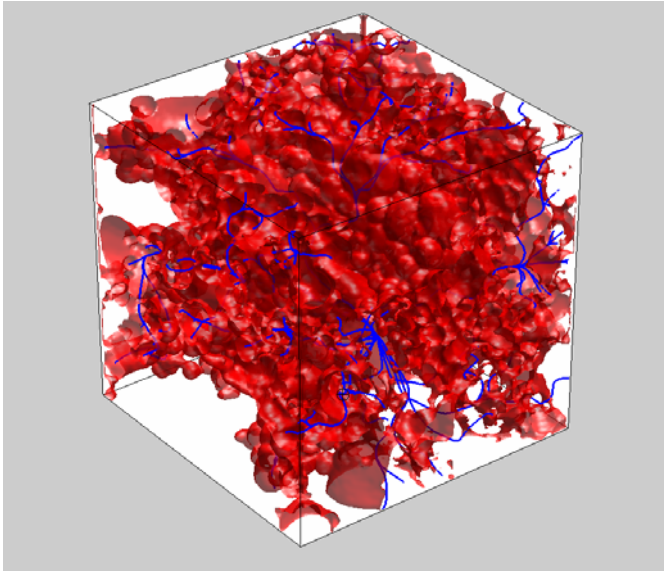

Figure 4.14 – The void space of a complex porous medium showed by isosurface and isonormal-lighting. Semi-transparency is also used to better visualize the extracted paths.

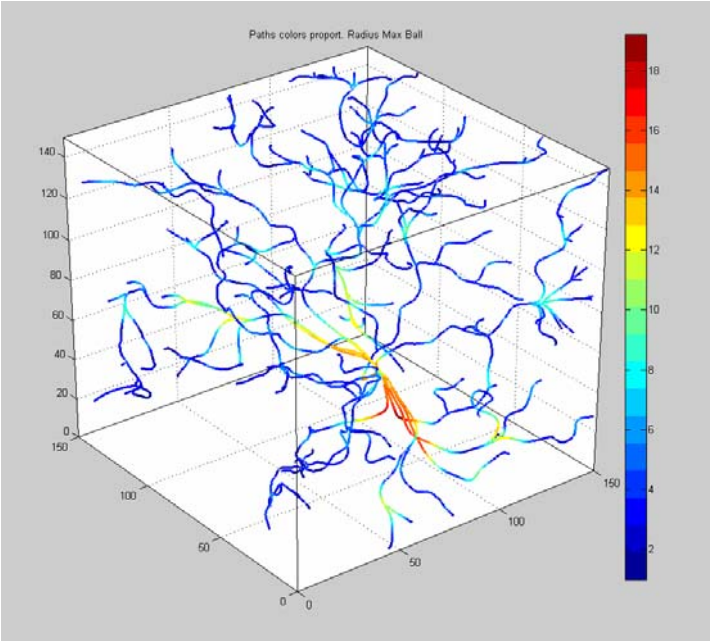

Figure 4.15 – Calculated paths are shown with different colors (note that no overlaps occur). The color palette reflects the diameter of the local maximal ball with centre on the path.

4.3.2 Feature extraction

The paths that the method extracts are centred with respect to the boundaries of the void space thus pass on the centre of maximal ball. To extract features and measurements on the paths, such as equivalent object diameters etc., irregular polygons on planes perpendicular to the paths are used that approximate the perimeter of the path cross-sections. The polygon area and the perimeter are calculated and the equivalent diameters of all sections along the path are derived. For each path segment, for instance, the sections with minimal area can be visualized as irregular polygons (see Figure 4.16).

Notice that all the extreme points are automatically located on the faces of the selected REV. A maximal ball positioning strategy distributes the maximal balls starting from the largest and imposing only the condition that the new ball should not overlap the existing ones. The coordination number, that is the number of throats intersecting a pore body or in network terms the number of paths entering and exiting a maximal ball, is calculated based on the sign of the distance of a point that belongs to a path to the centre of the sphere. A path-point having a distance to the centre of the sphere greater than (less than) the sphere radius is external (internal) to the pore. Thus, the change of sign of the distance indicates that the path intersects the sphere.

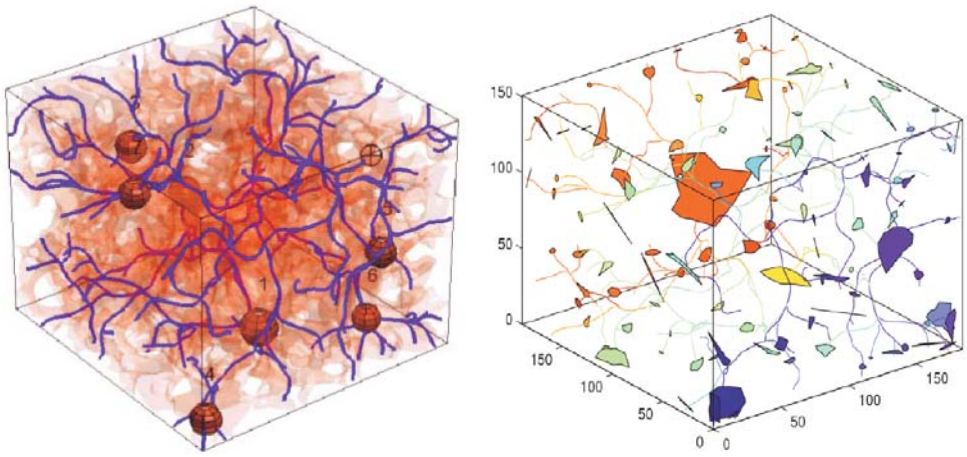

Figure 4.16 – Visualization of irregular polygons representing the minimal area sections of each path segment. Some maximal spheres placed on the path network according to the non-overlapping constraints. On the right, spheres are inserted into the pore space to demonstrate path centring.

Conclusion

In this chapter we pointed out the importance of the processing of μ-CT reconstructed data in order to extract quantitative information related to physical properties of the investigated materials. This analysis requires a specific know-how both on the material under study and on the DIP procedures.

Thanks to the experience matured within the SYRMEP collaboration we have been able to develop custom tools for the analysis of porous media.

In the next chapter we will present in detail a selected number of scientific applications.

Chapter 5

Applications to material science

During my stay at Elettra I had the opportunity to be involved in many different research projects in the field of material science and earth science involving the SYRMEP beamline and the TOMOLAB facility. In particular:

- three-dimensional investigation of volcanic textures and implications for conduit processes (Polacci et al., 2008);
- investigation of the pore space structure of oil reservoir rock samples with different permeability (Dong et al., 2007);
- quantitative evaluation of multiphase fluid distribution inside the pore space of sandstone samples (Dong, 2007);
- 3D visualization of CO2 gas capture and multi-phase flow behaviour in unconsolidated quartz sand (Iglauer, 2008);
- investigation of microstructure and mechanical properties of resonance wood (Caniato et al., 2007);
- microstructural characterization of foam and felts for noise control application (Bregant et al., 2007);
- optimization of process parameters in hybrid friction stir welding/TIG technique on aluminum alloys (Favretto et al., 2006);
- greenstone artefacts in prehistory: preliminary results and perspectives based on X-ray computerized microtomography (Bernardini et al., 2007);
- μ-CT application to a predictive evaluation of coralline algae structure (Bressan, 2007).

Among the mentioned activities, in this chapter we will present three selected examples of μ-CT studies which look rather representative applications to material

science. The aim is to give an overview on different applications, spread on a wide range of sectors, in which μ-CT can be of great help. The extraction of quantitative measurements from the acquired volume data will be performed by mean of the digital image processing (DIP) tools introduced in the previous chapter.

The first example describes the development of semi-automatic DIP in order to obtain a geometrical and morphological characterisation of a light porous material as polyurethane foams employed for their acoustical and vibrational insulating properties.

The second case illustrates an innovative approach followed in order to characterize the resonance wood microstructure. A natural material like spruce wood used to make piano soundboards was examined in order to model (by means of Finite Element Method, FEM) the acoustical behaviour of this material.

The third application concerns a metallic material such as aluminium, demonstrating the capabilities of μ-CT, in combination with image processing tools, to reveal defects in hybrid-friction stir welding (HFSW) joints, thus guiding the optimization of the process parameters.

5.1 Measurement of the characteristic lengths of foams and felts employed in the automotive industry for noise control applications

Cellular materials have many useful mechanical, thermal and acoustic properties but, in order to efficiently employ them, their morphological characteristics should be related to the engineering performances via numerical models. Foam properties are related to their cellular structure, the relative percent of open or closed cells, the average cell size, the local density and the degree of anisotropy (Olurin, 2002).

In this paragraph an experimental work is presented aimed to non-invasively investigate the intricate 3D pore space of a large set of polyurethane foam samples used in the automotive industry using μ-CT imaging at the SYRMEP beamline and at the TOMOLAB station.

The analysis has been proved as an effective method to visualize the microstructure of foam samples with a resolution absolutely adequate to reveal the main features of such kind of materials. Quantitative measurements on reconstructed volumes and precise recognition of geometrical elements were achieved by mean of standard visualization software and custom developed codes.

5.1.1 Noise control applications for the automotive industry

Research on the noise insulation techniques and on the perception of vibration has recently increased of importance in particular for the transportation industry (automotive and airplane) in order to minimize the negative impact on the personnel comfort and the handling of machines. Also small improvements can be sometimes of great industrial interest.

In the automotive field, many different materials are used with the purpose of improving the acoustical and vibrational comfort inside the passenger compartment: from simple massive barriers to more complex damping bituminous materials, foams and felts. These materials are typically arranged in multi-layers (see Figure 5.1) and many different combinations are in principle possible and, to be able to design and optimize in advance the acoustic and vibrational treatment with respect to the appropriate amplitude and frequency ranges, it is of paramount importance to appropriately model the physical behaviour of the constituent materials. While the modelling of massive barriers and damping bituminous materials does not present major difficulties, for felts and foams the situation is more complex. This happens because the porous microstructure of those materials is constituted by a solid frame (usually referred to as the "skeleton") saturated with a fluid (typically standard air) and it is the interaction between these two components that determines their physical behaviour at a macroscopic level. In particular, most of the dissipative processes that take place inside these materials and that make them useful for noise and vibration control are directly linked to this interaction. These porous materials attenuate airborne sound waves by increasing air resistance, thus reducing the amplitude of the waves, while the energy is dissipated as heat. For a flexible, open cell porous foam saturated with a fluid, the transport of vibro-acoustic energy is carried both through the airborne path (i.e. the sound pressure waves propagating through the fluid in the pores) and through the structure borne path (i.e. the elastic stress waves carried through the solid frame of the material). For most porous materials, used to reduce sound and vibration, these waves are coupled to each other, i.e. they simultaneously propagate in both the fluid and the solid frame but with different strengths. One of the major causes of the dissipation is the amplitude and the phase differences of the fluid and the structure borne waves. Additionally, other mechanisms occur such as the heat exchange between the fluid and the solid as well as the internal losses arising in the deformation of the solid. All these dissipation mechanisms are generally frequency-dependent.

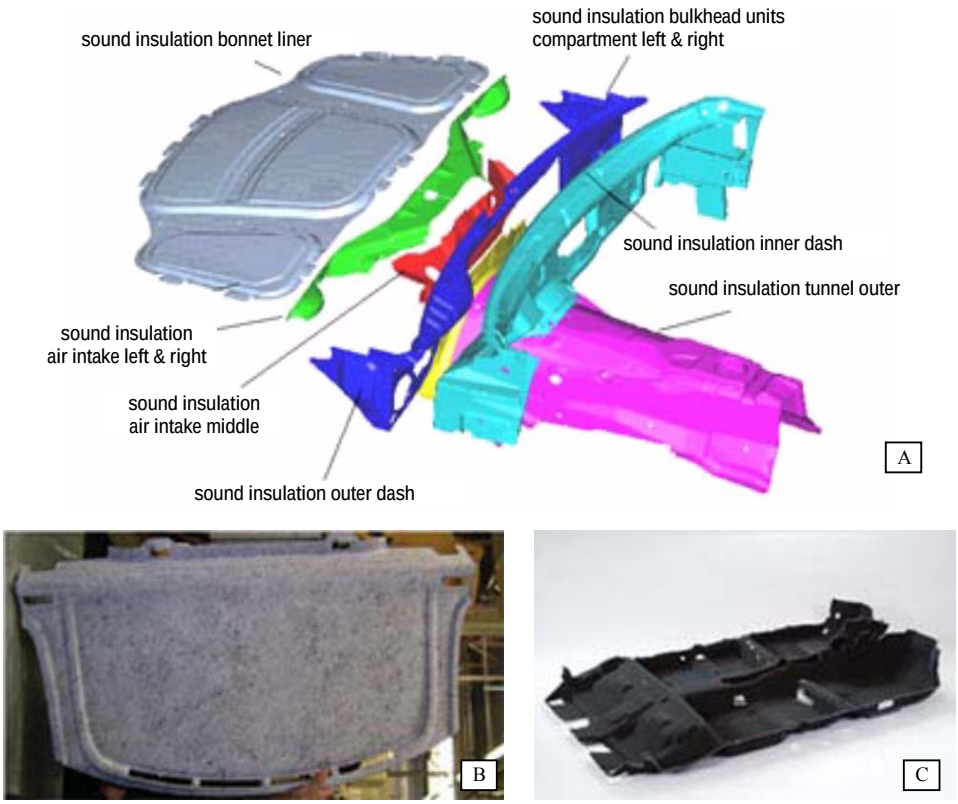

Figure 5.1 – Uses of foam and felts materials in vehicles (A): a car engine compartment panel (B) and an under floor panel (C).

Several authors discussed on the determination of (macroscopic) sound absorption properties of those materials starting from the two-phase microstructure revealed by microscopy (see Figure 5.2) or CT methods (Perrot et al., 2003). In order to link micro- to macro-scale one needs to point out the relationships between the three-dimensional topology, morphology and geometry of the cell structure and the macroscopic parameters measured via usually complicate laboratory tests.

Since several years, one of the most adopted theories to describe the two-phase behaviour of porous materials is the Biot-Allard model (Biot, 1956). This model describes in detail the dynamic equations for a porous material, starting from stress-strain relationships that are deducted on the basis of a very elegant Lagrangian theory. In these relationships, a porous material is characterized through a set of 15 parameters. Some of these are necessary to characterize the skeleton (e.g. its density and its Young's modulus), some others are necessary to characterize the saturating fluid and, eventually, some parameters are necessary to characterize the interaction between the two phases.

It is not the case to make here a detailed list of all these parameters, but it is important to mention that some of these are of a purely geometrical nature: they do not

depend on the dynamic properties of the two phases but just on the geometry of the material microstructure. Among these parameters, the porosity ϕ (i.e. the fraction of the total volume inside the material that is occupied by the saturating fluid), the tortuosity τ (an adimensional parameter needed to characterize the inertial interaction between the solid and the fluid phase) and the thermal characteristic length Λ' (which can be expressed as twice the pore volume to pore surface ratio). For typical materials used in the automotive field, the porosity can vary from 0.85 % to 0.98 % (such high values make quite difficult the DIP of the tomographic data), while the tortuosity can vary from 1.0 to 3.0.

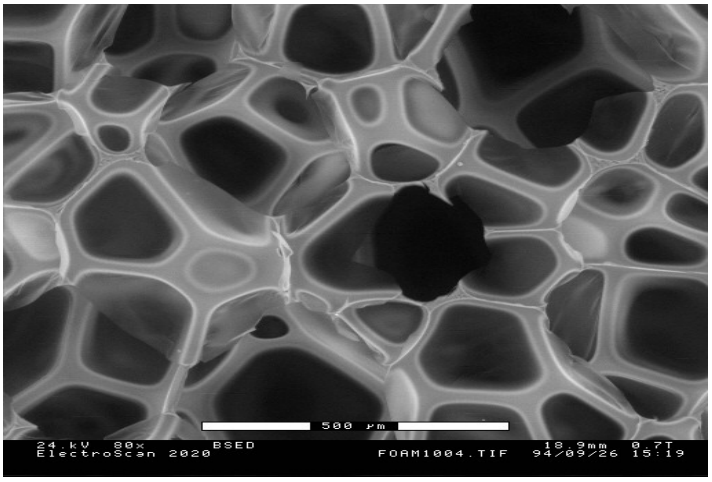

Figure 5.2 –The foam microstructure imaged by scanning election microscopy (SEM).

The evaluation of the parameters necessary for the Biot-Allard model is generally carried out experimentally on material samples, using mainly indirect methods: the parameters value is deducted from the measurement of other quantities, on the basis of some assumptions and simplified physical laws. Just to make an example, the porosity is typically measured in the following way: a sample of the material is mounted in a cylinder with a known volume and the cylinder is then mounted in the measurement device. A valve closes the system when the measurement starts and the initial pressure in the system is the same as the atmospheric pressure. Using a piston, the measurement system creates a known volume change, which creates a pressure change in the fluid that saturates the porous material. By knowing the initial volume of the sample, measuring the applied volume change and the corresponding pressure change, the porosity can be calculated using Boyle's law, assuming that the whole process takes place at constant temperature (and neglecting the volume change of the porous material

structural frame). As one can see, several assumptions are made in this procedure: the air has to behave as a perfect fluid, the process has to take place at constant temperature, the volume change of the material skeleton has to be negligible and it is by no means clear how far these assumptions are actually fulfilled. The situation is similar (or even worse) for the tortuosity: one of the most widespread methods used for its evaluation is based on ultrasonic techniques that simply cannot be applied to some materials like compressed felts. Moreover, the scatter among the results obtained by such indirect procedures from different laboratories is still much too high.

On the other hand, in the automotive sector, the procedure of transforming foams (solid-fluid interactions / different interfaces and boundary conditions) or multilayer sandwiches (foam / massive layer / felt) into equivalent single layered materials doesn't seem to be adequate anymore, thus more direct realistic simulations are required. To this purpose the detailed knowledge of the internal structure of the material seems to be the only conceivable way to derive the requested constitutive laws.

Instead, the intricate structure of foams and felts can be examined using 3D imagining techniques like the X-ray μ-CT followed by intensive DIP. The latter can be used to create computerized models of the investigated samples and to derive their geometrical properties and characteristics, fundamental for the creation of the numerical models of the materials used both for structural acoustics and fluid flow applications without altering the material structure by the measuring procedure.

Some works have been done in the past on liquid or aqueous foams (Montminy, 2004; Lambert, 2005) to understand how the foam structure changes in time. Few ones (Maire, 2003) focused on the geometrical characterization of organic and inorganic (for example bread and metallic) foams. The acoustic properties of rigid-frame porous materials were also treated (Brennan, 2001; Han, 2003). Not many authors (Elliot, 2002; Kinney, 2002; Youssef, 2005) focuses on PU foams, trying to extract information about the under stress (up to 80%) behaviours of such kind of materials. There is however a lack of bibliographical references on the use of the μ-CT scans to measure the characteristic dimensions used in the vibro-acoustic modelling, that instead represent one of the most common application, especially for materials normally exhibiting very high porosity level and working in very low stress (2-5%) condition.

5.1.2 Sample preparation, acquisition and reconstruction

The present experimental activity concerns the μ-CT tests carried on at the SYRMEP beamline and at the TOMOLAB station on several samples of polymeric foams used in the automotive industry. Two different sets of samples were analyzed: the first series were cut out with a blade from the central part of a large foam mat to perform the scans with the most regular cell structure. To increase the statistics, avoiding local variances of the foam microstructure, four samples were considered from different zones of the original mat, with a square base of around 5×5 mm and a length of approximately 15 mm. The μ-CT measurements were performed at the SYRMEP beamline (see Figure 5.3). The size of the samples was selected in order to fit the horizontal field of view of the detector. The foam sample was fixed with plasteline on the turn-table to assure its stability during the rotation. Pure adsorption images and phase contrast ones were acquired on the same sample during the tests, just varying the mutual distance between the sample and the detector.

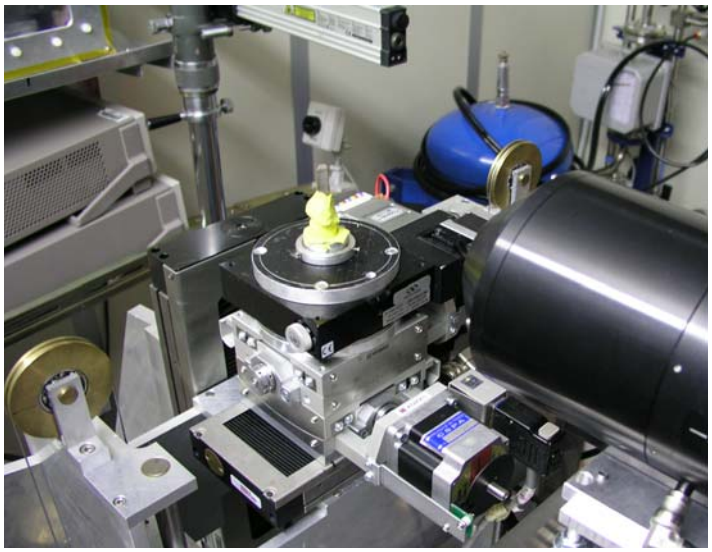

Figure 5.3 –The foam sample placed on the turntable for scanning at SYRMEP.

The optimal energy was founded at 18 keV, on the base of the sample attenuation characteristics. A set of 1440 projections, taken by the CCD camera as 12 bits grayscale images during a 180° rotation, have been processed in order to reconstruct each single slice. The optimal sample-to-detector distance D_{SD} was found at 15 cm. The pixel size, thus the nominal spatial resolution of the acquired images, was of 4.5 μm. The slice thickness corresponds again to the pixel size.

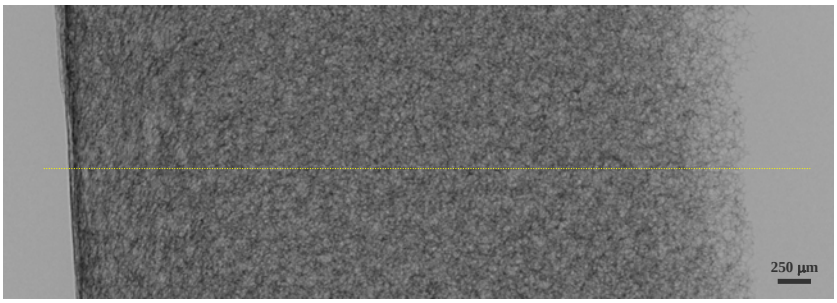

Figure 5.4 – One of the projections of the foam sample (SYRMEP).

As an example, the slice corresponding to the yellow row line in the Figure 5.4 was reconstructed from the planar projections: the result is shown in Figure 5.5.

The microstructure of such foams consists of a number of strut light elements connected at a number of joints. As known, foam is a substance formed by trapping many gas bubbles into a liquid or a solid. In the specimen used in this test the gas (air) is surrounded by an open-cell polyurethane matrix. As expected the air bubbles are easily recognizable inside the CT images and it is noticeable how these tend to be rather round far from the foam face and quite deformed close to the outer surface zone.

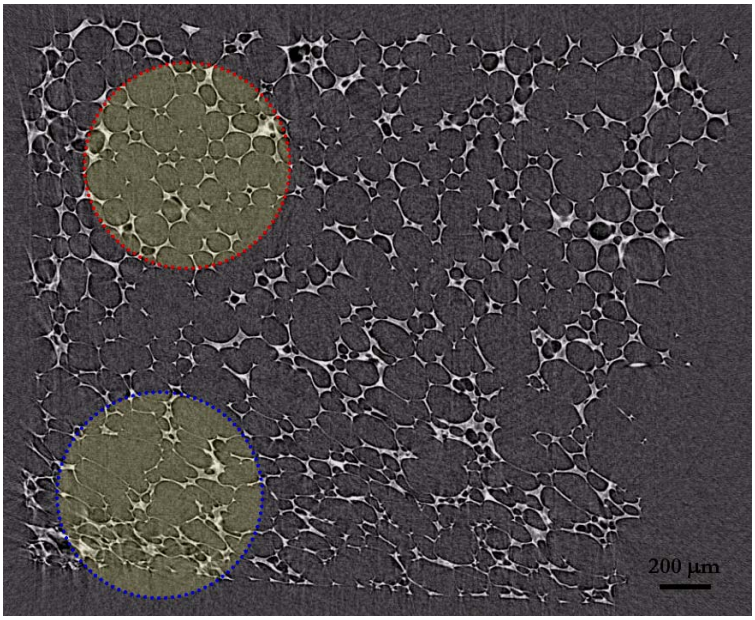

Figure 5.5 – A reconstructed slice of the foam sample (the red and blue circles are drawn to evidence the very different cell structure between the inner and the outer parts of the material).

A non-woven felt was also considered, as it represents another material commonly employed in the automotive sector for the realization of insulating parts. Similarly to the foam case, regular samples were cut out with a blade from the felt mat (see Figure 5.6)

and four tomographic scans were performed. Felt is a non-woven cloth that is produced by matting, condensing and pressing fibres. These fibres form the structure of the fabric. Felt is often used in automotive sound packages in combination with nobler material for its low cost and acoustical properties.

Figure 5.6 – The felt mat from which samples were extracted.

Due to the nature of that material, to minimize the small movements of the fibres at the sample edges (caused, for example, by the normal air flow in the room environment surrounding the sample) and so the subsequent scatter and the resolution loss, the sample has been wrapped in a thin layer of parafilm before being fixed onto the rotating table for scanning. This thin film, confining the felt structure, is easily recognizable in the planar images as well as in the reconstructed slices.

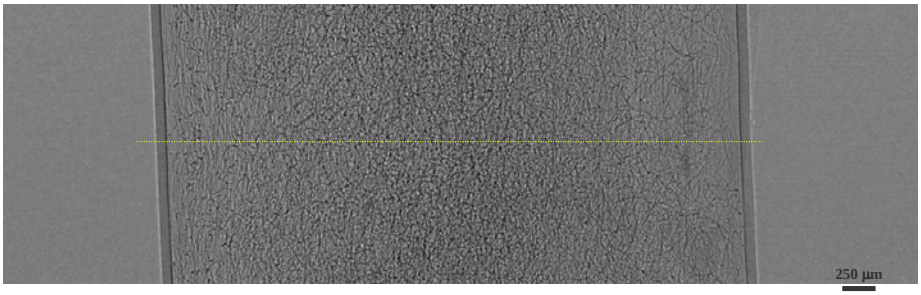

Figure 5.7 – One of the projections acquired of the felt sample (SYRMEP).

As an example, the slice corresponding to the yellow row line in the Figure 5.7 was reconstructed from the planar projections: the result is shown in Figure 5.8.

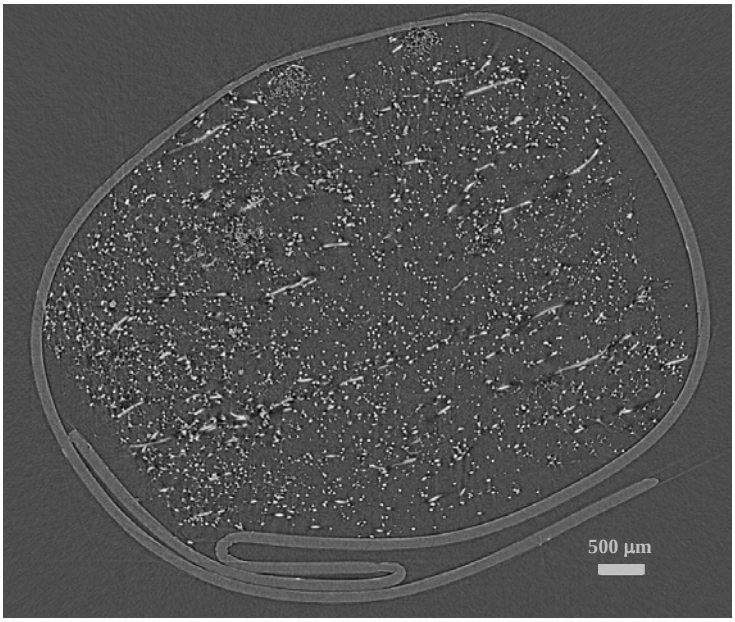

Figure 5.8 – A reconstructed slice of the felt sample.

Keeping similar the experimental condition (i.e. beam energy of 21 keV, pixel size of 4.5 µm), analogous spatial resolution is supposed to be achieved in the slices as for the previously described foam sample. The sample-to-detector distance D_{SD} was reduced to 9 cm in order to limit the excessive and deleterious phase contrast effect given by the thin felt fibres.

However, it is noticeable how the internal fibrous structure of felt is still undetectable by the simple bi-dimensional visualization of the single slice: the situation is completely different after that a complete three-dimensional volume is created by stacking the slices on a pile, as showed in Figure 5.9. The volume rendering has been performed by using the VGStudio package (Volume Graphics GmbH). In the latter case the intricate fibrous structure of felts is visible and the multiple crossing of the single fibers can be visualized. Although the tomographic analysis of fibrous materials is not so common in comparison to that one of the porous media, still some recent references can be found in connection with the study wood based composite materials (Lux, 2006) or bonded fibre networks (Tan et al., 2006). Some software tools have been developed as well, to characterize and study the fibrous materials (Yang and Lindquist, 2000; Eberhardt, 2002).

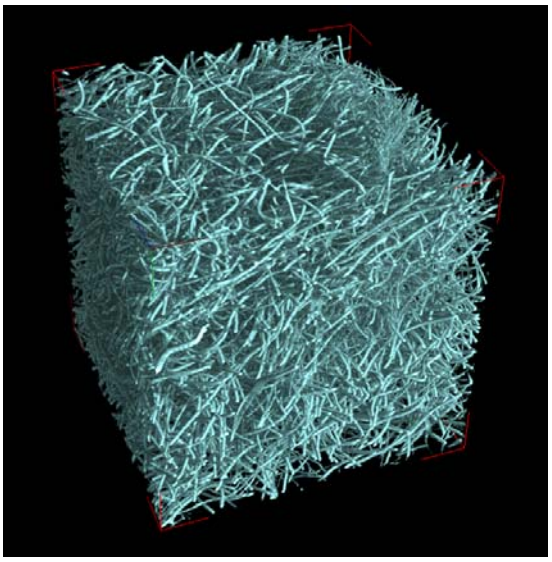

Figure 5.9 – A 3D rendering of the felt sample (300×300×300 pixels).

Both for the foam and the felt samples which were imaged at SYRMEP, a volume of 900×900×600 voxels was reconstructed: from each scan then several sub-volumes were selected for further visualization and image processing analysis.

To compare qualitatively the imaged samples a 3D visualization of the entire stack is possible, which is virtually inspected by views from different oriented planes. Particularly, the three orthogonal views of the VOI are considered in Figure 5.10 to evaluate the homogeneity of the samples (i.e., the presence or not of various density zones, or differently shaped/oriented pores, bubbles, fibres etc.): in the upper left image the ZX plane is showed, in the upper right the ZY plane is showed, as indicated in the bottom right image by the virtual sectioning of the volume done by the PORE3D program.

It is noticeable how the foam, even if explored along different planes, maintains very similar topology, appearing as a quite homogenous material, without any degree of anisotropy. On the contrary, in the case of the felt the anisotropy of the material becomes evident.

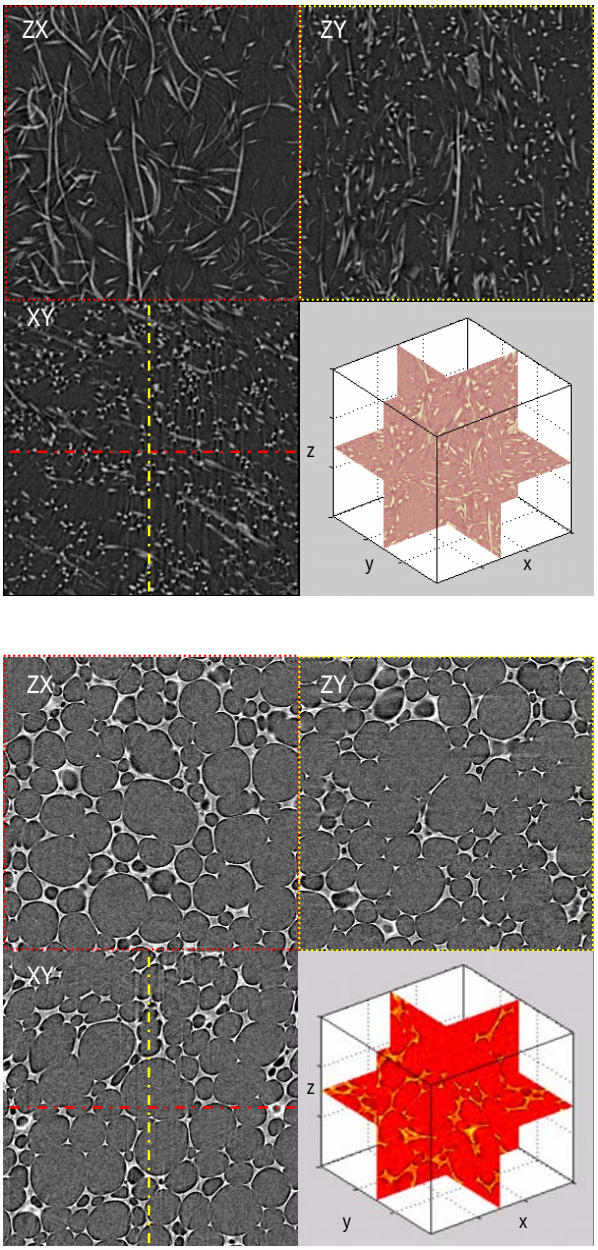

Figure 5.10 – A 3D volume of foam and felt samples virtually sectioned by orthogonal planes.

After the preparatory part above described, necessary to optimize the acquisition and the reconstruction parameters, a second series of different samples of around 7 mm in diameter were extracted out using a simple drilling tool (see Figure 5.11B) from the central part of the original mats. The obtained cylindrical form best fits the FOV of the detector and helps simplifying the reconstruction of the slices too. The new samples constitute a large dataset which is representative of the foam materials typically adopted in the automotive industry, spanning the extremes of the foam quality range, from the best to the worst in the acoustical sense. Tomography was conducted through the outer

surface of the foam to highlight again the cell structure in proximity of the material interface.

Scans were done both at the SYRMEP beamline and at the TOMOLAB station. At SYRMEP each scan consisted of 900 projections (images) covering an arc of 180° of rotation of the sample. In the vertical direction, each acquired image was about 4 mm high. More than 400 slices were reconstructed for each scan with a pixel size of 9 μm (binning 2×2 was adopted in order to speed up the acquisition and to limit the size of the reconstructed volume thus facilitating further manipulations). The beam energy was kept at 18 keV. Images were acquired with a sample-to-detector distance of 15 cm.

To increase the number of samples and to evaluate the potential differences, more than one core was extracted from the same foam mat and at least two zones for each core were imaged (e.g. top and bottom) in order to increase the statistic.

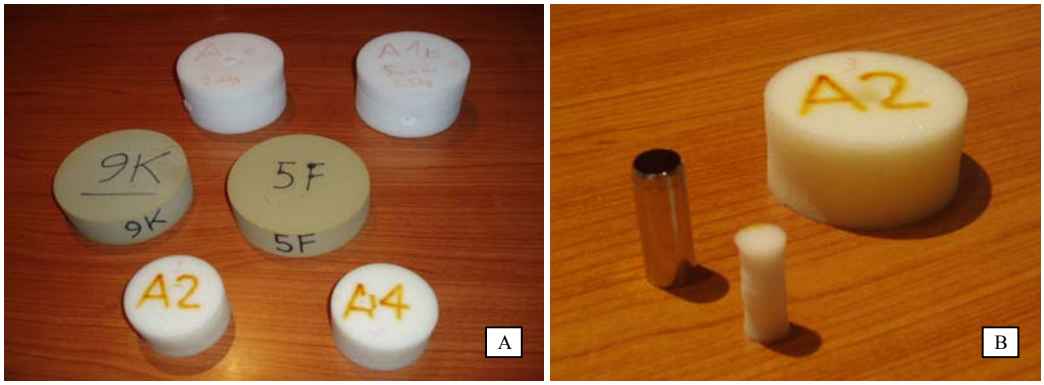

Figure 5.11 – Some of the investigated foam samples (A) and the cylindrical core sample extracted by the drilling tool (B).

At TOMOLAB an energy of 40 kV and 200 μA was used (middle focal spot mode), with magnification factors between 3.75× and 4.5×. Other specific information on the corresponding pixel size and sample-to-detector distance is furnished in Table 5.1. A complete nomenclature of the investigated samples is also reported together with a resume of the scanning parameters.

Sample Label	Foam Type	SYRMEP / TOMOLAB	Parameters
A2	polyurethane	S & T	E: 18keV, Px: 9μm, D_{sd}: 15cm / E: 40kV 200μA, M: 4.5× , Px: 5.5μm, D_{sd}: 31.5cm
A4	polyurethane	S	E: 18keV, Px: 9μm, D_{sd}: 15cm
A2b	melamine	T	E: 40kV 200μA, M: 4.5× , Px: 5.5μm, D_{sd}: 31.5cm
9K	most likely polyurethane	S	E: 18keV, Px: 9μm, D_{sd}: 15cm
5F	most likely polyurethane	S	E: 18keV, Px: 9μm, D_{sd}: 15cm
Gray1	most likely polyurethane	T	E: 40kV 200μA, M: 3.75× , Px: 6.6μm, D_{sd}: 24.75cm

Table 5.1 – Summary of the investigated foam samples: nomenclature and acquisition parameters.

Figure 5.12 gives an overview on the investigated foam samples, showing a selected ROI from one slice of each sample. As one can see, the polyurethane foam – i.e. the A2, A4 and Gray1 samples - is better reproduced, while melamine foam - i.e. the A2b sample – is absolutely unsatisfactory for further quantitative measurement. This seems caused by the relatively small bubbles (see the scale bar of slices for comparison) and thinner pore walls too, reasonably beyond the resolution limit of both the adopted imaging systems. The intermediate samples – i.e. 5F and 9K – reveal a microstructure which is a bit more complicated and characterized of smaller pore bubbles, but still clearly detectable.

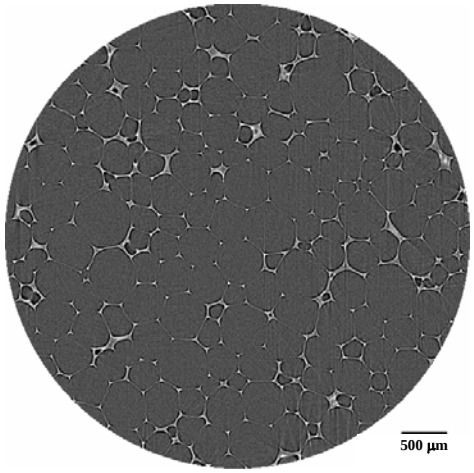

A2 – SYRMEP (Px: 9 μm)

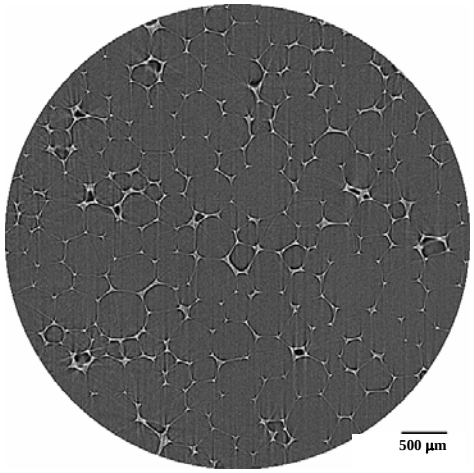

A4 – SYRMEP (Px: 9 μm)

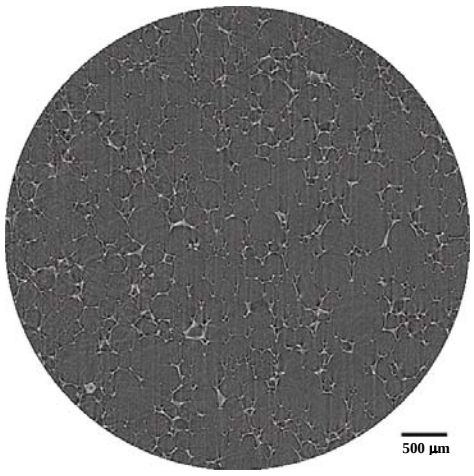

5F – SYRMEP (Px: 9 µm)

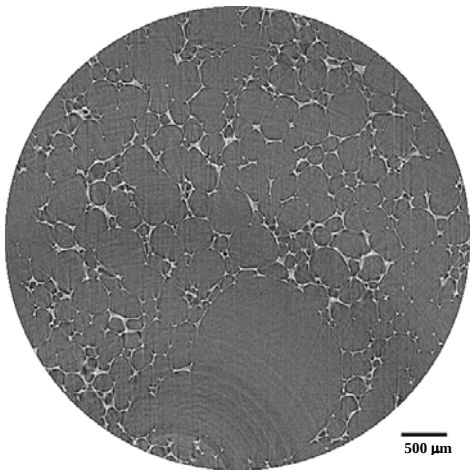

9K – SYRMEP (Px: 9 µm)

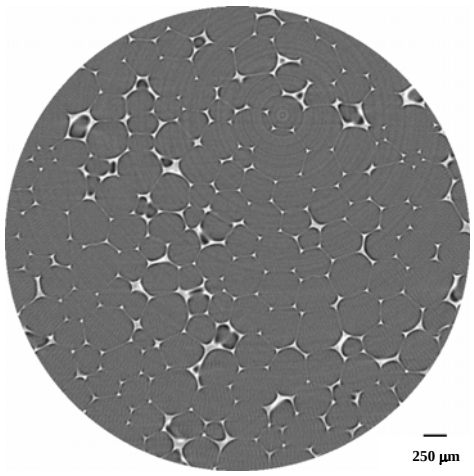

A2 – TOMOLAB (Px: 5.5 µm, M: 4.5×)

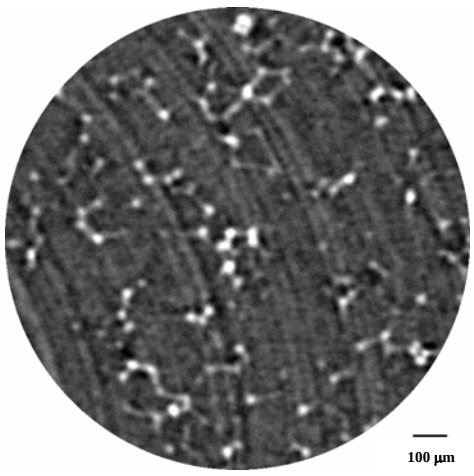

A2b – TOMOLAB (Px: 5.5 µm, M: 4.5×)

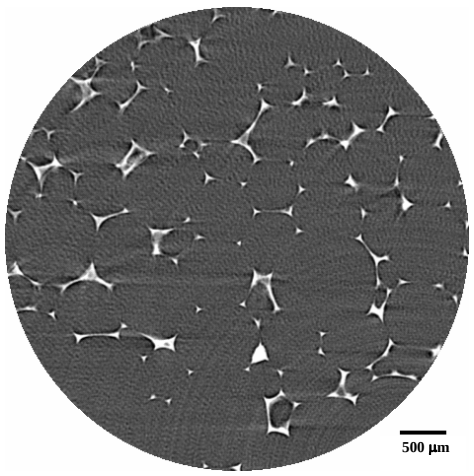

Gray1 – TOMOLAB (Px: 6.6 µm, M: 3.75×)

Figure 5.12 – Slices of the foam samples investigated at SYRMEP and TOMOLAB.

Figure 5.13 shows the 3D rendering of some VOI selected from each samples. This helps to understand the geometry of the three-dimensional internal micro-structure,

improving the visualization of the different pore shapes and providing the connectivity between the elements. The 3D visualization of the melamine foam A2b is not presented.

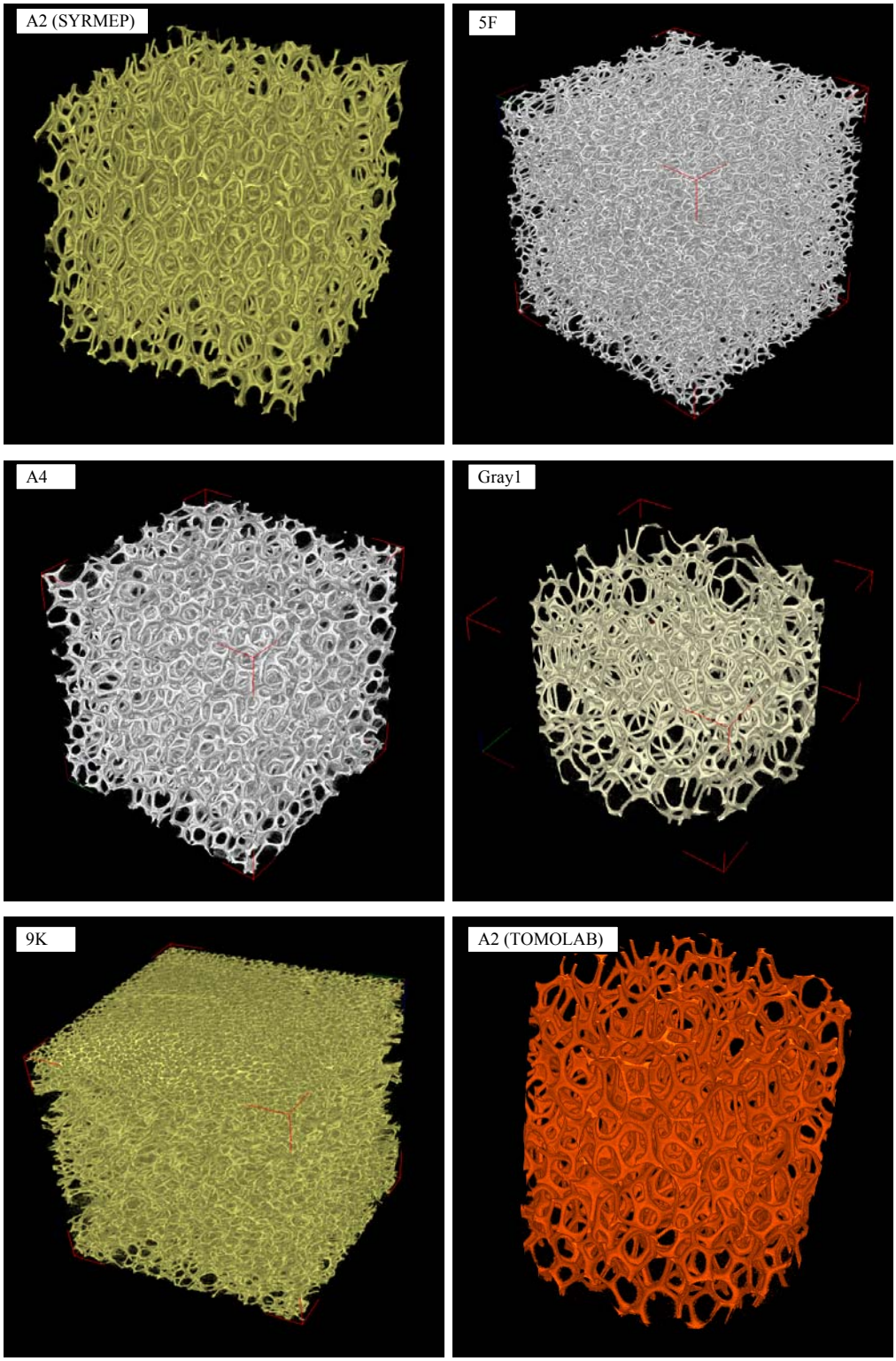

Figure 5.13 – 3D reconstructions of the investigated samples (the selected VOI are 300x300x300 pixels sized; refer to Table 5.1 for the pixel size of each sample).

5.1.3 Quantitative results

Once the volume is available, the datasets can be analysed with appropriate DIP tools: this paragraph collects the numerical results of the evaluation of the geometrical and morphological properties of the different samples.

Basically, the results include porosity (i.e. the ratio of void to total voxels), the thermal characteristic length, defined as the ratio between the volume and surface voxels of the void phase, and the tortuosity, defined as the ratio of the actual path length through the pores to the Euclidean distance.

As previously mentioned, several cores were extracted from the same samples and different parts were imaged. Furthermore for each sample, different sub-volumes (REV) were considered for statistical reasons. Properties evaluations were carried out along the three orthogonal directions (i.e. not only slice by slice in the Z direction, but also in the XZ and YZ planes), even if not significant differences are expected.

The REV can be defined in different ways as function of the quantity that has to be measured (e.g. the porosity, the permeability). In this specific case, the porosity will be used as indicator to determine the REV size.

To determine the REV a recursive process is foreseen: starting form the central voxel of the reconstructed volume, a cube of fixed dimensions is considered. The porosity is evaluated, than the size of the cube is increased. Again the porosity is calculated and so on till the largest permitted cube is reached. The REV size is finally assumed as the size of the cube that corresponds to a stabilization of the porosity value (see Figure 5.14). On the base of this consideration a 300 voxel REV was defined.

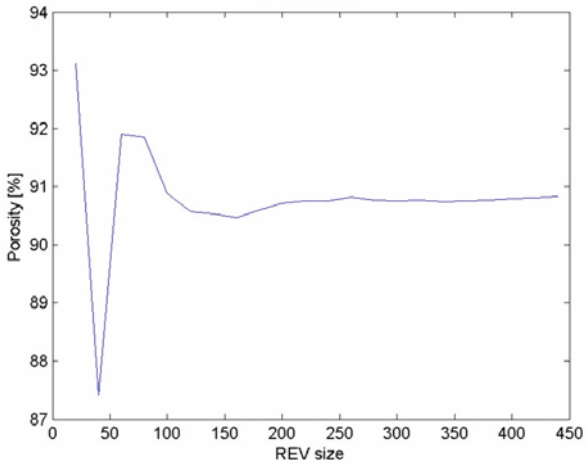

Figure 5.14 –The REV analysis carried out for the A4 foam.

Different digital filters were applied on the grayscale slices, in order to improve the image quality and reduce random noise, spurious features and other artefacts due to the acquisition and reconstruction process. One should carefully manage spatial filters as they can alter real data. Special care should be used to avoid removing small and thin structures, like the extreme points of the cells wall. For our case both the Median filter and the Gaussian one were successfully applied. The 3D median filter was exploited directly on the entire volume, using a convolution kernel with a radius of one pixel (i.e. a 3×3×3 cubic mask).

Segmentation is the process used to convert the original grayscale image to a binary one (i.e. containing only zeros to represent the void phase and ones to represent the solid phase). This represents the first heavy modification in the DIP before any further analysis, and can be considered as a key step to evaluate the porosity, as well as many other geometrical and morphological parameters on porous materials. The basic concept lies in the proper selection of a threshold value on the intensities histogram of a grayscale image. Once this threshold value is identified, voxels are assigned to one of the two classes representing the void or solid phases according their value if lower or higher than the selected threshold.

The histogram showed on Figure 5.15 shows the typical bi-modal distribution of grayscale levels of a bi-phases system. The smaller peak on the right corresponds to the solid phase while the bigger one in the centre of the figure is associated to the void bubbles. On the left a very small peak appears: this is due to the phase contrast effect that comes from synchrotron coherent beam and enhances the contrast at the solid/void interfaces of slightly adsorbing material (like foams are).

We tested and compared different segmentation procedures on our dataset. Although the more sophisticated methods can be of some advantage for the more elaborate cases (for example in multi phases mix), the Otsu's method delivers reasonable results both in terms of computational time and lack of numerical artifacts. However, after segmentation usually a cleaning procedure is preferable in order to remove those isolated void voxel that are unphysical (i.e. produced by the segmentation) and the solids particles eventually suspended into the void phase, which are also unphysical. Such a cleaning procedure is basically performed according a size criterion removing particles and objects whose volume is below a predefined value.

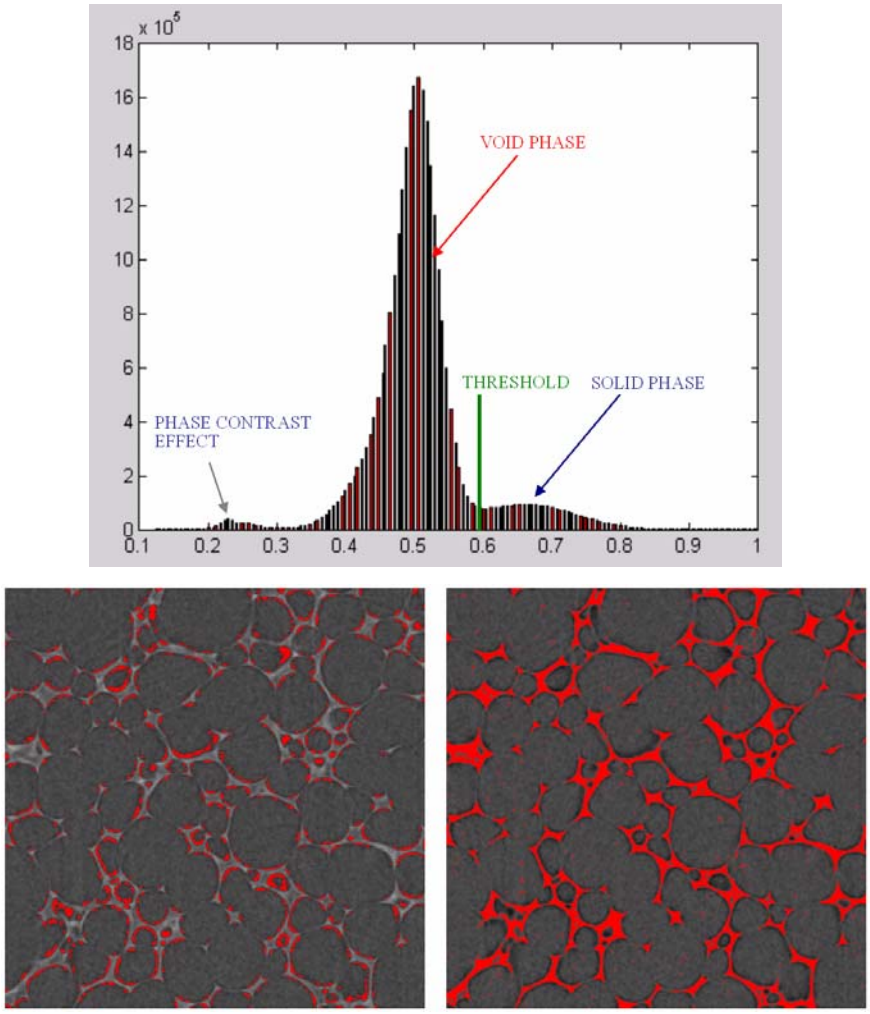

Figure 5.15 – Grayscale intensities histogram of the foam volume (sample A4).

If one is interested into the effective porosity, the closed voids should be removed (i.e. pores or bubbles not connected to the border of the REV). Since each slice has its own grayscale set, a preparatory equalization step is first needed before operating with the volume histogram.

Once we get the binary image after segmentation, the porosity ϕ of the sample is immediately estimated as:

$$\phi = \frac{\#\ voxels \in void\ \ phase}{X \cdot Y \cdot Z} \qquad [5.1]$$

where X, Y and Z are the cube dimensions in pixels.

Porosity values were calculated as mean values on a wide set of 300×300×300 cubic samples. Also the degree of anisotropy can be evaluated, just considering ϕ along different directions. As an example, ϕ profile is given in Figure 5.16 (i.e. ϕ evaluated

on single 2D slices, in order to give an idea of the homogeneity inside the sample) along the Z-axis. Since only the 3D-disconnetted bubbles were removed, the total ϕ exactly matches the effective one (i.e. there are no isolated bubbles into the samples). This sounds reasonable considering the very high porosity and connectivity of such kind of porous medium.

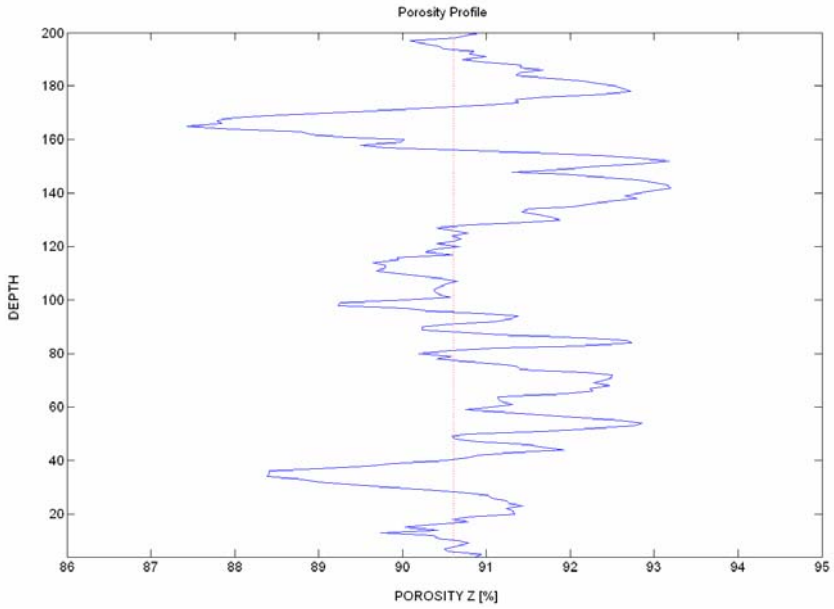

Figure 5.16 – Different segmenting techniques applied to the same ROI of the foam (sample A4).

The thermal characteristic length (Λ') is a purely geometrical parameter used in Biot's model to define the energy dissipation related to thermal exchanges between the solid phase and the fluid one in a porous material. Roughly speaking, the thermal characteristic length can be related to the pore size distribution of a medium. The mathematical definition for Λ' is:

$$\frac{2}{\Lambda'} = \frac{\int_S dS}{\int_V dV} \qquad \left[\frac{1}{m}\right] \qquad [5.2]$$

Thus, it is essentially calculated evaluating the volume to surface ratio of the pores (bubbles) inside the material or the selected REV. The digital process employed to get the volume to surface ratio considers a single slice. After segmentation, on the binary image is very simple to calculate the total area A of the sectioned bubbles, just counting the number of white voxel in the slice. A new binary image is created (see Figure 5.17) on which only the edges of the internal features (pores) are preserved; the

applied method takes an intensity image *I* as its input, and returns a binary image *B* of the same size, with 1's where the function finds edges in *I* and 0's elsewhere. The method returns edges at those points where the gradient of *I* is maximum. So, the total perimeter P of the cross-sections of the bubbles is calculated again just counting the white voxel in the slice.

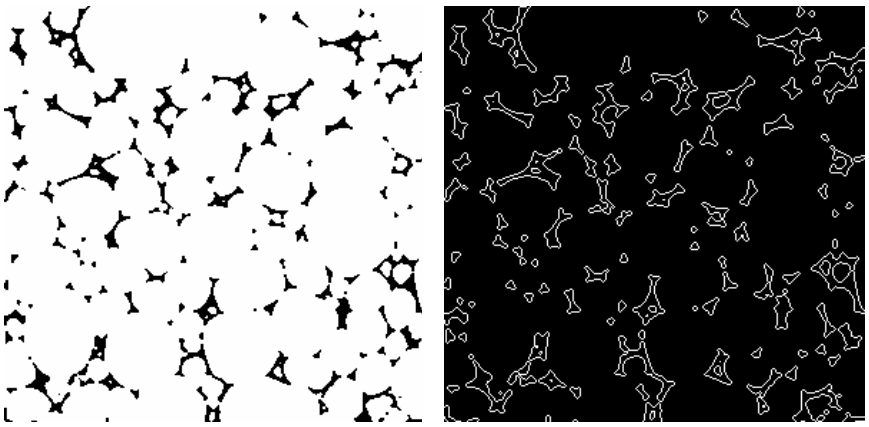

Figure 5.17 – Edge extraction for the calculation of Λ' (sample A4).

One can naturally extend the bi-dimensional concepts to three-dimensional ones: just summing the cross-sectional areas of the slices the total pore volume is obtained, while summing the cross-sectional perimeters the surface of the pores can be approximated.

By formula, it can be written:

$$\sum_i^N P_i = S \qquad \sum_i^N A_i = V \qquad [5.3]$$

where N is the number of slices, S the total wall surface and V the total pore volume.

Finally, the thermal characteristic length can be obtained as:

$$\Lambda' = \frac{2V}{S} \quad [m] \qquad [5.4]$$

To investigate the directionality effect and to evaluate the degree of anisotropy of the medium respect to this parameter, the procedure was repeated considering the other two directions. Finally, for each subset considered, Λ' was also calculated as:

$$\Lambda' = mean\left(\frac{2A_i}{P_i}\right) \qquad [5.5]$$

The approach is conceptually identical but practically a little bit different so can lead to small differences of the values.

Tortuosity τ is another very important geometrical parameter to characterize our foam samples; particularly, it can be related to the fluid flow properties, i.e. the

permeability (Montminy, 2004) and to the capability to transmit acoustical waves inside the pore space of the medium. The complexity of the three-dimensional pores structure, due to the high connectivity of the bubbles, is self evident from the reconstructed CT images. Tortuosity can be defined as the ratio of the effective (or actual) path length ℓ that one has to walk through the pore space from a given starting point to an end one, to the Euclidean distance *d* between the same starting and end points:

$$\tau = \frac{\ell_{effective}}{d_{Euclidean}} \qquad [5.6]$$

Since feature extraction from 3D segmented images is a computationally heavy task, we calculate the skeleton which represents the object in lower dimension while strictly preserving its topology. For an object in continuum space, the medial axis (i.e. the skeleton, when centered with respect to the pore space boundaries) is the union of one-dimensional curve segments. The skeleton network of paths and nodes retains important information about the connectivity and the percolation properties of the samples.

The 3DMA program was used because to treat large samples of 400×400×400 voxels (see Figure 5.18).

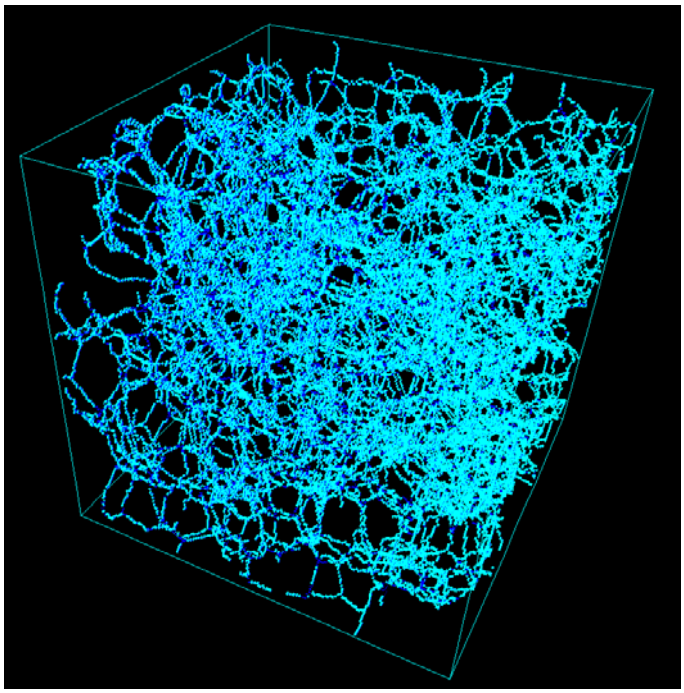

Figure 5.18 – The skeleton of the A4 sample is showed (obtained by 3DMA). A color map is used for medial axis proportional to the distances, from blue (far away) to green (closest to grain border): blue voxels are located on the center of the largest bubbles; green voxels represent the terminal part of a blind path.

The statistical values of the geometrical parameters obtained form DIP on the foam samples described in the previous sections are statistically summarized in Table 5.1.

The porosity ϕ values generally underestimate the value measured via traditional laboratory test (e.g. Hg porosimetry) for all the samples, with an almost constant error of about two percent points. This is reasonably due to the presence of noise or artifacts and to the intrinsic limitations of the set-up used; this could make difficult an accurate segmentation of the thinner structures. However, a kind of calibration seems possible due to the constant deviation from the real value showed by the samples.

The thermal characteristic length Λ' is of the same order of the experimental value and this can be assumed as a good result, also considering the resolution limit of the acquired images, which reasonably cannot reveal structures smaller than few micrometers. Furthermore, the calculated values allow a sorting of the different foams.

	A2				A4			
	ϕ [%]		Λ' [µm]		ϕ [%]		Λ' [µm]	
sample #	SYRMEP	TOMOLAB	SYRMEP	TOMOLAB	SYRMEP	TOMOLAB	SYRMEP	TOMOLAB
A	94,19	94,4	450	510	94,14		415	
B	94,26	94,41	452	509	94		400	
C	94,22	94,48	449	520	93,85		405	
D	94,13		440		94,07		423	
E	93,84		416		93,75		399	
F	93,87		413		93,97		402	
G	93,79		408					
H	93,94		421					
mean	**94,03**	**94,43**	**431**	**513**	**93,96**		**407**	
std. dev.	0,19	0,04	18,46	6,08	0,14		9,61	

	5F				9K				Gray1			
	ϕ [%]		Λ' [µm]		ϕ [%]		Λ' [µm]		ϕ [%]		Λ' [µm]	
sample #	SYRMEP	TOMOLAB	SYRMEP	TOMOLAB	SYRMEP	TOMOLAB	SYRMEP	TOMOLAB	SYRMEP	TOMOLAB	SYRMEP	TOMOLAB
A	91,92		270		88,56		176			96,49		935
B	90,94		240		88,9		200			96,44		945
C	91,15		267		88,22		173			96,3		880
D	90,64		235							96,48		950
E	89,85		210									
F	91,05		244									
mean	**90,93**		**244**		**88,56**		**183**			**96,43**		**928**
std. dev.	0,68		22,17		0,34		14,80			0,09		32,27

Table 5.2 – Quantitative results on REV selected from the investigated foam samples: porosity ϕ and thermal characteristic length Λ' are reported, together with their mean value for each sample and the standard deviation.

	PU foam - SYRMEP		
	ϕ [%]	Λ' [µm]	τ
Min	88,11	125,58	0,96
Max	91,3	230,65	1,78
Mean	90,3	190,73	1,22
Median	90,4	202,45	1,07
Std. Dev.	0,87	30,99	0,36
Experimental	**92,2**	**161**	**1,65**

Table 5.3 – Statistical comparison between the numerical results on standard polyurethane foam calculated via DIP (12 REV of 300×300×300 voxels were considered) and via laboratory tests: porosity ϕ, thermal characteristic length Λ' and tortuosity τ are showed.

In Table 5.3, to give an idea of robustness of the DIP approach, we better compare the calculated values for ϕ, Λ' and τ with that ones measured via laboratory tests. The considered foam sample is the standard polyurethane foam we showed in Figure 5.5: 12 REV were considered to obtain the quantitative results.

5.1.4 Conclusions

The results showed in the present paragraph proved clearly enough the potentials and the capabilities of X-ray μ-CT to discern and define the structures and the geometrical features of polyurethane foam samples. These qualitative examples show that the cellular structure is complex: the images obtained constitute a good database for the development of clear and robust image-processing algorithms for the evaluation of geometrical and morphological parameters.

The image quality of the reconstructed slices was optimized tuning the scan parameters to attain the best combination between the investigated materials and the characteristics of the available equipment at the SYRMEP beamline as well as at the TOMOLAB facility.

The developed activities represent a first step towards the creation of a bridge between the micro-analysis of the porous materials structure, the macroscopic models that are currently used for modeling them and their macroscopic acoustic performances. Such a bridge is necessary to be able, in the near future, to properly drive the design of the chemistry of porous materials on the basis of pre-defined acoustic targets.

We demonstrated that μ-CT coupled with intensive digital image processing can be considered as a valid complemental - or even substitutive - approach to obtain the measurement of those parameters of purely geometrical nature, which are traditionally derived via time-consuming and delicate laboratory tests. The proposed method indicates a work-flow, from the image acquisition to the geomorphologic characterization of the porous materials, which can be practically applied to control the design and production of such materials used in the automotive industry, useful to properly address the process parameters towards their optimization.

At the same time a deeper investigation of the material behaviour under stressed or normal operative conditions seems recommendable, which could lead to the numerical modeling of those materials via, for example, finite element or lattice Boltzmann simulations.

5.2 An imaging based innovative approach for the characterization of the resonance wood

In the last years several musicians, scientists and musical instruments makers deal with the understanding of microscopic properties of different woods in order to realize, for example, piano soundboards. The knowledge in this field is both from scientific approaches and from empirical methods. Many studies were carried out to determine the mechanical and micro-structural wood properties in order to link them to the resonance macro-behaviour and therefore to obtain measurable quantities (Horcin and Gubriansky, 2005; Berthaut et al., 2003, Suzuki and Nakamura, 1990).

Nowadays, for example, it is well known that spruce Young modulus for the violin upper plate and that one of the maple lower plate must be of a precise value (Hutchins, 1995). There are nevertheless other parameters and variables which characterize and influence the resonance wood quality, such as the climatic stands, the humidity content (Fromm et al., 2001), the temperature fluctuations and the type of seasoning.

In this paragraph a new scientific approach for the characterization of the resonance wood is described. In order to investigate the wood microstructure an intensive imaging work has been done using μ-CT coupled with Scanning Electron Microscopy (SEM). Wood microstructure affects the acoustic macro-behaviour of this material: the proposed method allows the evaluation of the acoustic qualities of the different resonance woods mainly basing on the geometrical and morphological characterisation of the wood microstructure. We used information obtained by robust image processing analysis to feed a Finite Element Method (FEM) model for further acoustic simulations. The method leads to an objective sort between the high quality resonance wood and the worse one. The aim of this study is to evidence the importance of resonance wood microstructure as acoustic agent for the macro-behaviour of this material.

5.2.1 Imaging work

Non-invasive μ-CT was used to reconstruct the three-dimensional inner wood structure, combined with SEM in order to get bi-dimensional very high resolution images to use as a benchmark.

The spatial resolution of few micrometers nowadays easily achievable using both synchrotron light or micro-focus X-ray source, is adequate to reveal the wood microstructure (Fioravanti and Ricci, 1991; Illman and Dowd, 1999; Stepp et al., 2004).

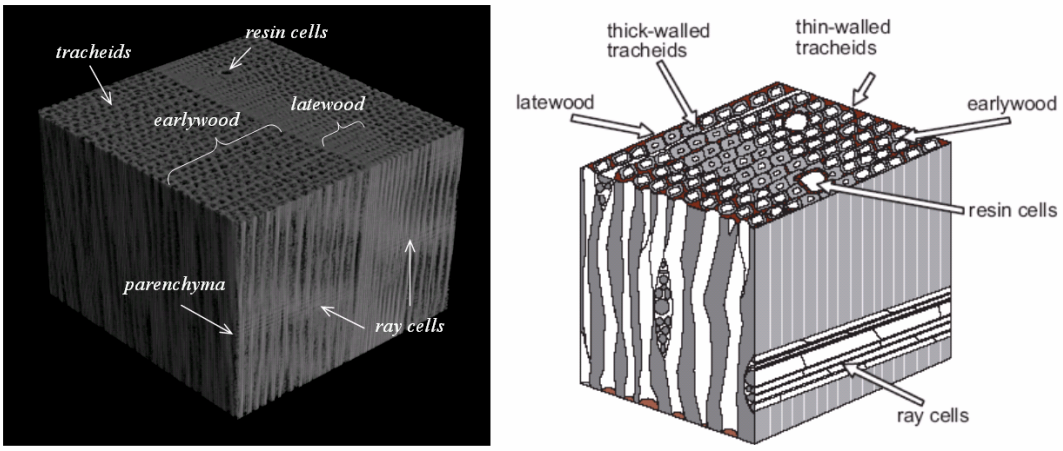

Figure 5.19 – A 3D visualization of the spruce wood reconstructed by μ-CT (left): tangential, radial and longitudinal virtual cross-sections are showed. A sketch illustrating the main anatomic features of softwoods is also showed (right).

To what it concerns the present study, μ-CT was performed both at the SYRMEP beamline and at the TOMOLAB facility. Three samples of spruce wood form different coming were investigated, namely two samples of Abies Picea Excelsa from the Val di Fiemme (Italy) and the Tarvisio Forest (Italy) and one sample of Picea Sitchensis from the west coast of Canada.

Later, two samples of spruce coming from Val di Fiemme were observed, representing the best to the worst wood quality the acoustic sense. In the following, we refer to these samples as high (H) and low (L) quality.

Different parallelepipeds with a square cross-section of around 5 (radial) x 5 (tangential) mm were extracted from the central part of three spruce boards (see Figure 5.20). In the longitudinal direction the sample length was approximately 25 mm.

In order to keep the most constant value of moisture content the specimens were enveloped with Parafilm during the tomographic scan.

Figure 5.20 – Samples cut out from the original wood board.

At SYRMEP a set of 900 projections were collected for each scan with beam energy of 18 keV and a sample-to-detector distance of 10 cm, in order to reconstruct 800 slices corresponding to a sample height of 3.6 mm. The adopted pixel size was of 4.5×4.5 μm.

At TOMOLAB planar images were recorded with an energy of 40 kV and 200 μA, a magnification factor of 5× that, coupled with a binning 2×2 (horizontal × vertical) of the CCD, finally yielded a voxel size of 5 μm. Figure 5.21 presents a comparative evaluation of the achievable results with both the facilities, which qualitatively shows that the achievable spatial resolution is almost comparable.

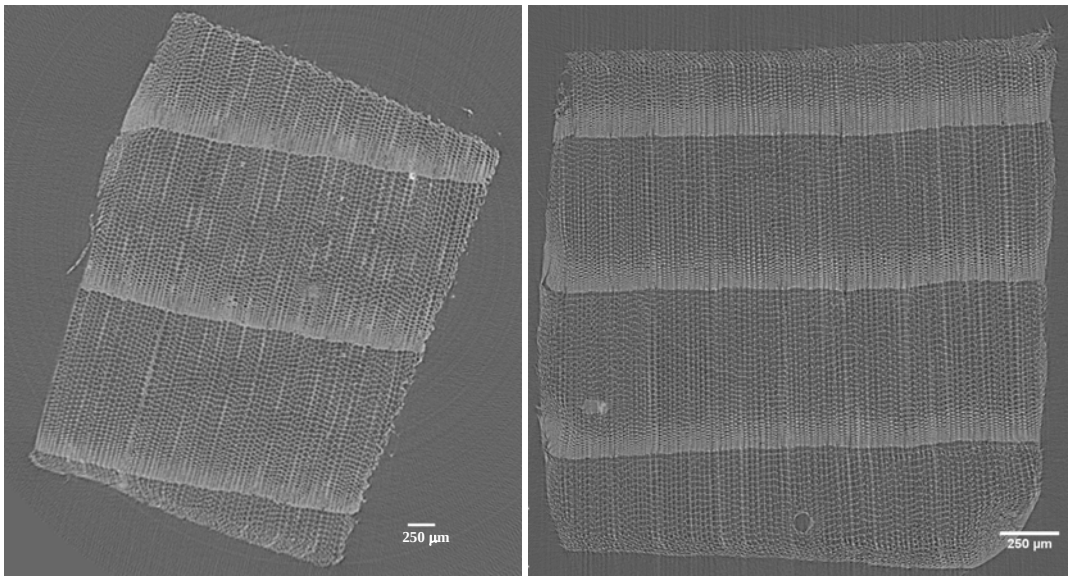

Figure 5.21 – A qualitative comparison between the same spruce wood imaged at SYRMEP and at TOMOLAB (experimental conditions are reported in the text).

The second and complementary investigation adopted to characterize the inner resonance wood microstructure was the SEM analysis. Usually, the time-consuming and delicate procedures required to obtain cross-sections of wood samples by microtomy risk to damage the sample during the cutting, altering the investigable structures. This makes the use of SEM non convenient to collect huge amounts of data in a short time. However, SEM seems necessary in order to have a brighter insight of the microstructure itself, inspecting topographies of specimen at very high magnifications (even more than 1˙000˙000 ×) thus allowing to achieve a sub-micrometric spatial resolution on the obtained bi-dimensional images.

The equipment used was a Leica scanning electron microscopy Stereoscan 430i with Oxford Link X-rays microanalysis, available at the laboratories of the University of Trieste. All the specimens, as they are organic and therefore non conductive, needed to

be in advance metallized and polished. Again, the different comings and qualities of spruce wood were examined as previously described.

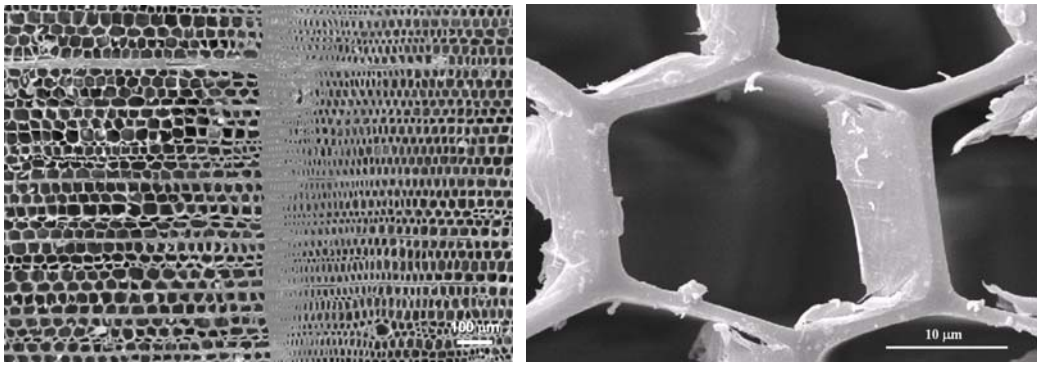

Figure 5.22 – The microstructure of spruce wood (H sample) imaged by SEM at 100 x (left) and the particular of a cell in the same sample (right). It is noticeable that part of the cell structure was a bit altered during the sample preparation. Images appear three-dimensional just because of the large depth of field and the shadow relief effect of secondary and backscattered electrons.

Growth in trees is affected by soil and environmental site-specific conditions: normally, a single growth ring will have low and high density regions which correspond to fast and slow growth rates respectively. Earlywood is referred to as the lighter portion having large wood cell lumens and thin cell walls. In contrast, latewood grows slower and appears as the darker portion of the ring with the smaller lumens and thicker cell walls. The regularity of these alternating zones, together with the general homogeneity of the cells diameter and wall thickness, are one of the necessary requirements to make a spruce wood suitable for making musical instruments and components.

Figure 5.23 reports the reconstructed slices (pixel size of 4.5 µm) of samples from different comings. From the slices a ROI can be extracted to better visualize the cells. The ray cells are visible as the short white segments spread all over the slices, always oriented orthogonally to the growth rings: just a piece of each ray is intersected by the slice, as the ray slopes deeper towards the next slices. In the slice on the left, vanishing ring artefacts are perceptible, superimposed to the wood microstructure.

The X-ray absorption of wood is related to the relative weight of its chemical element, i.e. carbon, oxygen and hydrogen. Furthermore the percentage of water given by the moisture content of the wood will influence the X-ray absorption, as well as the eventual – and rare – presence of heavier elements tracks.

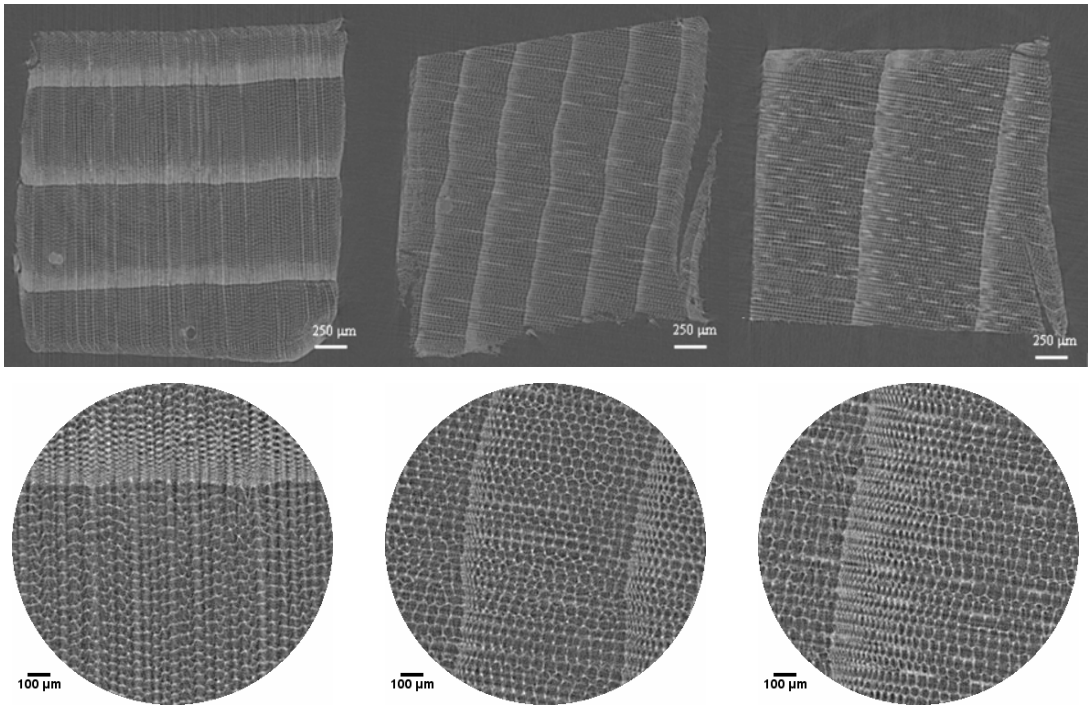

Figure 5.23 – Reconstructed grayscale slices from the Val di Fiemme spruce wood (left), the Tarvisio one (middle) and from Canada (right). Images were acquired at the SYRMEP beamline with a pixel size of 4.5 µm. The corresponding circular ROI are showed below.

There are three mainly polymeric constituents of the wood: cellulose, hemi-cellulose and lignin. Cellulose ($C_6H_{10}O_5$) is a linear, semi-crystalline glucose polymer. Hemi-cellulose ($C_{5\text{-}6}H_{11\text{-}12}O_{5\text{-}6}$) is a branched amorphous, hetero-polysaccharide. Lignin ($C_{10}H_{13}O_2$) is a networked amorphous phenol-propane polymer. All these polymers are hydroscopic as they lodge hydroxyl and other oxygen-containing groups that attract moisture. The mass percentage of each polymer in dry wood is about 45-50% cellulose, 20-35% hemi-cellulose and 20-30% lignin, which can vary widely depending upon the trees species. In addition to the three constituents above mentioned there may be 0-10% of non-structural organic materials in wood: these materials, called extractives, include a diverse collection of compounds such as tannins, terpenoids, waxes, and gum starch.

Wood is typically an orthotropic material as its mechanical, vibrational and acoustical properties vary along three mutually perpendicular axes (i.e. longitudinal, which is parallel to the fiber orientation, radial and tangential which are respectively normal and tangent to the growth rings). The major differences are between the radial or tangential axis and the longitudinal one. Obviously, also transmission and attenuation of sounds are different for longitudinal, radial, and tangential directions. In Figure 5.24 a

VOI was created from the selected ROI on the slices, and virtually inspected along the three orthogonal directions above mentioned. The main anatomic features of the (spruce) softwood are detectable, i.e. tracheids, latewood, earlywood, resin ducts, parenchyma cells, etc.

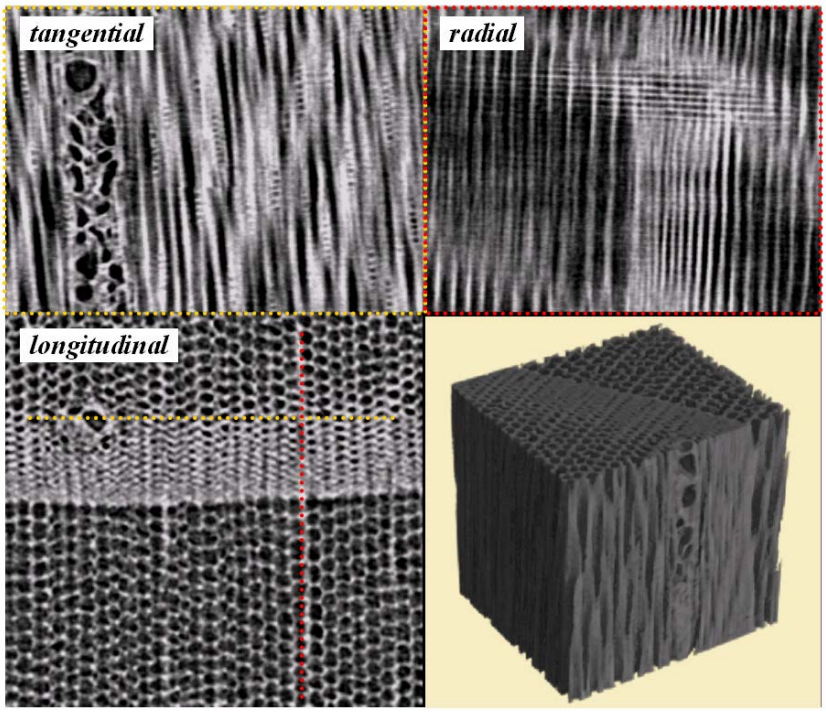

Figure 5.24 – A 3D virtual inspection of a VOI (voxel size is 4.5 μm) selected from the reconstructed sample (Val di Fiemme). A 3D rendering of the whole VOI is showed on the bottom right. Volume faces are not oriented according to the longitudinal, radial and tangential directions.

5.2.2 Quantitative measurements

The volumes reconstructed via μ-CT were further analyzed by mean of intensive DIP applying home-built functions and routines implemented under the Matlab® environment (Matlab Imaging Toolbox 6.5.1) in order to extract geometrical and morphological information on the investigated samples from a three-dimensional statistically relevant amount of data.

A REV was chosen large enough in order to include all the representative features of interest: generally, a cubic sub-volume of 350×350×350 pixels (corresponding to a cube size of 2.46 mm^3 for the SYRMEP datasets) is considered adequate.

To evaluate the porosity, as well as many other geo-morphological parameters, it is again necessary to operate on a binary image, i.e. an image containing only zeros to represent the void phase and ones to represent the solid phase. Once the threshold is

identified on the intensities histogram of the slices, any voxel is assigned to one of the two classes, according its value, if lower or higher than the threshold itself.

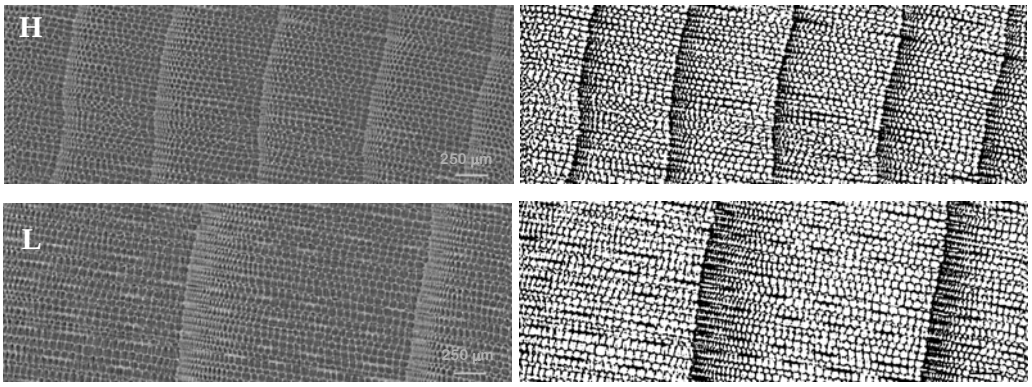

Figure 5.25 Original (left) and thresholded (right) wood microstructure of a ROI selected from the spruce images. High and Low quality samples are presented coming from the Val di Fiemme.

Intensive semi-automatic procedures can be applied to obtain quantitative morphological information on the thresholded wood microstructure (Steppe et al., 2004). Porosity ϕ can be evaluated as the ratio of the voids to the total pixels. The mean value on the considered REV can be calculated, via recursive calculation on single slices forming the volume: a porosity profile along the longitudinal axes can be visualized to evaluate the deviation from the mean value (see Figure 5.26).

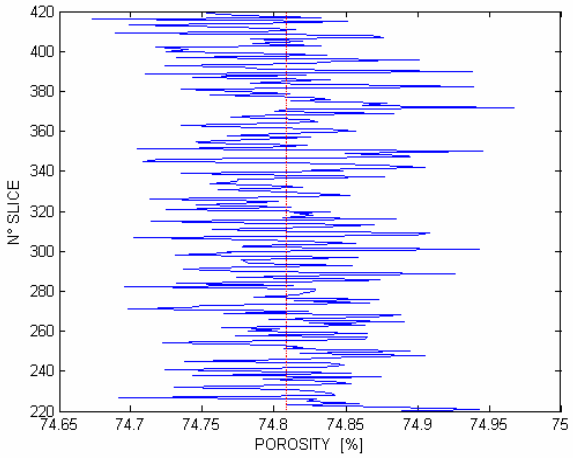

Figure 5.26 – The porosity ϕ is evaluated slice by slice along the longitudinal direction (Val di Fiemme, H sample). The mean value is represented by the red dotted line.

The cells diameter D as well as the walls thickness w can be estimated on a statistical basis calculating the two-point correlation function slice by slice (Al Raoush and Wilson, 2005) as showed by Figure 5.27. As expected, the cell size results very

different form the latewood and the earlywood. However, the achieved spatial resolution makes very hard measuring accurately the cell size of the latewood as often the cells cannot be clearly distinguished to each other. The two-point correlation function is strictly related to the porosity, the specific surface area and to the object's diameter as discussed in the previous chapter.

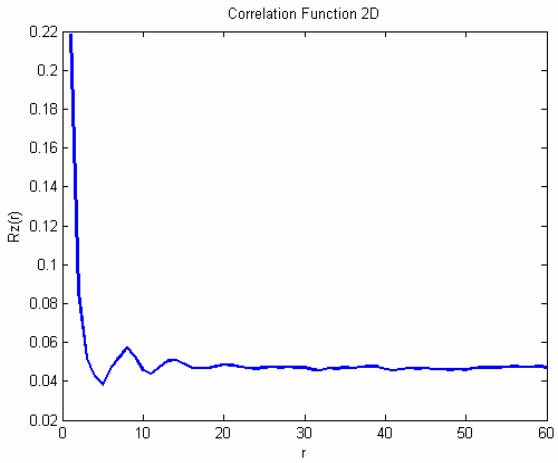

Figure 5.27 – The two-point correlation function (Val di Fiemme, H sample) is strictly related to the porosity, the specific surface area and to the cells diameter. Latewood and earlywood should be separately considered. The lag distance r is expressed in terms of the pixel size (4.5 μm).

Another approach that was considered involved the direct measurements of the cell diameters D and the wall thickness w via a semi-automatic procedure on the slices. As illustrated in Figure 5.28 on the sample H coming from the Val di Fiemme, we evaluated a line profile on a selected ROI: it should comprehend an earlywood homogenous zone included into a single growth ring: this will avoid confusion with values coming from the smaller cells of the latewood (which cannot be precisely measured due to the lack of resolution).

We elaborated information collected from the closer and rarer peaks of several line profiles to estimate both the mean cell size and the mean wall thickness for earlywood.

While such a profile should be preferably obtained on the grayscale image (to preserve all the information content of the original image which can make the measure more accurate), it is then possible to operate also on the segmented ROI in order to separate each wood cell. In Figure 5.28 an example is given of single cells identification by mean of a rainbow colour scale.

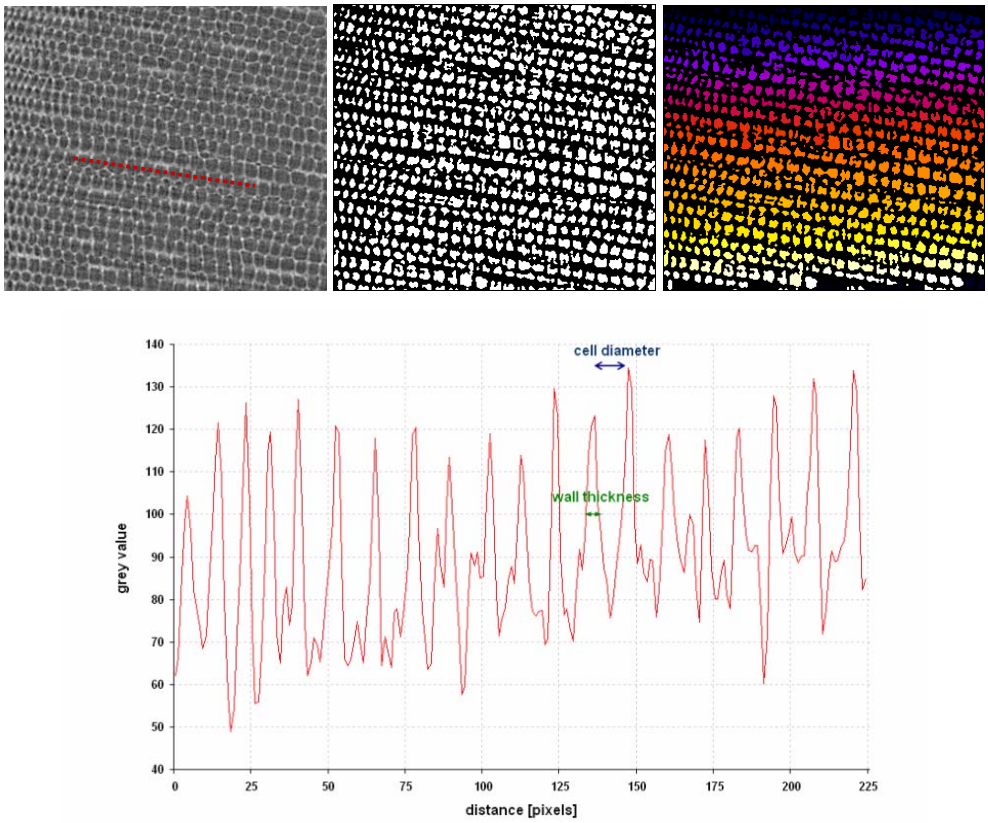

Figure 5.28 – A method is illustrated to measure, from the closer and rarer peaks on the line profile (red line in the original grayscale image on the top left), the mean cell size and the mean wall thickness for earlywood. Also, operating on the segmented image (middle top), object separation on labeling (top right) can be adopted to obtain areal or length measurements on the single wood cells.

The morphological measures can be evaluated on a statistical base considering a significant number of lines and ROI: in Figure 5.29 we report, for instance, the distribution of the cell diameter for the same sample.

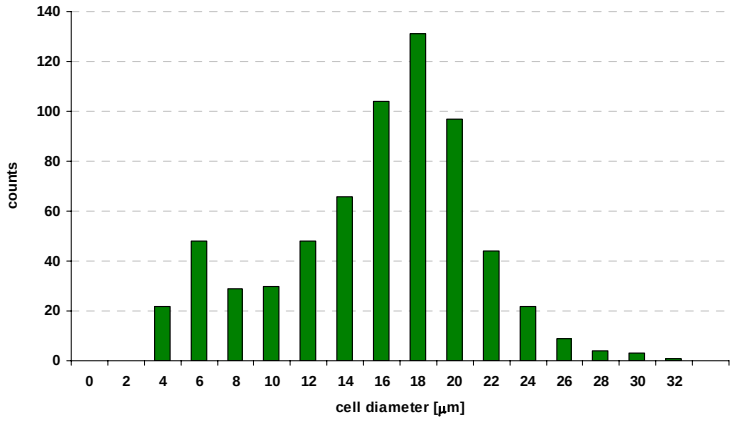

Figure 5.29 – The (log normal) distribution of the cell diameters plotted for the H sample.

The two methods both revealed a good agreement, especially for the cell diameter.

In Table 5.4 we provide a summary of the mean values measured via DIP on the μ-CT slices of the spruce samples from the different comings. It is noticeable how the Canada spruce reveals a lower porosity if compared with the others, while it seems quite difficult establish a significant difference concerning the diameter of the earlywood cells for the three samples. To whom it regards the latewood, one should be aware that the measurements are not completely reliable due to the poor information we can recover from the μ-CT data. However, we use the SEM images as a benchmark to approximately confirm the presented values.

	Val di Fiemme		Tarvisio		Canada	
	earlywood	latewood	earlywood	latewood	earlywood	latewood
ϕ [%]	71,5	75,7	70,3	74,8	62,5	68,8
D [μm]	19,7	11,2	21,4	16,5	18,2	15,6
w [μm]	4,3	2,4	4,1	2,5	4,6	1,6

Table 5.4 – Quantitative results for porosity, cell diameter and wall thickness on the sample of different comings (mean values are showed on a significant amount of selected VOI).

In Table 5.5 instead a summary is given of the same geometrical parameters evaluated on the high and low quality samples from the Val di Fiemme. The porosity value found for the H sample is a bit lower respect to the L one. Even if again the values of cells diameter and wall thickness are quite similar, it's worth noticing how the 5th and 95th percentiles reveal the higher dispersion of the measured values in the case of the low quality sample. This reasonably indicates a coarser degree of homogeneity inside the sample microstructure, which could in some way be reflected into the acoustical response of that wood.

	H *sample*					
	earlywood			latewood		
	percentile		mean	percentile		mean
	5%	95%		5%	95%	
ϕ [%]	58	63	60,20	65	72	68,60
D [μm]	18	21	19,40	9	13	10,50
w [μm]	3	5	4,45	1	2	1,89

	L *sample*					
	earlywood			latewood		
	percentile		mean	percentile		mean
	5%	95%		5%	95%	
ϕ [%]	56	61	58,56	65	77	71,40
D [μm]	15	25	16,78	8	14	12,60
w [μm]	3	5	4,30	1	2	1,92

Table 5.5 – Quantitative results for porosity, cell diameter and wall thickness on the High and Low quality samples coming from Val di Fiemme (mean values are showed on VOI as well as percentiles).

5.2.3 Finite Element Method modelling

The microstructure of the resonance wood undoubtedly influences the macro-behaviour of the material: the regular cell arrangement, the cells geometry and morphology together with the alternation of earlywood and latewood zones - exhibiting different densities and rigidity - determines the peculiar acoustic properties of this natural material (Caniato et al., 2007).

We propose now a scientific based manner to investigate the acoustical quality of such visco-elastic material, in order to properly employ it for making musical instruments, just starting from the deep knowledge of the microstructure.

The DIP tools applied on the μ-CT data provided the necessary tree-dimensional statistical sustain to characterise the microstructures. A finer vision of the cells features is furnished by the SEM technique. Coupling together these analyses we simulated the real medium geometry by a FEM model in order to obtain the modal behaviour of the wood pieces versus the frequency. The reproduction of the real wood samples, based on the acquired μ-CT and SEM images is showed in Figure 5.30 for the three different comings.

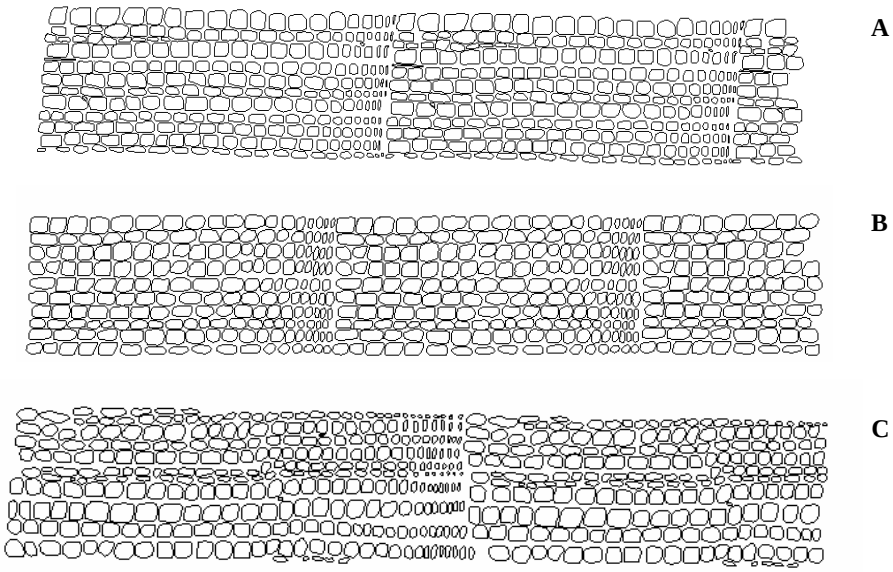

Figure 5.30 – The reproduction of the microstructures of Val di Fiemme (A), Tarvisio (B) and Canada (C) sample, obtained from the SEM images and the DIP on μ-CT data.

The model was solved on a mesh grid made of triangular elements by the software package program. Although the simulation suffers for its bi-dimensional formulation, it can be considered meaningful due to the strong anisotropy of the material. The results

showed in Figure 5.31 reveal a slightly different trend of the three varieties of woods which lead to three different acoustic macro-behaviours. The trend of the modes of the Tarvisio spruce suggests that this microstructure can vibrate more easily than the Val di Fiemme one, thus it seems not particularly suitable for the realization of the piano soundboard. It's worth observing that even if the Tarvisio microstructure seems to be more rigid because of the minor dimension of the rings, here the cells are equally spaced and larger than in the Val di Fiemme sample: this is supposed to cause a decrease of the Young module of the material. On the other hand, as the Canadian spruce sample presents smaller cells (when compared to the others) an increase of the Young modulus is expected for this case. The higher rigidity exhibited by the Canadian spruce makes it suitable for making parts of the musical instrument that have strict feature like, for instance, the ribs.

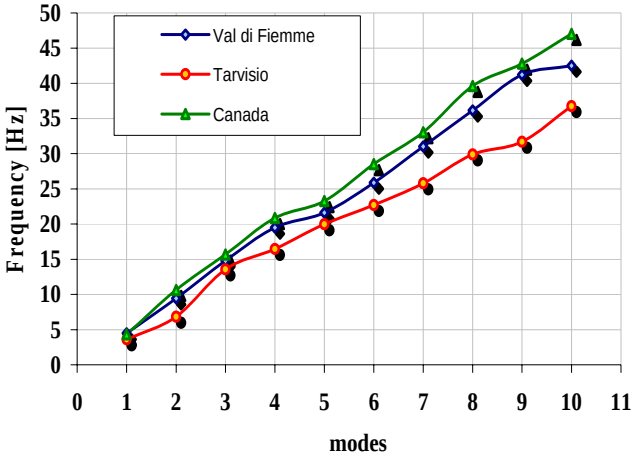

Figure 5.31 – Modal trend versus frequencies for the different coming samples.

We prepared another model then to investigate and compare the behaviour of the high and low quality wood coming from the Val di Fiemme. The reproduction of the real wood samples, based again on the acquired μ-CT and SEM images is showed in Figure 5.32 for the three different comings.

The model was solved on a mesh grid made of triangular elements by the Ansys software package. In this case, the target is also the confirmation, via such a rigorous method, of the real sorting out of the considered samples according to their different resonance quality.

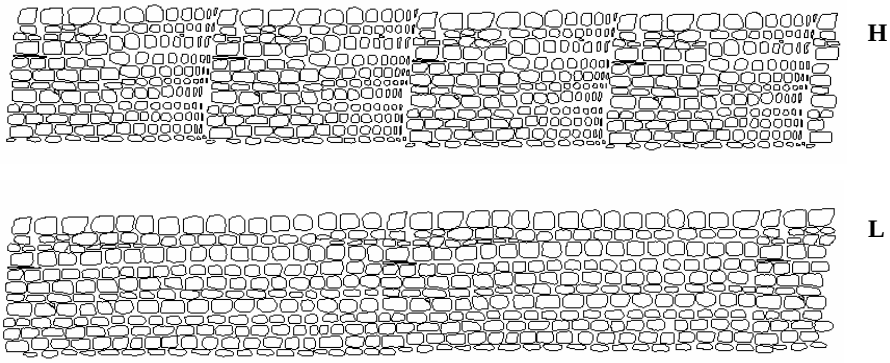

Figure 5.32 – The reproduction, obtained from the SEM images and the DIP on μ-CT data, of the microstructures of the high (H) and low (L) quality wood coming from the Val di Fiemme.

The results show different trend of the two analyzed microstructures that motivates the choice of the best wood quality to make the piano soundboards or other parts of musical instruments. In fact, the trend of the modes found for the low quality spruce (see Figure 5.33) shows that this microstructure vibrates more easily than the high quality one and this can be viewed as a serious defect for acoustical behaviour and sound transmission thorough the wood. The evidence is reasonably due to the greater presence of latewood in the high quality sample that acts as a reinforcing structure for the material.

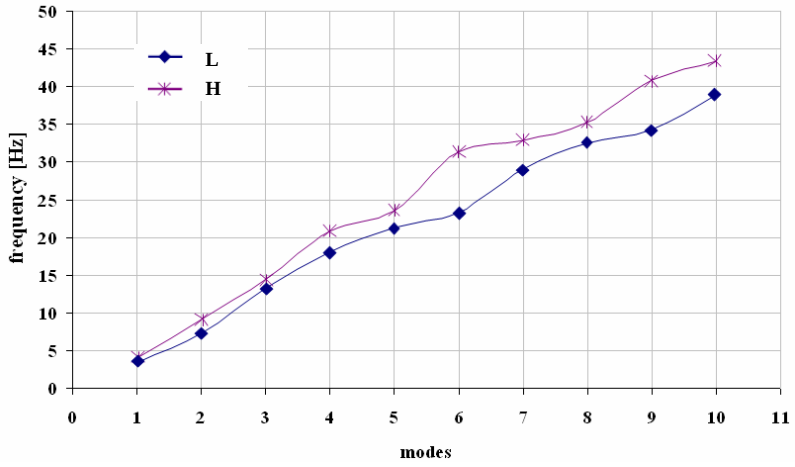

Figure 5.33 – Modal trend versus frequencies for the high and low quality samples.

5.3 Use of X-ray computed tomography as a new non-destructive tool for the optimization of process parameters in hybrid friction stir welding/TIG technique

X-ray μ-CT has been exploited also as a powerful investigative tool to reveal internal defects on aluminium samples welded by hybrid friction stir welding (HFSW) / tungsten inert gas (TIG) technique. Tomographic sans were acquired both at the SYRMEP beamline and at the TOMOLAB station, yielding three-dimensional visualization of the weld zone features, as well as morphological and geometrical characterization of voids, which can drive towards an optimal combination of the process parameters (Favretto et al., 2006).

5.3.1 1. Friction Stir Welding

Friction Stir Welding (FSW) is a solid state joining process developed and patented by TWI of Cambridge in the early 1990's (Thomas et al., 1991). As the name implies, in FSW a weld occurs when a non-consumable tool, the pin, is forced to move along the joint line while spinning. The frictional heat that is generated between the rotating tool and the pieces of metal softens the material, which can be mixed by the profiled tool, so that physical continuity between work-pieces can be obtained. The shape of the welding tool (composed by the *pin* in the lower part and the *shoulder* in the upper part) promotes a high hydrostatic pressure which forces the thermally softened material to flow around the tool. The material then cools and consolidates at the rear of the tool to form the solid state weld. The process is very simple and - with the exception of the clamping step - can be completely automated.

Because FSW produces weld joints with high mechanical and metallurgical properties for all wrought aluminium alloys – even those ones commonly classified as virtually non-weldable by conventional fusion welding techniques – the process has proven very attractive to the industry, in particular to shipbuilding, marine, aerospace and railway one. It is successfully applied today mainly on planar or tube-shaped components made of aluminium alloys (Heinz et al., 2000).

On the other hand the process requires high vertical pressures in order not to compromise the quality of the join and this in itself poses an upper limit to the advancing speed of the tool (bending stress). Generally speaking, although, acting on the tool geometry, researchers obtained substantial improvements on the welding speed,

FSW remains a slow process in comparison to the traditional welding techniques. Furthermore, given the values of the other parameters, increasing the advancing speed of the tool gives way to the formation of cracks on the opposite side to that in contact with the tool itself. The limit on welding speed advises to employ FSW only for large production volumes.

The presented study deals with a possible solution to one of the main drawbacks of this method, its relative slowness when compared to other processes like GMAW (gas metal arc welding) or VPPAW (variable polarity plasma arc welding), which is dictated by the limited strength of the welding probe.

A research group at Materials and Natural Resources Department of the University of Trieste recently proposed a new system consisting in the coupling of a FSW system with a GTAW (gas tungsten arc welding) torch, which can supply an adjustable amount of heat to the weld before the stirring action occurs. This lead to two advantages: first, the tool can act on a pre-heated - and consequentially, yet softened - material and second, the system results more flexible due to the added degree of freedom.

The need to investigate the weld formation mechanisms associated with the stir welding action requires an experimental non destructive testing procedure. In particular, it's of great importance to analyze the hybrid system in terms of joint quality, with specific reference to the absence of voids and porosity. X-ray μ-CT is one of the best candidates to solve the problem.

Figure 5.34 – HFSW is well-suited for the fast, highly automatized welding process of thin structures, like that employed for building modern high performances ships.

5.3.2 2. Hybrid versus traditional Friction Stir Welding

As above mentioned we propose a modified FSW process coupling the traditional tool with a GTAW torch. The goal is to obtain high mechanical properties joints,

keeping low ratios between rotational (RS) and travel (TS) speed. One of the disadvantages of classical FSW process is that lower is RS/TS ratio higher is the stress that the tool has to yield: high values of travel speed can lead to the rupture of the tool. In HFSW an auxiliary energy source locally preheats the material to be welded before the FSW tool complete the process. This is done without reaching the melting condition of the base metal, so that all the advantages of FSW over traditional processes are preserved. A pre-heating performed with a GTAW torch is used in order to reduce the stresses on the tool during friction stir welding (see Figure 5.35): additional heat input facilitate the tool to plasticize the material, without reducing the travel speed; the amount of electricity current has to be calibrated in order to not fuse the material before the passing of the FSW tool. The result is a lowering of the flow stress of the material encountered by the FSW tool, which leads to lower stresses on the relatively delicate pin structure. Moreover, the vertical load acting on the shoulder-workpiece interface to restrain the metal vertical flow can be reduced while keeping the optimal operating conditions.

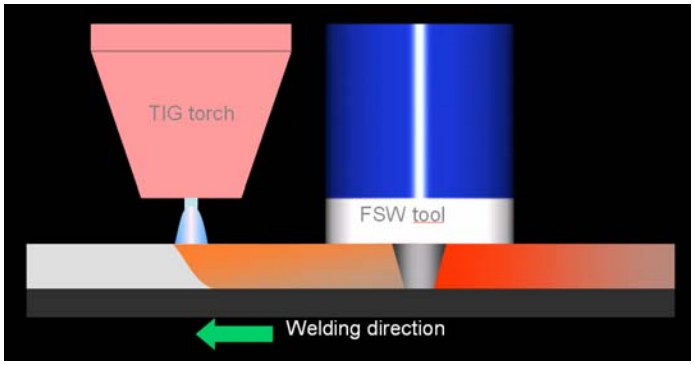

Figure 5.35 – Sketch of the HFSW operating principle based on the preheating of the workpiece, in order to soften the base material which invests the FSW tool pin and shoulder. This helps in reducing the mechanical and tribological stresses, thus allowing for enhanced performance welds.

Furthermore, it has been proven that the quality of the joint is strongly linked to the degree of plasticized material mixing in the vicinity of the tool. During FSW the thermally softened material in the weld joint undergoes a complicated deformation path which is not yet fully understood. Unfortunately the mixing stage is affected in different degrees by all the welding parameters, such as the torch current, the advancing speed, the rotating speed, the geometry of the tool and the vertical pressure. In other words, in order to obtain a high quality joint, many different parameters that control the HFSW process have to be combined together, and an exhaustive investigation of the optimal

process conditions is needed. In this study, we started examining the influence of the torch current on produced welds.

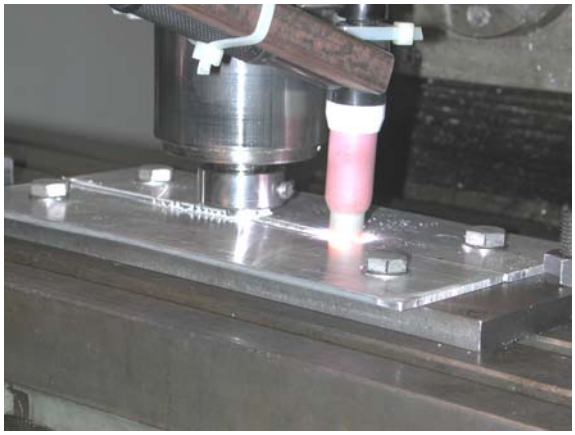

Figure 5.36 – HFSW test were conducted using this simple equipment, in order to demonstrate the working principle on an AA6060-T5 planar sample.

It's worth mentioning the joint zones which are differently affected by the FSW process: the weld nugget

The microstructure of a friction stir weld depends on the tool design, the rotation and translation speeds, the applied pressure and the characteristics of the material being joined. However, it is possible to distinguish among several zones: the central nugget region containing the onion-ring flow-pattern is the most severely deformed region; then the thermo-mechanically affected zone (TMAZ); far away, the heat affected zone (HAZ) similarly to the conventional welds; finally, the unaffected zone (see Figure 5.37).

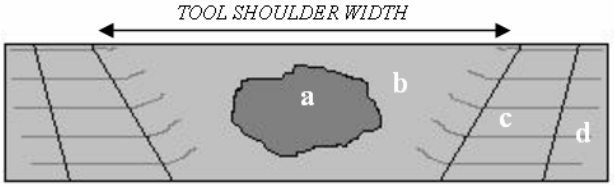

Figure 5.37 – A scheme illustrating the FSW affected zones: the weld nugget (a), the thermo-mechanically affected zone (b), the heat affected zone (c) and the unaffected zone (d).

5.3.3 Sample preparation and preliminary analysis

In the first part of this study, AA6060-T5 friction stir welds were performed with contemporaneous use of GTAW torch; the parameters of welding process are reported

in Table 5.6. Welds were cross-sectioned perpendicularly to the welding direction, grinded with SiC paper, polished with diamond suspension and etched with 100 ml H_2O + 2 ml HF for 4 minutes for the micrographic evaluation.

Digital pictures were taken on the cross section with a Nikon Coolpix 990 connected to an Optiphot Nikon optical microscope. In Figure 5.38 the aspect of the microstructure of welded zone is reported.

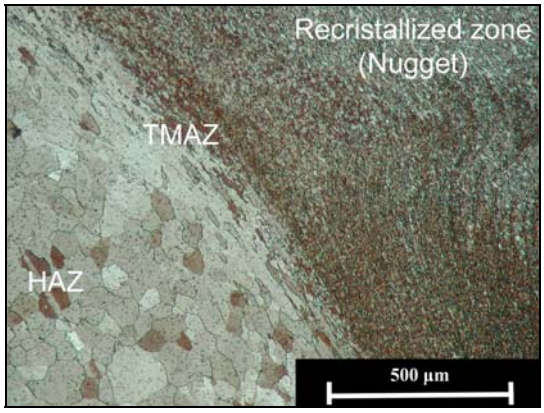

Figure 5.38 – A micrograph image of the welded zone.

From each of the investigated welds a sample was extracted just cutting the weld perpendicularly to the join direction. This way, a typical sample with a cross section of around 4×4 mm^2 (it roughly corresponds to the thickness of the Al foil) and a height of 8-10 mm was created, containing the weld zone approximately in the middle of its height.

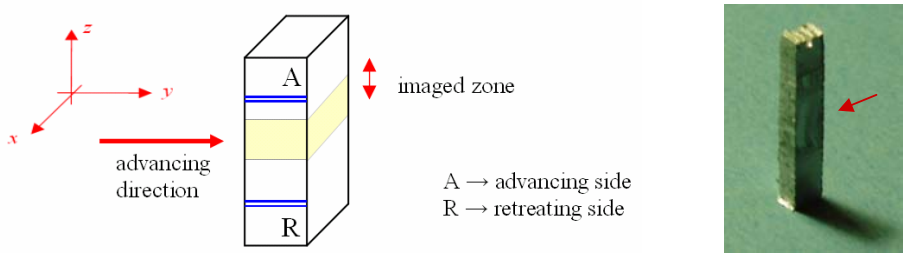

Figure 5.39 – Scheme of the sample extraction (left) from the welded zone and the sample (right).

Planar radiographs and complete tomographic scans were acquired for each of the samples. The beam energy during the experiment at the SYRMEP beamline was set to 26 keV, a value high enough to assure a good photons count on the detector plane, in spite of the high sample absorption. The samples were imaged on the weld zone with a final voxel size of 9 microns.

Name of the sample	RS/TS [rpm / mm·min^{-1}]	Ampere of GTAW arc
A	10	40
B	10	80
C	10	100

Table 5.6 – Summary of the main welding conditions of AA6060-T5 samples imaged at SYRMEP.

Hereafter a planar radiograph from one of the aluminium samples is presented. Sometimes, as in the case depicted by Figure 5.40, simply from the radiograph of the sample it's possible to detect an internal defect, if its size is big enough. Obviously, to understand its morphology and connectivity, a complete tomographic reconstruction is needed.

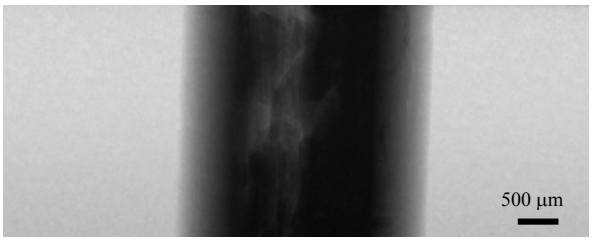

Figure 5.40 – A planar radiograph of sample C imaged at the SYRMEP beamline.

As to the slices, because the imaged material is homogeneous some typical artefacts that derive from tomographic reconstruction are better visible: this is the case, for example, for the ring artefacts that we reduced applying an appropriate filtering procedure.

The entire length of the sample was investigated, even if the middle one is the most interesting because contains the welded zone. Because the travel direction of the pin is completely comprised in the XY plane (i.e. the slice plane), the upper and lower zones of the imaged volume represent respectively the so called advancing and retreating sides of the weld (according to the angular velocity of the rotating tool, if concordant or not with the advancing velocity).

5.3.4 Results and discussion

As showed in Figure 5.41, porosity and defects due to the pin rotational and advancing movements normally enlarge as soon as the torch current is increased (from 40 to 100 Ampere). Also small pores, probably produced independently from the rotating tool advancing process, are successfully revealed (see the red circle in Figure 5.42).

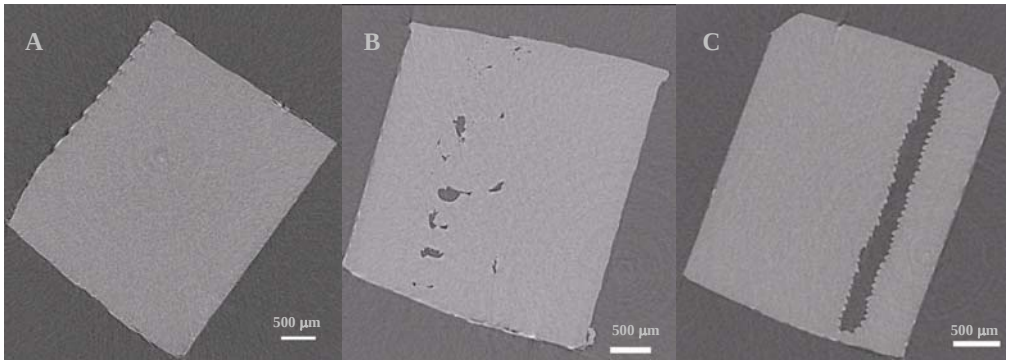

Figure 5.41 – Slices reconstructed from samples A, B and C. HFSW parameters were maintained the same, except the torch current, which was increased.

The 3D volume can be assembled for each sample just stacking the slices; the weld zone can be rendered in order to visualize the porosity and the presence of defects along the weld direction. Both looking at the planar slices and at the three-dimensional volume, the effect of the rotating pin is self evident, especially when the torch current is increased. Measuring the effective magnitude of the voids, a quantification of the joint quality can be obtained. Also the pitch of the tool is clearly distinguishable and can be measured on the digital images.

Accurately examining these preliminary results, the high resolution of the acquired images is appreciable: it allows also the identification and characterization of very small defects or isolated pores that appear nearby the weld central zone (see again the red circle of Figure 5.42). Structures similar to onion-rings are a consequence of the way in which a threaded device deposits material from the front to the back of the welding tool.

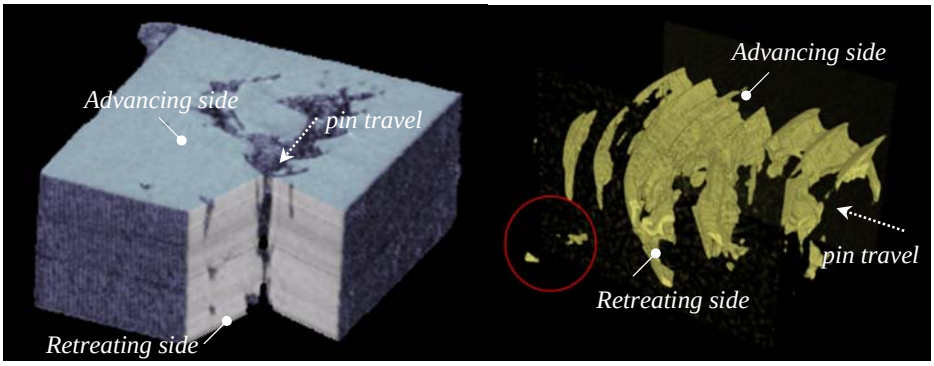

Figure 5.42 – A three-dimensional visualization of the entire volume reconstructed for sample B (left) and the rendering of the voids/defects (right).

All the collected results confirm the need of keeping the current as low as possible and propose μ-CT as a valid and promising technique to characterize aluminium samples both during the process optimization step and – with minor improvements – as a routine methodology for the joining quality evaluation.

However, we judge that in many practical industrial cases, just conventional radiography could be enough to provide an idea of the presence of internal defects on joints, while μ-CT should be reserved to those cases that require a three-dimensional evaluation of the voids distribution or of the material mixing occurred following the welding process.

Later on, in the second part of the study, several tomographic studies were carried on at the TOMOLAB station too, in order to exploit the significant advantage of the larger FOV available there. The choices for the design and the assembling of the TOMOLAB equipments represents a nice compromise between high resolution - down to few micrometers - and high flexibility to deal with both light materials and highly attenuating ones, like aluminium, relying on the strong penetrating power.

The delivered beam energy allows to pass and thus to scan thicker samples, that can be mounted on the turn-table without extracting them from the original joint, but usually just reducing opportunely the size of the pieces. Two and three multiple layer of aluminium alloys of different composition were investigated at TOMOLAB (see Figure 5.43). The characteristics of the employed Al alloys are summarized in Table 5.7.

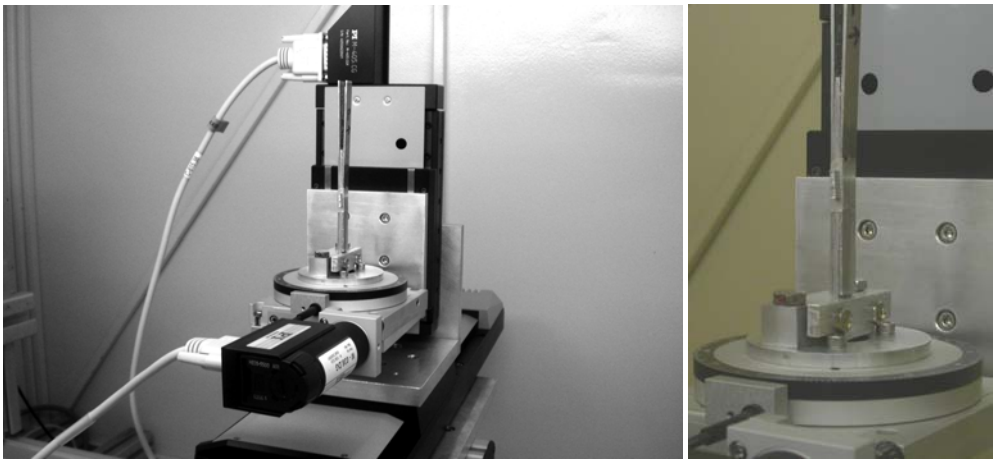

Figure 5.43 – The sample (triple layer of Al foils) mounted on the turn table inside the TOMOLAB facility. A special sample holder was designed to keep the piece vertical; the central part was scan only.

Composition [%]	Si (max)	Fe (max)	Cu	Mn	Mg	Cr (max)	Ti (max)	Zn (max)	Zr+Ti (max)	Other	
2024	0.50	0.50	3.80-4.90	0.30-0.90	1.20-1.80	**0.10**	**0.15**	0.25	0.20	0.05	0.15
7075	0.40	0.50	1.20-2.00	0.30	2.10-2.90	**5.10-6.10**	**0.18-0.28**	0.20	0.25	0.05	0.15

Table 5.7 – Chemical composition of the Al alloys imaged at the TOMOLAB facility.

At the TOMOLAB facility we worked at 110 kV, 220 μA with a magnification factor of 2× ($D_{od} = 16cm$). As expected with such a high energy the beam hardening and also ring artifacts degrade sensibly the reconstructed images. The beam hardening effect is much more visible at the external borders of the largest dimension of the sample. Ring artifacts were partially reduced by the post-processing procedure illustrated in the third chapter.

It seems not an easy task to quantitatively distinguish between the two different alloys by segmentation, because their attenuating properties at the working energies are very close to each other. However, our eyes can do this better, intuitively identifying the separation interfaces between the two components on the slices as well as on the 3D volumes. In Figure 5.44 a 3D reconstructed volume is virtually inspected by views from different oriented planes; the slice plane is indicated and the others cross sections too.

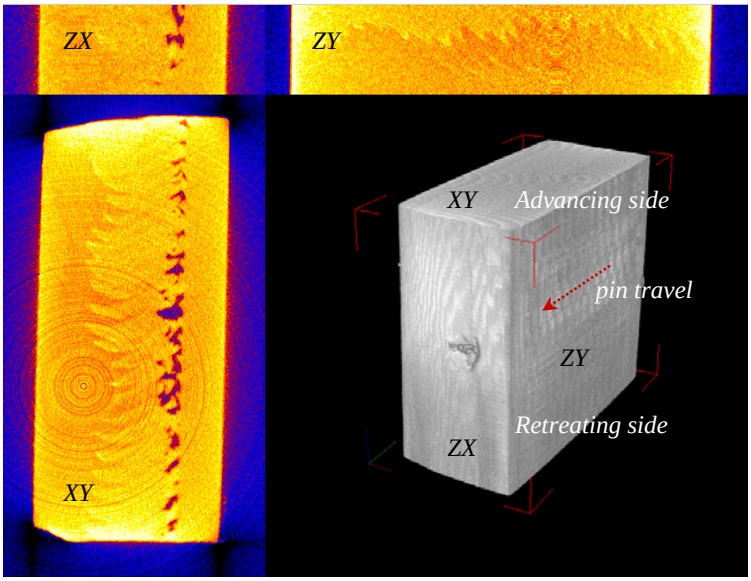

Figure 5.44 – A 3D volume of the HFSW sample virtually sectioned by orthogonal planes. The volume orientation with respect to the pin travel direction is indicated for reference.

Always in the images it is important to correctly orient the portrayed volume with respect to the pin travel direction and thus to the advancing and retreating sides.

The material flow occurred during the welding process basically generated by the FSW tool geometry and welding parameters is clearly visible. The images also reveal that the material deposition flowed in the direction of tool rotation (i.e. clockwise).

For the future a valid suggestion is the use of a contrast-giving marker material prior to welding, as for instance a Titanium powder implanted into aluminum sheets (Donath et al., 2004).

Conclusions and perspectives

The overall objective of this thesis work has been to define a non-destructive procedure suitable for the microstructural characterisation of materials exploiting the X-ray computed microtomography technique.

This globally required the acquisition of different competences: first, the setting up of a tomographic facility dedicated to the image acquisition and then the development of specific tools for the quantitative analysis of the acquired three-dimensional data, in order to extract their peculiar microscopic properties. The thesis structure has been logically subdivided in two main parts which correspond to the chronological development of the work.

In the first part, working at the SYRMEP beamline of Elettra, I improved my theoretical knowledge about X-ray imaging associated to a third-generation synchrotron source. At the same time, I practiced about μ-CT with the existent tomographic set up of the beamline. Then I contributed to the realization of the TOMOLAB station, a cone-beam μ-CT facility equipped with a microfocus X-ray source, which is complementary to the SYRMEP beamline. During the assembling of the system components (i.e. the X-ray source, the sample stages and the detector) we highlighted the critical aspects related to their combination in order to achieve the desired performances. I carried out a characterisation of this open machine to evaluate the achievable spatial resolution varying the different working parameters (i.e. the beam energy, the focal spot size, the geometrical magnification, the detector settings, the slices reconstruction etc.). These aspects have been considered fundamental to asses the capabilities of the specific machine. Thus we optimized the operating parameters to perform the different

experiments. We also exploited the possibility of acquiring phase-contrast images thanks to the micrometric focal spot size of the X-ray tube.

We verified that the foreseen targets have been completely satisfied, especially in terms of the complementarities with respect to the SYRMEP beamline, allowing the imaging of a wider range of materials of a larger size, while maintaining the high spatial resolution (we demonstrated that few micrometers can be revealed on centimetric samples).

However, we have also pointed out the main artefacts that contribute to the deterioration of the image quality (beam hardening, ring artefacts, geometrical misalignment etc.), suggesting specific methods to avoid or at least to reduce them.

In the second part, I dedicated the main effort to the development of methodologies and customized programs for the analysis of the tomographic data. I gave my contribution to the realization of a software package, PORE3D, which is a collection of algorithms and procedures aimed at the quantitative description of the microstructure of complex porous media. The three-dimensional nature of a μ-CT dataset requires not a trivial approach for its characterisation, thus we developed a skeleton-based method to obtain geometrical, morphological and topological measurements on features contained into the 3D space. We also outlined a new approach for the extraction of the centred and shortest paths inside a porous material, which is sensitively faster.

The digital image processing methodologies have been tested on a large set of different applications in the field of material science and earth science, using 3D data acquired both at TOMOLAB and at SYRMEP. Particularly, we investigated three different materials: open-cells polyurethane foams employed in the automotive industry for noise control applications, spruce resonance wood used to make musical instruments and aluminium joints prepared by a hybrid-friction stir welding process.

The results proved clearly enough the potentials and the capabilities of X-ray μ-CT to discern and define the microstructures inside the investigated samples. We demonstrated that μ-CT, coupled with intensive digital image processing, can be considered as a valid complemental, or even substitutive, approach to obtain the measurement of those parameters of purely geometrical nature. In all the presented studies, we have indicated a work-flow, from the image acquisition to the geomorphologic characterization of the material, which can be practically applied to control choice, design, production and use of such materials.

At the same time the success of the activities presented in this dissertation opens the way to a large extent of scientific and industrial applications. Due to growing interest in porous materials, the possibility of deriving their physical properties from the three-dimensional digital microstructure is very attractive. The state-of-the-art facilities available represent an ideal tool to investigate several phenomena involving the microstructure of artificial or natural materials. On the other hand the computational power of modern calculators allows the rapid examination of huge amount of data.

We trace here just few key-aspects in order to address the future activities:

- digital image processing methods need to be tailored for a wide range of applications, each one requiring its own customization. This means that new specific algorithms suited, for example, for multiphase systems or fibrous materials, will be more and more essential. Furthermore, the developed PORE3D program necessitates to be optimized for speed and efficiency, in order to be able to manage larger volumes;
- the existent tomographic set-up of the TOMOLAB facility could be further upgraded, for instance, combining different type of detectors (with a larger field of view, a higher dynamic range, or furnished with an image intensifier). The sample stages could also be modified in order to better fit new requirements (precision, compactness etc.). The slices reconstruction process could be further speed up, in order to achieve a quasi real-time tomography. Finally, under the acquired know-how, other solutions could be easier designed of a tomographic facility capable of sub-micrometric spatial resolution on smaller object;
- several applications have shown the need of numerical data processing further than digital image processing, involving the numerical modeling of materials via, for example, finite element methods or direct simulation on the digital data as the lattice Boltzmann method (for example, the investigation of materials behaviour under stress, the multi-phase fluid flow study inside porous media etc.). This should be also considered in the future plans.

Bibliography

Al-Kharusi, A.S. and Blunt, M.J., *Network extraction from sandstone and carbonate pore space images*, J. Petrol. Sci. Eng. **56**, 219-231 (2007).

Al-Raoush, R.I. and Wilson, C.S., *Extraction of physically-realistic pore network properties from three-dimensional synchrotron X-ray microtomography images of unconsolidated porous media systems*, Journal of Hydrology **300**, 44-64 (2005).

Al-Raoush, R.I., Thompson, K., and Willson, C.S., *Comparison of Network Generation Techniques for Unconsolidated Porous Media*, Soil Sci. Soc. A. J. **67**, 1687-1700 (2003).

Appoloni, C.R., Fernandes, C.P., de Mello Innocentini, M.D., Macedo, Á., *Ceramic Foams Porous Microstructure Characterization By X-ray Microtomography*, Materials Research 7(4), 557-564 (2004).

Arfelli, F., Barbiellini, G., Bregant, P., Calligaris, F., Cantatore, G., Castelli, E., Dalla Palma, L., de Guarrini, F., Giacomich, R., Longo, R., Poropat, P., Rosei, R., Sessa, M., Stacul, F., Tonutti, M., Tomasini, F., Tromba, G., Vacchi, A., Vidimari, R., Zanini, F. and Zuiani, C., *SYnchrotron Radiation for MEdical Physics. A comparison between digital and conventional screen-film systems*, Phys. Med. **9**(2-3), 188-191 (1993).

Arfelli, F., Bonvicini, V., Bravin, A., Cantatore, G., Castelli, E., Dalla Palma, L., Di Michiel, M., Fabrizioli, M., Longo, R., Hendrik Menk, R., Olivo, A., Pani, S., Pontoni, D., Poropat, P., Prest, M., Rashevsky, A., Ratti, M., Rigon, L., Tromba, G., Vacchi, A., Vallazza, E. and Zanconati, F., *Mammography with synchrotron radiation: phase-detection techniques*, Radiology **215**, 286-293 (2000).

Ashbridge, D.A., Thorne, M.S., Rivers, M.L., Muccino, J.C. and O'Day, P.A., *Image optimization and analysis of synchrotron X-ray computed microtomography (μCT) data*, Computers & Geosciences **29**, 823-836 (2003).

Attali, D. and Montanvert, A., *Computing and Simplifying 2D and 3D Continuous Skeletons,* Computer Vision and Image Understanding **67**(3), 261-273 (1997).

Barret, J.F. and Keat, N., *Artifacts in CT: Recognition and Avoidance*, Radiographics **24**(6), 1679-1691 (2004).

Baruchel, J. and Kvick, A., *Synchrotron radiation imaging and diffraction for industrial applications*, Europhysics News **35**(2) (2004).

Baruchel, J., Buffière, J.Y., Maire, E., Merle, P. and Peix, G., *X-ray Tomography in Material Science*, Hermès Sciences Publications, Paris (2000).

Bear, J., *Dynamics of fluids in porous media*. American Elsevier Publishing Company, New York (1972).

Beckman, F., Bonse, U., Busch, F. and Gunnewig, O., *X-ray microtomography (microCT) using phase contrast for the investigation of organic matter*, J. Comput. Assis. Tomogr. **21**(4), 539-553 (1997).

Beckmann, F., Donath, T., Lippmann, T., Schreyer, A. and Clemens, H., *Synchrotron-radiation based microtomography of new materials for lightweigth construction*, GKSSForschungszentrum, Geesthacth, Germany (2003).

Bernard, D., *3D Quantification of Pore Scale Geometrical Changes Using Synchrotron Computed Microtomography*, Oil & Gas Science and Technology – Rev. IFP **60**(5), 747-762 (2005).

Bernardini, F., Demarchi, G., Favretto, S., Montagnari, M., Princivalle, F. and Alberti, A., *Greenstone artefacts in prehistory: preliminary results and perspectives based on X-ray computerized microtomography*, Science for Cultural Heritage, Lussingrande, Kroatia, August 2007.

Bernhardt, R., Scharnweber, D., Müller, B., Thurner, P., Schliephake, H., Wyss, P., Beckmann, F., Goebbels, J. and H. Worch, *Comparison of microfocus- and synchrotron X-ray Tomography for the analysis of osteointegration around Ti6Al4V-implants*, European Cells and Materials **7**, 42-51 (2004).

Berthaut, J., Ichchou, M.N. and Jézéquel, L., P*iano soundboard: structural behavior, numerical and experimental study in the modal range*, Applied Acoustics **64**, 1113-1136 (2003).

Bertrand, L., *Synchrotron Imaging for Archaeology, Art History, Conservation, and Palaeontology,* Physical Techniques in the Study of Art, Archaeology and Cultural Heritage, Vol. 2, pp. 97-114. Bradley, D. and Creagh, D. (Eds). Elsevier (2007).

Beucher, S. and Lantejoul, C., *Use of Watershed in Contour Detection*, Proc. Int. Workshop Image Process., CCETT, Rennes, France, 1979.

Biot, M.A., *The theory of propagation of elastic waves in fluid saturated porous solid. I Low frequency range*, *II high frequency range*, JASA 28 (1956).

Birks, J.B., *The Theory and Practice of Scintillator Counting*, Mac-Millan, New York (1964).

Born, M., Wolf, E., *Principle of Optics*, 6th ed., Pergamon Press, Oxford, New York, 1980.

Bregant, L., Favretto, S. and Bertolini, C., *X-ray Tomography of Foam and Felt for Noise Control Application in the Automotive Industry*, 18th Rieter Automotive Conference, Switzerland, June 2007.

Bregant, L., Favretto, S. and Bertolini, C., *μCT-Based Measurements of the Characteristic Lengths of Polyurethane Foams Employed in the Automotive Industry for Noise Control Applications,* 5th World Congress on Industrial Process Tomography, Bergen (Norway), September 2007.

Brennan, M.J. and To, W.M., *Acoustic properties of rigid-frame porous materials – an engineering perspevtives*, Applied Acoustics **62**, 793-811 (2001).

Bressan, G., Favretto, S., Fonda, G., Kaleb, S., Melis, R., Montenegro, M.E., Pugliese, N., Riccamboni, R., Russo, A., Sodini, N., Tromba, G. and Vita, F., *Actuopalaeontology: a Polyfunctional Tool for Archaeology*, Science for Cultural Heritage, Lussingrande, Kroatia, August 2007.

Bressan, G., Favretto, S., Kaleb, S. and Tromba, G., *Applicazione della microtomografia computerizzata a raggi X allo studio predittivo della struttura di alghe rosse calcaree*, 38° Congresso SIBM – Santa Margherita Ligure (Italy), June 2007.

Bressan, G., Kaleb, S., Favretto, S., Tromba, G. and Vita, F., *X-ray microtomography application to a predictive evaluation of coralline algae structure*, Elettra Highlights 2006-2007, December 2007.

Bronnikov, A.V., *Cone-beam reconstruction by backprojection and filtering*, J. Opt. Soc. Am. A **17**(11), 1994-2000 (2000).

Bronnikov, A.V., *Theory of quantitative phase-contrast computed tomography*, J. Opt. Soc. Am. A, **19** (3), 472-480 (2002).

Brown, R.L. and Bold, R.H., *The measurement of flow resistance of porous acoustic materials*, JASA 13 (1942).

Burger, W. and Burge, M., *Digital Image Processing: an Algorithmic Approach Using Java*, Springer 2007.

Caniato, M., Favretto, S. and Lucchini, E., *A new approach for the characterization of the resonance wood*, International congress of Acoustics, Madrid, September 2007.

Caniato, M., Favretto, S. and Lucchini, E., *Comparison between different resonance woods by a new scientific method*, International congress of Acoustics, Madrid, September 2007.

Caniato, M., Favretto, S., Lucchini, E., *Caratterizzazione microstrutturale di legno per strumenti musicali*, Proceedings of Italian acoustic association congress, Firenze, 13-15 June 2007.

Champoux, Y., Stinson, M.R. and Daigle, G.A., *Air based system for measurement of porosity*, JASA 89 (1991).

Cheung, Y., *k-Means: A new generalized k-means clustering algorithm*, Pattern Recognition Letters **24**, 2883-2893 (2003).

Cloetens, P., Boller, E., Ludwig, W., Baruchel, J., and Schlenker, M., *Absorption and phase imaging with synchrotron radiation*, Europhysics News **32**(2) (2001).

Coenen, J., Tchouparova, E. and Jing, X., *Measurement parameters and resolution aspects of micro X-ray tomography for advanced core analysis*, SCA2004-36.

Cohen, L.D. and Kimmel, R., *Global minimum for active contour models: a minimal path approach*, Int. J. Computer Vision **24**(1), 57–78 (1997).

Coles, M.E., Hazlett, R.D., Muegge, E.L., Jones, K.W., Andrews, B., Dowd, B., Siddons, P., Peskin, A., Spanne, P. and Soll, W.E., *Developments in synchrotron X-ray microtomography with applications to flow in porous media*, SPE-36531, in Annual technical conference and exhibition proceedings, v. omega, Formation evaluation and reservoir geology: Society of Petroleum Engineers, pp. 413-424 (1996).

Cullignan, K.A., Wildenschild, D., Christensen, B.S.B., Gray, W.G. and Rivers, M.L., *Pore-scale characteristic of multiphase flow in porous media: a comparison of air-water and oil-water experiments*, Advances in Water Resources **29**, 227-238 (2006).

Davis, G.R. and Elliott, J.C., *Artefacts in X-ray microtomography of materials*, Materials Science and Technology **22**(9), 1011-1018 (2006).

del Risco Norrild, L., Ronnqvist, C., Fransson, K., Brenner, R., Gustafsson, L., Edling, F. and Kullander, S., *Calculation of the modulation transfer function for the X-ray imaging detector DIXI using Monte Carlo simulation data*, Nucl. Instrum. Meth. Phys. Res. A 466, 209-217 (2001).

Delerue, J.F.C. and Perrier, E., *DXSoil, a library for 3D image analysis in soil Science*, Computers & Geosciences 28, 1041-1050 (2002).

Deschamps, T. and Cohen, L.D., *Fast extraction of minimal paths in 3D images and applications to virtual endoscopy*, Med. Image Anal. **5**(4), 281–299 (2001).

Dierick, M., Masschaele, B. and Van Hoorebeke, L., *Octopus, a fast and user-friendly tomographic reconstruction package developed in LabView*, Meas. Sci. Technol. **15**, 1366–1370 (2004).

Dillard, T., N'guyen, F., Maire, E., Salvo, L., Forest, S., Bienvenu, Y., Bartout, J.-D., Croset, M., Dendievel, R. and Cloetens, P., *3D quantitative image analysis of open-cell nickel floams under tension and compression loading using X- ray microtomography*, Philosophical Magazine **85**(19), 2147-2175 (2005).

Donath, T., Beckmann, F., Zettler, R., dos Santos, J., Lohwasser, D., Lippman, T., Clemens, H. and Schreyer, A., *Investigation of material flow in friction stir welding using computed microtomography*, AIP Conf. Proc. 705: SRI 03 San Francisco, California, pages 1312–1315 (2004).

Dong, H., *micro-CT imaging and pore network extraction*, PhD thesis, Earth Science and Engineering Dep., Imperial College London, 2007.

Dong, H., Touati, M. and Blunt, M.J., *Pore Network Modeling: Analysis of Pore Size Distribution of Arabian Core Samples*, SPE105156, 2007.

Donnelly, E.F. and Price, R.R., *Polychromatic phase-contrast computed tomography*, Medical Physics **34**(8), 3165-3168 (2007).

Dougherty, G. and Kawaf, Z., *The point spread function revisited: image restoration using 2D convolution*, Radiography **7**, 255-262 (2001).

Eberhardt, C.N. and Clarke, A.R., *Automated reconstruction of curvilinear fibres from 3D datasets acquired by X-ray microtomography*, Journal of Microscopy **206**(1), 41-53 (2002).

Elliott, J.A. and Windle, A.H., *In-situ deformation of an open-cell flexible polyurethane foam characterised by 3D computed tomography*, J. of Materials Science **37**, 1547-1555 (2002).

Falcone, P. M., Baiano, A., Zanini, F., Mancini, L., Tromba, G., Montanari, F. and del Nobile, M.A., *A novel approach to the study of bread porous structure: phase-contrast X-ray microtomography*, Journal of Food Science **69**(1) (2004).

Falcone, P.M., Baiano, A., Zanini, F., Mancini, L., Tromba, G., Dreossi, D., Montanari, F., Scuor, N., and Del Nobile, M.A., *Three-dimensional Quantitative Analysis of Bread Crumb by X-ray Microtomography*, J. of Food Science **70**(4) (2005).

Favretto, S., Scuor, N., Zanini, F., Lucchini, E., *Use of X-ray computed tomography as a new non-destructive tool for the optimization of process parameters in hybrid friction stir welding/TIG technique*, 8° Convegno Nazionale AIMAT – Palermo (Italy), June 2006.

Feldkamp, L.A., Davis L.C. and Kress, J.W., *Pratical cone-beam algorithm*, J. Opt. Soc. Am. A 1 – 6 (1984).

Fierz, F., Leukers, B., Degistirici, Ö., Irsen, S., Beckmann, F. and Müller, B., *Design and characterization of 3D-printed hydroxyapatite scaffolds using synchrotron-radiation-based micro computed tomography*, European Cells and Materials **11**(2):22 (2006).

Fioravanti, M. and Ricci, R., *L'impiego della tomografia computerizzata per misure densitometriche sul legno: indagine sperimentale e risultati metodologici*, Annali dall'Accademia Italiana di Scienze Forestali, **XL** (1991).

Fitzgerald, R., *Phase-sensitive X-Ray Imaging*, Physics Today (2000).

Flannery, B.P., Deckman, H.W., D'Amico, K.L. and Roberge, W. G., *Three-dimensional X-ray Microtomography*, Science **237**, 1439-1444 (1987).

Fromm, J.H., Sautter, I., Matthies, D., Kremer, J., Schumacher, P. and Ganter, C., *Xylem Water Content and Wood Density in Spruce and Oak Trees Detected by High-Resolution Computed Tomography*, Plant Physiol. **127**, 416-425 (2001).

Fu, X., Elliott, J.A., Bentham, A.C., Hancock, B.C. and Cameron, R.E., *Application of X-ray Microtomography and Image Processing to the Investigation of a CompactedGranular System*, Part. Part. Syst. Charact. **23**, 229–236 (2006).

Gallucci, E., Scrivener, K., Groso, A., Stampanoni, M. and Margaritondo, G., *3D experimental investigation of the microstructure of cement pastes using synchrotron X-ray microtomography (μCT)*, Cement and Concrete Research **37**(3), 360-368 (2007).

Garboczi, E.J., Bentz, D.P. and Martys, N.S., *Digital images and computer modeling*, Experimental Methods in the Physical Sciences **35**. Methods in the Physics of Porous Media, Chapter 1, Academic Press, San Diego CA, 1-41 p., 1999.

Gerlach, S., Römich, H., Lopéz, E., Zanini, F., Mancini, L., and Rigon, L., *Non-destructive analysis and testing of museum objects*, chapter Phase contrast microtomography for archaeological glasses, pages 147-151, in A. Denker et al. editors, *Non-destructive analysis and testing of museum objects*, Fraunhofer IRB Verlag (2006).

Giblin, P. and Kimia, B.B., *A formal classification of 3D medial axis points and their local geometry*, IEEE. T. Pattern. Anal. **26**(2), 238–251 (2004).

Goel, A., Arns, C.H., Holstad, R., Gregersen, Ø.W., Bauget, F., Averdunk, H., Sok, R.M., Sheppard, A.P. and Knackstedt, M.A., *Analysis of the impact of papermaking variables on the structure and transport properties of paper samples by x-ray microtomography*, J. Pulp and Paper Science **32**(3), 111-122 (2006).

Grider, D.E., Wright, A. and Ausburn, P.K., *Electron beam melting in micro-focus X-ray tubes*, J. Phys. D: Appl. Phys. **19**, 2281-2292 (1986).

Gruner, S.M., Tate, M.W. and Eikenberry, E.F., *Charge-coupled device area x-ray detectors*, Rev. of Sci. Instrum. **73**(8), 2815-2842 (2002).

Han, F., Seiffert G., Zhao Y. and Gibbs B., *Acoustic absorption behaviour of an open-celled aluminum foam*, J. Phys. D: Appl. Phys. **36**, 294-302 (2003).

Heinz, A., Haszler, A., Keidel, C., Moldenhauer, S., Benedictus, R. and Miller, W.S., *Recent development in aluminium alloys for aerospace applications*, Materials science & engineering *A280, 102-107 (2000).*

Herman, G.T., *Image Reconstruction from Projections: the Fundamentals of Computerized Tomography*, Academic Press, New York (1980).

Horcin, P. and Gubriansky, V., *Properties of wood in musical instruments making*, proceedings Forum Acusticum, Budapest (2005).

Hutchins, C.M., *Measurable Characteristics of Violin-Family Instruments in Relation to the Sound of a High-Quality Violin*, MRS Bulletin, pp. 29-31 March 1995.

Hyväluoma, J., Raiskinmäki, P., Jäsberg, A., Koponen, A., Kataja, M. and Timonen, J., *Evaluation of a lattice-Boltzmann method for mercury intrusion porosimetry simulations*, Future Generation Comput. Syst. **20**(6), 1003–1011 (2004).

Iglauer, S., Favretto, S., Soldan, A, Schena, G., Blunt, M.J., *3D visualization of CO_2 gas capture and multi-phase flow behaviour in unconsolidated quartz sand utilizing synchrotron Computed Tomography*, in preparation.

Illman, B. and Dowd, B., *High resolution microtomography for density and spatial information about wood structures*, SPIE`s 44th Annual Meeting and Exhibition: The International Symposium on Optical Science, Engineering and Instrumentation, Colorado Convention Center & Marriott City Center, Denver, Colorado, USA, July 1999.

J. Sijbers and Postnov, A., *Reduction of ring artifact in high resolution micro-CT reconstructions*, Phys. in Med. and Biol. **49**(14), 247-253 (2004).

Johnson, D.L., Koplik, J., and Dashen, R., *Theory of dynamic permeability and tortuosity in fluid saturated porous media*, J. Fluid Mechanicsm **176** (1987).

Kak, A.C. and Slaney, M., *Principles of Computed Tomographic Imaging,* IEEE PRESS (1987).

Kari, L., Lokander, M. and Stenberg, B., *Structure-borne sound properties of isotropic magneto-rheological rubber*, KGK Kautschuk Gummi Kunststoffe **55**, 669-673 (2002).

Kasae, P., Favretto, S., Mancini, L. and Tromba, G., *PORE3D: a program for quantitative image analysis of porous media*, Machine Vision and Applications J., submitted (2007).

Ketcham, R.A. and Carlson, W.D., *Acquisition, optimisation and interpretation of X-ray computed tomographic imagery: applications to the geosciences*, Computer & Geosciences **27**, 381-400 (2001).

Ketcham, R.A., *Computational methods for quantitative analysis of three-dimensional features in geological specimens*, Geosphere **1**(1), 31-41 (2005).

Kinney, J.H., Marshall, G.W., Marshall, S.J. and Haupt, D.L., *Three-Dimensional Imaging of Large Compressive Deformations in Elastomeric Foams*, J. of Appl. Polymer Science **80**, 1746-1755 (2002).

Klasens, H., *Measurment and calculation of unsharpness combinations in X-ray photography*, Philips Res Rep **1**, 241-249 (1946).

Knackstedt, M., Arns, C.H., Limaye, A., Sakellariou, A., Senden, T.J., Sheppard, A.P., Sok, R.M., Pinczewski, W.V. and Bunn, G.F., *Digital core laboratory: reservoir-core properties derived from 3D images,* J. of Petroleum Technology, May 2004, 66-68.

Knackstedt, M., Arns, M.C., Saadatfar, M., Senden, T., Sakellariou, A., Sheppard, A., Sok, R., Schrof, W. and Steininger, H., *Virtual Materials Design: Properties of*

Cellular Solids Derived from 3D Tomographic Images, Advanced Engineering Materials **7**(4) (2005).

Krimmel, S., Stephan, J. and Baumann, J., *3D computed tomography using a microfocus X-ray source: Analysis of artifact formation in the reconstructed images using simulated as well as experimental projection data*, Nucl. Instr. and Meth. in Phys. Res. A **542**, 399-407 (2005).

Lambert, J., Cantat, I., Delannay, R., Renault, A., Graner, F., Glazier, J.A., Veretennikov, I. and Cloetens, P., *Extraction of relevant physical parameters from 3D images of foams obtained by X-ray tomography*, Colloidal and Surfaces A, **263**, 295-302 (2005).

Lee, T-C., Kashyap, R. and Chu, C-N., *Building skeleton models via 3-d medial surface/axis thinning algorithms*, CVGIP: Graphic Models and Image Processing, **56**(6): 462-478 (1994).

Letang, J.-M. and Peix, G., *On-line X-ray focal spot assessment based on deconvolution using standard imaging devices*, NDT&E International **36**, 3030-317 (2003).

Levitz, P., *Off-lattice reconstruction of porous media: critical evaluation, geometrical confinement and molecular transport*, Advances in Colloid and Interface Science **77**, 71-106 (1998).

Lewitt, R.M., *Reconstruction algorithms: Transform methods*, Proceedings of the IEEE, **71**(3), 390-408 (1983).

Liang, Z., Ioannidis, M.A. and Chatzis, I., *Geometric and Topological Analysis of Three- Dimensional Porous Media: Pore Space Partitioning Based on Morphological Skeletonization*, J. of Colloid and Interface Science **221**(1), 13-24 (2000).

Lim, K.S. and Barigou, M., *X-ray micro-computed tomography of aerated cellular food products*, Food Research International **37,** 1001-1012 (2004).

Lindquist, W.B. and Lee, S.M., *Medial axis analysis of void structure in three-dimensional tomographic images of porous media*, Journal of Geophysical Research, **101**(B4), 8297-8310 (1996).

Lindquist, W.B. and Venkatarangan, A., *Investigating 3D geometry of porous media from high resolution images*, Physics and Chemistry of Earth (A) **25**(7), 593-599 (1999).

Lindquist, W.B., *3DMA-Rock: a software package for automated analysis of rock pore structure in 3-D computed microtomography images*, http://www.ams.sunysb.edu/˜lindquis/3dma/3dma.html.

Lindquist, W.B., Lee, S.M., Coker, D.A., Jones, K.W. and Spanne, P., *Medial Axis Analysis of Void Structure in three-dimensional tomographic images of porous media*, Journal of Geophysical Research **101**(B4), 8297-8310 (1996).

Lindquist, W.B., *Quantitative analysis of three-dimensional X-ray tomographic images*, Proc. SPIE **4503**, 103-115, Developments in X-Ray Tomography III (2002).

Lindquist, W.B., Venkatarangan, A., Dunsmuir, J., and Wong, T.F., *Pore and throat size distributions measured from synchrotron x-ray tomographic images of Fontainbleau sandstones*, Journal of Geophysical Research **105**: 21508 (2000).

Lohou, C. and Bertrand, G., *A 3D 12-subiteration thinning algorithm based on P-simple points*, Discrete Appl. Math. **139**(1–3), 171–195 (2004).

Lopes, R.T., Rodrigues J.L., De Assis, J.T., De Jesus E.F.O. and De Oliveira, L.F., *Evaluation of a Microtomography System with an X-ray Microfocus Tube*, Appl. Radiat. Isot. **48**(10-12), 1437-1442 (1997).

Lowry, M.I. and Miller, C.T., *Pore-scale modeling of nonwetting-phase residual in porous media*, Water Resources Research **31**(3), 455-473 (1995).

Lux, J., Delisèe, C. and Thibault, X., *3D characterization of wood based fibrous materials: an application*, Image Anal. Stereol. **25**, 25-35 (2006).

Maire, E., Fazekas, A., Salvo, L., Dendievel, R., Youssef, S., Cloetens, P. and Letang, J.M., *X-ray microtomography applied to the characterization of cellular materials. Related finite element modeling problems*, Composites Sc. and Tech. **63**, 2431–2443 (2003).

Mancini, L., Dreossi, D., Fava, C., Sodini, N., Tromba, G., Favretto, S. and Montanari, F., *TOMOLAB: the new X-ray micro-tomography facility at Elettra*, Elettra Highlights 2006-2007, December 2007.

Mancini, L., *Étude des Défauts dans les Quasicristaux en utilisant les Aspects Nouveaux de l'Imagerie aux Rayons X Associés aux Sources Synchrotron de Troisième Génération*, PhD Thesis, Université Joseph Fourier, Grenoble, June 1998.

Mardia, K.V. and Hainswotrh, T.J., *A Spatial Thresholding Method for Image Segmentation*, IEE Transactions on Pattern Analysis and Machine Intelligence **10**(6), 919-927 (1988).

Matthews, G.P., Moss, A.K., Ridgway, C.J., *The effects of correlated networks on mercury intrusion simulations and permeabilities of sandstone and other porous media*, J. Powder Technol. **83**(1), 61–77 (1995).

Mayo, S.C., Miller, P.R., Wilkins, S.W., Davis, T.J., Gao, D., Gureyev, T.E., Paganin, D., Parry, D.J., Pogany, A. and Stevenson, A., *Quantitative X-ray projection microscopy: phase-contrast and multi-spectral imaging*, J. of Microscopy **207**, 79-96 (2002).

Momose, A., Takeda, T. and Itai, Y., *Phase-contrast x-ray computed tomography for observing biological specimens and organic materials*, Rev. Sci. Instr. **66**, 1434-1436 (1995).

Montminy, M.D., Tannenbaum A.R., Macosko C.W., *The 3d structure of real polymer foams*, J. of Colloidal and Interface Science **208**, 202-211 (2004).

Montminy, M.D., Tannenbaum, A.R. and Macosko, C.W., *New Algorithms for 3-D Imaging and Analysis of Open-Celled Foams*, Journal of Cellular Plastics **37** (2001).

Moran, C.J., Pierret, A. and Stevenson, A.W., *X-ray absorption and phase-contrast imaging to study the interplay between plant roots and soil structure,* Plant and Soil **223**, 99-115 (2000).

Mousavi, R., Miri, T., Cox, P.W. and Fryer, P.J., *Imaging food freezing using X-ray microtomography*, Int. J. of Food Science & Technology **42**(6) , 714–727 (2007).

Oh, W. and Lindquist, W.B., *Image thresholding by indicator kriging*, IEEE Transactions on Pattern Analysis and Machine Intelligence **21**(7), 590-602 (1999).

Ohgaki, T., Toda, H., Uesugi, K., Kobayashi, T., Makii, K., Takagi, T. and Aruga, Y., *Application of Local Tomography Technique to High-Resolution Synchrotron X-ray Imaging*, Materials Science Forum Vols. 539-543, pp. 287-292 (2007).

Olurin, O.B, Arnold M., Korner, C. and Singer, R.F., *The investigation of morphometric parameters of aluminium foams using micro-computed tomography*, Materials Science and Engineering A **328**, 334-343 (2002).

Otsu, N., *A Threshold Selection Method from Gray-Level Histograms*, IEEE Transaction on Systems, Man and Cybernetics **9**(1), 62-66 (1979).

Pal, N.R. and Pal, S.K., *Entropic Thresholding*, Signal Processing **16**, 97-108 (1989).

Pani, S., *Tomographic imaging with synchrotron radiation*, Phys. Med. **XVI**(3), 155-159 (2000).

Perrot, C., Panneton, R., Olny, X. and Bouchard, R., *Mesostructural approach for characterising macroscopic parameters of open cell foams with computed microtomography*, Proceedings of the Institute of Acoustic **25**(5) (2003).

Peyré, G. and Cohen, L., *Heuristically driven front propagation for geodesic paths extraction*, Lecture Notes in Computer Science, Springer-Verlag GmbH **3752** (2005).

Pogany, A., Gao, D. and Wilkins, S.W., *Contrast and resolution in imaging with a microfocus x-ray source*, Rev. Sci. Instr. **68**, 2774-2782 (1997).

Polacci, M., Baker, D.B., Mancini, L., Favretto, S. and Hill, R.J., *Vesiculation in magmas from Stromboli and implications for normal Strombolian activity and paroxysmal explosions in basaltic systems*, J. Geophys. Res., submitted (2008).

Polacci, M., Baker, D.R., Mancini, L., Tromba, G. and Zanini, F., *Three-dimensional investigation of volcanic textures by X-ray microtomography and implications for conduit processes*, Geophys. Res. Lett. **33**, L13312, doi:10.1029/2006GL026241 (2006).

Polacci, M., Burton, M.R., La Spina, A., Murè, F., Favretto, S. and Zanini, F., *Correlating versciculation, degassing and style of eruptive activity at basaltic volcanoes: the case of the August-December 2006 Etna eruption (Italy)*, International Union of Geodesy and Geophysics (IUGG) – Perugia (Italy), July 2007.

Pratt, W.K., *Digital Image Processing – Second Edition*, Wiley-Interscience Publication, Jhon Wiley & Sons, Inc. (1991).

Ramaswamy, S., Gupta, M., Goel, A., Aaltosalmi, U., Kataja, M., Koponen, A. and Ramarao, B.V., *The 3D structure of fabric and its relationship to liquid and vapor transport*, Colloids and Surfaces A: Physicochem Eng. Aspects **241**, 323-333 (2004).

Remy, E. and Thiel, E., *Exact medial axis with Euclidean distance*, Image Vision Comput. **23**(2), 167–175 (2005).

Reynolds, A.P., Seidel, T.U. and Simonsen, M., *Visualization of material flow in an autogenous friction stir weld*, Proceeding of first international friction stir welding symposium, Thousand Oaks, USA, 14-16 June 1999.

Roberts, A.P. and Torquato, S., *Chord-distribution functions of three-dimensional random media: approximate first-passage times of Gaussian processes*, Physical Review E **59**, 4953-4963 (1999).

Russ, J.C., *The Image Processing Handbook*, 3rd Edition, IEEE PRESS (1999).

Rustichelli, F., Romanzetti, S., Dubini, B., Girardin, E., Raven, C., Snigirev, A. and Rizzi, G., *Phase-contrast microtomography of thin biomaterials*, J. of Materials Science: Materials in Medicine **15**(9), 1053-1057 (2004).

Saadatfar, M., Arns, C.H., Knackstedt, M.A. and Senden, T.J., *Mechanical and transport properties of polymeric foams derived from 3D images*, Colloids and Surfaces A, Physicochem. Eng. Aspects **263**, 284-289 (2004).

Saadatfar, M., Knackstedt, M.A., Arns, C.H., Sakellariou, A., Senden, T.J., Sheppard, A.P., Sok, R.M., Steininger, H. and Schrof, W., *Polymeric foam properties derived from 3D images*, Physica A **339**, 131-136 (2004).

Sahoo, P.K., Soltani, S., Wong, A.K.C., Chen, Y.C., *A survey of thresholding techniques*, Computer Vision, Graphics, and Image Processing **41**(2), 233-260 (1988).

Sakellariou, A., Sawkins T.J., Senden, T.J. and Limaye, A., *X-ray tomography for mesoscale physics applications*, Phys. A **339**, 152-158 (2004).

Salvo, L., Cloetens, P., Maire, E., Zabler, S., Blandin, J.J., Buffiere, J.Y., Ludwig, W., Boller, E., Bellet, D. and Josserond, C., *X-ray micro-tomography an attractive characterisation technique in materials science*, Nuclear Instruments and Methods in Physics Research B **200**(14), 273-286 (2003).

Sannitidi Baja, G. and Nyström, I., *Skeletonization in 3D discrete binary images*. In: Chen, C.H., Wang, P.S.P. (eds.) Handbook of Pattern Recognition and Computer Vision, 3rd ed., Chapter 22, pp. 137–156.World Scientific, Singapore (2005).

Schena, G. and Favretto, S., *Pore Space network characterisation with sub-voxel definition*, Transport in Porous Media **70**, 181-190 (2007).

Schena, G., Favretto, S., Santoro, L., Pasini, A., Bettuzzi, M., Casali, F., Mancini, L., *Detecting microdiamonds in kimberlite drill-hole cores by computed tomography*, Int. J. Miner. Process. **75** 173-188 (2005).

Schena, G., Santoro, L. and Favretto, S., *Conceiving a high resolution and fast X-ray CT system for imaging fine multi-phase mineral particles and retrieving mineral liberation spectra*, Int. J. Miner. Process. **84**, 327-336 (2007).

Serra, J., *Image Analysis and Mathematical Morphology*, Academic Press, London (1982).

Sethian, J.A., *Level set methods and fast marching methods: evolving interfaces in computational geometry,* Fluid Mechanics, Computer Vision and Materials Science Cambridge Monographs on Applied and Computational Mathematics, 2nd ed., pp. 378 (1999).

Siddiqi, K., Bouix, S., Tannenbaum, A. and Zucker, S.W., *Hamilton–Jacobi skeletons*, Int. J. Computer Vision **48**(3), 215–231 (2002).

Sijbers, J. and Postnov, A., *Reduction of ring artefacts in high resolution micro-CT reconstructions*, Physics in Medicine and Biology **49**(14) (2004).

Silin, D. and Patzek, T., *Pore space morphology analysis using maximal inscribed spheres*, Physica A **371**, 336-360 (2006).

Silin, D.B., Jin, G., Patzek, T.W., *Robust determination of the pore space morphology in sedimentary rocks,* Society of Petroleum Engineers, Inc. Paper SPE 84296 (2003).

Sodini, N., Dreossi, D., Favretto, S., Fioravanti, M., Mancini, L., Rigon, L., Tromba, G. and Zanini, F., *Characterization of archaeological wood by means of X-ray computed micro-tomography*, Science for Cultural Heritage, Lussingrande, Kroatia, August 2007.

Spanne, P., Thovert, J.F., Jacquin, C.J., Lindquist, W.B., Jones K.W. and Adler, P.M., *Synchrotron computed microtomography of porous media: topology and transports*, Phys. Rev. Lett. **73**, 2001-2004 (1994).

Steppe, K., Cnudde, V., Girard, C., Lemeur, R., Cnudde, J.P. and Jacobs, P., *Use of X-ray computed microtomography for non-invasive determination of wood anatomical characteristics*, Journal of Structural Biology **148**, 11-21 (2004).

Stevenson, A.W., Gao, D., Gureyev, T.E., Pogany, A. and Wilkins, S.W., *Hard X-ray Phase-Contrast Imaging With a Microfocus Source*, AIP Conf. Proc. **497**, 641-648 (1999).

Stevenson, A.W., Gureyev, T.E., Paganin, D., Wilkins, S.W., Weitkamp, T., Snigirev, A., Rau, C., Snigireva, I., Youn, H.S., Dolbnya, I.P., Yun, W., Lai, B., Garrett, R.F., Cookson, D.J., Hyodo, K. and Ando, M., *Phase-contrast X-ray imaging with synchrotron radiation for materials science applications*, Nucl. Instr. and Meth. in Phys. Res. B **199**, 427-435 (2003).

Succi, S., *The Lattice Boltzmann Equation for fluid dynamics and beyond*, 288 pp., Clarendon Press, Oxford (2001).

Suzuki, H. and Nakamura, I., *Acoustics of Pianos*, Applied Acoustics **30**, 147-205 (1990).

Tan, J.C., Elliott, J.A. and Clyne, T.W., *Analysis of Tomography Images of Bonded Fibre Networks to Mesure Distributions of Fibre Segment Length and Fibre Orientation*, Advanced Eng. Mat. **8**(6), 495-500 (2006).

Thomas, W.M., Nicholas, E.D., Needham, J.C., Church, M.G., Templesmith, P. and Dawes, J.C., International Patent Application No. PCT/GB92/02203 and GB Patent Application No. 9125978.9, 1991.

Torquato, S., *Random Heterogeneous Materials – microstructure and macroscopic properties*, Springer (2001).

Turner, M.L., Knüfing, L., Arns, C.H, Sakellariou, A., Senden, T.J., Sheppard, A.P., Sok, R.M., Limaye, A., Pinczewski, W.V. and Knackstedt, M.A., *Three-dimensional imaging of multiphase flow in porous media*, Physica A **339**, 166–172 (2004).

Umnova, O., Attenborough, K., Shin H.C. and Cummings, A., *Deduction of tortuosity and porosity from acoustic reflection and transmission measurements on thick samples of rigid porous materials*, Applied acoustics **66** (2005).

Van de Casteele E., Van Dyck, D., Sijbers J. and Raman, E., *An energy-based beam hardening model in tomography*, Phys. in Med. and Biol. **47**(23), 4181-4190 (2002).

Van de Casteele E., Van Dyck, D., Sijbers J. and Raman, E., *Effect of beam hardening on resolution in X-ray microtomography*, SPIE Medical Imaging (2004).

Van de Casteele, E., Van Dyck, D., Sijbers J. and Raman E., *A model-based correction method for beam hardening artefacts in X-ray microtomography*, J. of X-ray Sci. and Tech. **12**(1), 43-57 (2004).

Venkatarangan, A., *Geometric and statistical analysis of porous media*, PhD thesis, State University of New York at Stony Brook (2000).

von Smekal, L., Kachelriess, M., Stepina E. and Kalender, W.A., *Geometric misalignment and calibration in cone-beam tomography*, Med. Phys. **31**(12), 3242-3266 (2004).

Weiss, P., Obadia, L., Magne, D., Bourges, X., Rau, C., Weitkamp, T., Khairoun, I., Bouler, J.M., Chappard, D., Gauthier, O. and Daculsi, G., *Synchrotron X-ray microtomography (on a micron scale) provides three-dimensional imaging representation of bone ingrowth in calcium phosphate biomaterials*, Biomaterials **24**(25), 4591-4601 (2003).

Wevers, M., de Meester, P. and Swennen, R., *Microfocus X-ray computer tomography in materials research*, 15th WCNDT, Rome (2000).

Whitaker, S., *The method of volume averaging (Theory and applications of transport in porous media)*. Kluwer Academic Publishers, Dordrecht – The Netherlands (1999).

Wildenschild, D., Vaz C.M.P., Rivers M.L., Rikard D. and Christensen, B.S.B., *Using X-ray computed tomography in hydrology: systems, resolutions, and limitations*, Journal of Hydrology **267**, 285–297 (2002).

Wilkins, S.W., Gureyev, T.E., Gao, D., Pogany, A. and Stevenson, A.W., *Phase-contrast imaging using polychromatic hard X-rays*, Nature **384**(28), 335-338 (1996).

Wong, P., *Methods in the physics of porous media* **35** Academic press (1999).

Wu, Y.S., van Vliet, L.J., Frijlink, H.W. and van der Voort Maarschalk, K., *The determination of relative path length as a measure for tortuosity in compacts using image analysis*, European J. of Pharm. Science **28**, 443-440 (2006).

Xu, J., Stevenson, A.W., Gao, D., Tykocinski, M., Lawrence, D., Wilkins, S.W., Clark, G.M., Saunders, E. and Cowan, R. S., *The role of radiographic Phase-Contrast Imaging in the Development of Intracochlear Electrode Arrays*, Otology and Neurotology **22**(6), 862-868 (2001).

Yang, H. and Lindquist, W.B., *Three dimensional image analysis of fibrous materials*, Proc. SPIE **4115**, 275-282, Applications of Digital Image Processing XXIII, (2000).

Yang, H., *A geometric and Statistical Analysis of Fibrous Materials from Three-Dimensional High Resolution Images*, PhD Thesis in Dep. of App. Math. and Stat., State University of New York at Stony Brook: New York (2001).

Yeong, C.L.Y. and Torquato, S., *Reconstructing random media. II. Three-dimensional media from two-dimensional cuts*, Physical Review E **58**(1), 224-233 (1998).

Young, I.T., Gerbrands, J.J. and van Vliet, L.J., *Fundamental of Image Processing*, Delft PH Pubblications, 1999.

Youssef, S., Maire, E. and Gaertner, R., *Finite element modelling of the structure of cellular materials determined by X-ray tomography*, Acta Materialia **53**, 719-73 (2005).

Yu, Z.Y., Delerue, J.F.C. and Ma, S.D., *3D Euclidean distance transformation*, Proceedings of International symposium on image, speech, signal and robotics, Hong Kong (1998).

Zienkiewicz, O.C. and Taylor, R.L., *Finite Element Method* Butterworth Heinemann, London (2000).